

Dissertation zur Erlangung des Doktorgrades
der Fakultät für Chemie und Pharmazie
der Ludwig-Maximilians-Universität München

Magnetism and superconductivity
in layered manganese and iron pnictides

Franziska Hummel
aus
Madrid, Spanien

2015

Erklärung

Diese Dissertation wurde im Sinne von § 7 der Promotionsordnung vom 28. November 2011 von Herrn Prof. Dr. Dirk Johrendt betreut.

Eidesstattliche Versicherung

Diese Dissertation wurde eigenständig und ohne unerlaubte Hilfe erarbeitet.

München, 12.06.2015

Franziska Hummel

Dissertation eingereicht am	12.06.2015
1. Gutachter:	Prof. Dr. Dirk Johrendt
2. Gutachter:	Prof. Dr. Hubert Ebert
Mündliche Prüfung am	22.07.2015

Danksagung

Ganz herzlich möchte ich mich bei meinem Chef, Prof. Dr. Dirk Johrendt, für die Aufnahme in seinen Arbeitskreis, die Überlassung des interessanten Forschungsthemas, die forschersche Freiheit und die hervorragende Betreuung während dieser Doktorarbeit bedanken.

Prof. Dr. Hubert Ebert danke ich herzlich für die Übernahme des Zweitgutachtens.

Bei Prof. Dr. Konstantin Karaghiosoff, PD Dr. Rudi Hackl, Prof. Dr. Jörn Schmedt auf der Günne und Prof. Dr. Hans-Christian Böttcher bedanke ich mich dafür, dass sie sich als Prüfer für mein Rigorosum zur Verfügung gestellt haben.

Danke auch an all meine aktuellen und ehemaligen Kollegen: Daniel Bichler, Andreas Binek, Lars Bulthaupt, Katharina Förg, Rainer Frankovsky, Gina Friederichs, Lola Liliensten, Katarina Marković, Marianne Martin, Fabian Nitsche, Ursula Pachmayr, Simon Peschke, Roman Pobel, Constantin Frhr. Schirndinger von Schirnding, Anne Schulz, Juliane Stahl, Christine Stürzer, Tobias Stürzer, Marcus Tegel, Erwin Wiesenmayer, Veronika Zinth und natürlich unsere AK-Muddi Catrin Löhnert. Ebenso natürlich allen Ehrenmitgliedern des AK Johrendt. Euch allen danke ich für die Hilfsbereitschaft, Gerätebetreuung, für Service-Messungen und für die gute Stimmung.

Bei Marcus möchte ich mich ganz besonders bedanken: für Deine ansteckende Begeisterung und weil Du es schaffst, selbst die kompliziertesten Zusammenhänge mit bewundernswerter Geduld ganz einfach zu erklären.

Vielen Dank auch an Gina für die Gesellschaft in Labor, Büro und Japan inklusive Ausarbeitung des Plan-Alphabets und an Rainer, der keine Fremdsprache gescheut hat um die Stimmung im AK aufzulockern.

Außerdem möchte ich mich bei meinen Praktikanten bedanken, die mit ihrem Engagement zu den Ergebnissen dieser Doktorarbeit beigetragen haben: Kathrin Hedegger, Mareike Czuppa, Stefan Schwarzmüller, Sascha Harm und Kerstin Hoffmann.

Danke auch an alle „Partner-Arbeitskreise“ Schnick, Lotsch, Oeckler und Schmedt auf der Günne für die gute Zusammenarbeit.

Bei Thomas Miller und Wolfgang Wünschheim bedanke ich mich für die stete Unterstützung bei allen kleinen und größeren Problemen. Ganz gleich ob ein Computer, ein Generator, eine Pumpe, ein Durchflusssensor oder eine Schraube den Geist aufgibt, einer von euch weiß wie sich das Problem beheben lässt.

Vielen Dank auch an Christian Minke für die Durchführung von EDX-Messungen inklusive konstanter Wort-Witz-Versorgung.

Danke an Sergiy Mankovsky für die Durchführung und Erläuterung der SPR-KKR Rechnungen, an Johannes Weber für die unkomplizierte Hilfe bei Linux-Problemen, an Vico (Peter) Ribeiro Celinski für seine geduldigen Bemühungen bei Vanadium-NMR-Messungen, an Yixi Su und Anatoliy Senyshyn für die Hilfe bei der Durchführung und Interpretation von Neutronen-Messungen, an Hubertus Luetkens für μ SR-Messungen, an Ann-Kathrin Henss für XPS-Messungen, an Oliver Niehaus und Birgit Gerke für HT-SQUID- und Mössbauer-Experimente und an Sascha Harm für Topas 5.

Vielen Dank auch an meine Freunde, die (teilweise schon seit Jahrzehnten) für den nötigen freizeitlichen Ausgleich sorgen. Vor allem danke ich Susanne Porkestanotsche Jolanka Malkusch, *formerly known as* Das-Mädchen-mit-dem-Karohemd, für all die gemeinsam erlebten Peinlichkeiten und ihre bezaubernde Gesellschaft auf dem allerschönsten Foto der Welt.

Ganz besonders möchte ich mich bei meiner Familie bedanken, die mich in allem unterstützt und mir immer die Freiheit gelassen hat, meine eigenen Entscheidungen zu treffen.

Und natürlich bei Erwin.

*„Zur Wahrscheinlichkeit gehört auch,
dass das Unwahrscheinliche eintreten kann.“*

(Aristoteles)

Contents

1	Introduction	1
2	Methods	5
2.1	Synthetic methods.....	5
2.1.1	Starting materials	5
2.1.2	Equipment and conditions	6
2.1.3	Precursor synthesis.....	6
2.2	Powder diffraction.....	6
2.2.1	X-ray powder diffraction.....	6
2.2.2	Neutron powder diffraction	7
2.2.3	Rietveld refinements.....	7
2.3	Magnetic measurements	7
2.4	Resistivity measurements.....	8
2.5	Energy-dispersive X-ray analysis	8
2.6	Heat capacity	8
2.7	Mössbauer spectroscopy.....	9
2.8	Muon spin rotation.....	9
2.9	X-ray photoelectron spectroscopy	9
2.10	Density functional theory calculations.....	9
3	Dynamic magnetism in CsMn_2P_2	11
3.1	Introduction	11
3.2	Experimental details	12
3.3	Results and discussion.....	13
3.3.1	X-ray experiments	13
3.3.2	Measurements of physical properties	16
3.3.3	Neutron experiments	17
3.3.4	μSR experiments.....	20
3.4	Conclusion	22

4	The electronic structure of CsMn_2P_2	25
4.1	Introduction	25
4.2	Calculation details	25
4.3	Results and discussion.....	26
4.4	Conclusion	31
5	Modifying the magnetism in CsMn_2P_2	33
5.1	Introduction	33
5.2	Experimental details	34
5.3	Isoelectronic doping in $\text{Cs}_{1-x}\text{Rb}_x\text{Mn}_2\text{P}_2$	34
5.4	Electron doping in $\text{Cs}_{1-x}\text{Ba}_x\text{Mn}_2\text{P}_2$	38
5.5	O_2^- and H_2 -annealing	39
5.6	Conclusion	42
6	$\text{Eu}_3\text{Sc}_2\text{O}_5\text{Fe}_2\text{As}_2$	43
6.1	Introduction	43
6.2	Experimental details	44
6.3	Crystal structure	44
6.4	Magnetic properties.....	47
6.5	Substitution experiments on $\text{Eu}_3\text{Sc}_2\text{O}_5\text{Fe}_2\text{As}_2$	49
6.6	Conclusion	52
7	The effects of chemical pressure in the solid solution $\text{Sr}_2\text{ScO}_3\text{FeAs}_{1-x}\text{P}_x$	53
7.1	Introduction	53
7.2	Experimental details.....	54
7.3	Sample composition	55
7.4	Crystal structure	56
7.5	Magnetic properties.....	61
7.6	Conclusion	62
8	Weak magnetism and the Mott state of vanadium in superconducting $\text{Sr}_2\text{VO}_3\text{FeAs}$	64
8.1	Introduction	64

8.2	Experimental details	66
8.3	Crystal structure	67
8.4	Magnetic properties.....	69
8.5	DFT calculations.....	72
8.6	Conclusion	74
9	Superconductivity in $\text{Sr}_2\text{V}_{1-x}\text{Cr}_x\text{O}_3\text{FeAs}$	75
9.1	Introduction	75
9.2	Experimental details	76
9.3	Results and discussion.....	77
9.4	Conclusion	85
10	The influence of oxygen deficiency in the solid solution $\text{Sr}_2\text{V}_{1-x}\text{Cr}_x\text{O}_{3-y}\text{FeAs}$	86
10.1	Introduction	86
10.2	Experimental details	87
10.3	Sample composition	88
10.4	Crystal structure	90
10.5	Magnetic properties.....	92
10.6	Conclusion	95
11	Summary.....	96
	Bibliography	101
	Scientific contributions	108
	Curriculum vitae.....	111

1 Introduction

Even today, more than 100 years after its first discovery^[1], superconductivity is still a fascinating and not yet fully understood phenomenon. In search of new superconductors, empirical rules have always served as guidelines for researchers. For instance, magnetism was considered to be detrimental to superconductivity for a long time. This belief originated in a famous set of empirical guidelines in this field, based on experimental work of *Bernd Matthias*^[2,3], which can be summarized as follows: 1. "A high symmetry is good; cubic symmetry is the best." 2. "A high density of electronic states is good." 3. "Stay away from oxygen." 4. "Stay away from magnetism." 5. "Stay away from insulators." 6. "Stay away from theorists."^[4]

Of course, such rules are only valid until they are proved wrong by the discovery of exceptions. By now, all of the above-mentioned rules have been disconfirmed by newly discovered superconducting systems and magnetism has even been found essential for high-temperature superconductors.

A large contribution to this paradigm change has been made in 2008 by the report of superconductivity in $\text{LaO}_{1-x}\text{F}_x\text{FeAs}$ with a maximum critical temperature ($T_{c,\text{max}}$) of 26 K^[5]. Only a few months later high-temperature superconductivity was discovered in the isostructural samarium compound $\text{SmO}_{1-x}\text{F}_x\text{FeAs}$ with $T_{c,\text{max}} = 55 \text{ K}$ ^[6]. In this new class of iron-based high-temperature superconductors the emergence of superconductivity takes place in the proximity of magnetic ordering^[7,8]. Although the details of the mechanism are still under debate, it is believed that the formation of Cooper pairs is decisively facilitated by magnetic fluctuations^[9-13].

Typically, parent compounds like LaOFeAs exhibit a stripe-type antiferromagnetic (AFM) order of the iron moments^[14], which can be destabilized by doping or applying pressure whereby superconductivity is induced^[5,15,16]. By now it has even been proved that high-temperature superconductivity in iron-based compounds is not only found in the proximity of magnetism but does also coexist on a microscopic level with magnetic ordering^[17].

Since 2008, several new structure types have been added to the class of iron-based superconductors. All of them have one common structural element: layers of edge-sharing $\text{FeX}_{4/4}$ ($X = \text{pnictogen or chalcogen atom}$) tetrahedra which are separated from each other by different interlayers. Initially, it was assumed that larger interlayer distances correlate with higher critical temperatures. However, this theory did not hold true.

For reasons of simplicity, the structures are abbreviated by their stoichiometry. Figure 1.1 shows three of these structure types, which are subject to the present thesis. First, the so-

called 122 type (Figure 1.1, left). It crystallizes in the BaZn_2P_2 structure^[18] and contains $\text{FePn}_{4/4}$ (Pn = pnictogen atom) layers separated by single ions (alkaline, alkaline earth, or rare earth elements). The first iron-based superconductor in this structure type was $\text{Ba}_{1-x}\text{K}_x\text{Fe}_2\text{As}_2$, discovered in the year 2008 with a maximum critical temperature of 38 K^[19]. Here, the Fe-Fe interlayer distance is 665 pm.

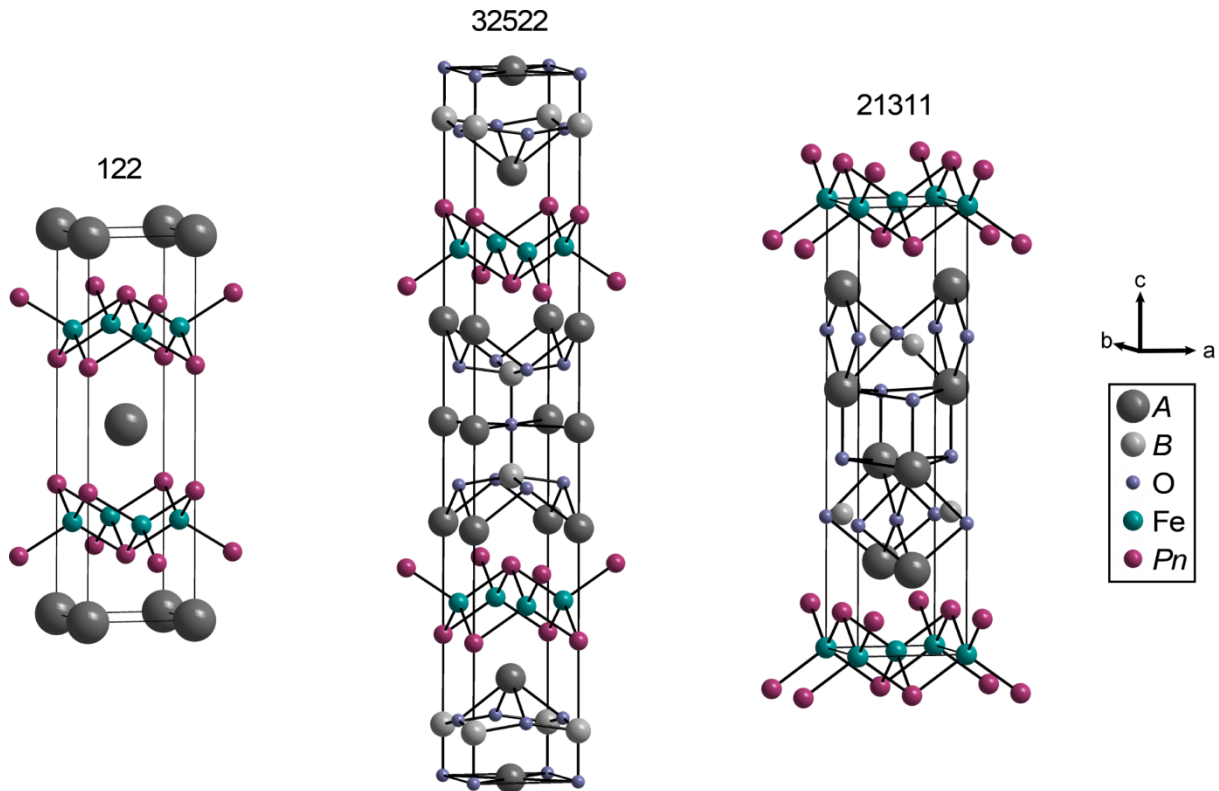


Figure 1.1: Crystal structures of the 122- (left), 32522- (middle), and 21311- (right) type iron-based superconductors.

The second structure type presented here is the so-called 32522 type (Figure 1.1, middle), which crystallizes in the $\text{Sr}_3\text{Fe}_2\text{O}_5\text{Cu}_2\text{S}_2$ structure^[20]. Hereby, the tetrahedral layers are separated by a perovskite-like oxide layer $(\text{A}_3\text{B}_2\text{O}_5)^{2+}$ with a divalent metal A^{2+} and a trivalent metal B^{3+} . Thus, the distance between two $\text{FePn}_{4/4}$ layers is considerably bigger than in the 122 type. The first compound with iron-pnictide layers in this structure type, $\text{Sr}_3\text{Sc}_2\text{O}_5\text{Fe}_2\text{As}_2$, was discovered in 2009 but does not exhibit superconductivity^[21]. It took two more years until the first superconducting member of the 32522 family was reported: $\text{Ca}_3\text{Al}_2\text{O}_5\text{Fe}_2\text{As}_2$ with $T_c = 30$ K and an Fe-Fe interlayer distance of 1304 pm^[22].

The third structure type which will be studied in this thesis is the so-called 21311 type (Figure 1.1, right). It crystallizes in the $\text{Sr}_2\text{GaO}_3\text{CuS}$ structure^[23] and exhibits a Ruddlesden-Popper-analog^[24] perovskite-like interlayer $(\text{A}_4\text{B}_2\text{O}_6)^{2+}$ with even larger interlayer distances than the

32522 type. In this structure type the first known superconductor, $\text{Sr}_2\text{ScO}_3\text{FeP}$, was reported in 2009 with a T_c of 17 K and an Fe-Fe interlayer distance of 1554 pm^[25].

Based on the insights into high-temperature superconductivity obtained by this new class of iron-based compounds, the initially quoted guidelines have become obsolete and a very reasonable, revised set of guidelines was proposed by *Mazin*: 1. "Layered structures are good". 2. "The carrier density should not be too high". 3. "Transition metals of the fourth period (vanadium, chromium, manganese, iron, cobalt, nickel and copper) are good". 4. "Magnetism is essential". 5. "Proper Fermi surface geometry is essential". 6. "Enlist theorists".^[4] Additionally, it was recommended that the physicists, which still dominate this research field, work together with solid-state chemists because the compounds of interest can be quite complex.

Not only the chemical structure, but also the physical properties of the corresponding compounds have in some cases turned out to be rather intricate. However, in order to understand the essential features of high-temperature superconductivity, it is necessary to study the underlying fundamental properties. As magnetism has been proved to be a prerequisite, it is one of the decisive factors worth analyzing in more detail. Systems exhibiting magnetic fluctuations might reveal new insights into the complex physics of superconductivity or even lead the way to new classes of high-temperature superconductors. Such fluctuations are mainly found in compounds with small magnetic moments ($\sim 1 \mu_B$) and low ordering temperatures. However, they can also occur in metals with larger moments due to itinerant magnetism. Additionally, layered structures with a high degree of two-dimensionality and therefore a high density of states (DOS) at the Fermi level (E_F) favor the emergence of magnetic fluctuations.

The present thesis concentrates on compounds of the 122, 32522, and 21311 types, described above, which exhibit itinerant magnetism, superconductivity, or which are promising candidates for high-temperature superconductivity. Hereby, not only iron-based systems are studied. Within the scope of this work, magnetic and superconducting properties are investigated along with their influencing factors in known and newly synthesized systems.

In Chapter 3 the manganese-based 122 compound CsMn_2P_2 is characterized in detail. Unlike what has been reported in literature so far, CsMn_2P_2 exhibits a complicated magnetism with dynamic effects. An extensive study based on a wide range of experimental methods is performed in order to clarify the unusual behavior.

Accompanying theoretical calculations are presented in Chapter 4. Here, the electronic structure of the experimentally determined magnetic structure of CsMn_2P_2 is evaluated and possible indications for the origin of the observed dynamic effects are investigated.

Concluding the studies of the 122 type in this thesis, Chapter 5 describes different approaches to modifying the magnetic properties of CsMn_2P_2 . Isoelectronic doping by partial substitution of cesium by rubidium, electron doping by substitution of cesium by barium, and annealing experiments under oxygen and hydrogen atmosphere are presented. The corresponding effects upon the physical properties of the compounds, in particular the magnetism, are thoroughly analyzed.

Chapter 6 introduces $\text{Eu}_3\text{Sc}_2\text{O}_5\text{Fe}_2\text{As}_2$ as a new member of the iron-based 32522 family and the first europium compound of this structure type. Although the compound itself does not exhibit superconductivity, it is a possible parent compound for future superconductors.

The following Chapters 7 to 10 are dedicated to compounds of the 21311 structure. Hereby, Chapter 7 discusses the effects of chemical pressure upon the structural and magnetic properties of $\text{Sr}_2\text{ScO}_3\text{FeAs}$ by partial substitution of arsenic by phosphorus. This new solid solution $\text{Sr}_2\text{ScO}_3\text{FeAs}_{1-x}\text{P}_x$ exhibits superconductivity for $x \geq 0.6$.

Subsequently, the stoichiometry and magnetic state of superconducting $\text{Sr}_2\text{VO}_3\text{FeAs}$, which have been a subject of numerous discussions, are studied in Chapter 8. The following presentation of the new solid solution $\text{Sr}_2\text{V}_{1-x}\text{Cr}_x\text{O}_3\text{FeAs}$ (Chapter 9) allows a detailed study of numerous influencing factors in order to examine which of them are decisive for the superconducting properties of the system.

Finally, Chapter 10 investigates the alleged significance of oxygen vacancies within this system. The effects of nominal oxygen deficiency in $\text{Sr}_2\text{V}_{1-x}\text{Cr}_x\text{O}_{3-y}\text{FeAs}$ upon the structural and superconducting properties of the compounds are discussed in detail.

Altogether, the present thesis contributes to the fundamental research necessary for the deeper understanding of magnetic and superconducting properties, which is an essential prerequisite for the discovery of new superconducting systems.

2 Methods

2.1 Synthetic methods

This chapter describes the materials and equipment used for this thesis and the general synthetic conditions. Additionally, the syntheses of precursors are described. Detailed information on the individual synthesis processes of the compounds are given in the experimental section of the corresponding chapters.

2.1.1 Starting materials

Table 2.1 lists the starting materials used in this work, including their molar weight, purity, appearance, and source of supply.

Table 2.1: Starting materials used in this work.

material	molar weight (g/mol)	purity (%)	appearance	supplier
Al	26.9815	99.95	powder	Sigma-Aldrich
As	74.9216	99.999	pieces	Alfa Aesar
As ₂ O ₃	197.8414	99.5	powder	Acros
Ba	137.327	99.99	pieces	Sigma-Aldrich
Ca	40.078	99.99	pieces	Sigma-Aldrich
Cr	51.9961	99.8	powder	Alfa Aesar
Cs	132.9055	99.98	ingot	Smart Elements
Eu	151.964	99.90	pieces	Alfa Aesar
Fe	55.845	99.90	powder	Chempur
Fe ₂ O ₃	159.6882	99.999	powder	ABCR
FeO	71.8444	99.90	powder	Sigma-Aldrich
Mg	24.305	99.8	pieces	Alfa Aesar
Mn	54.938	99.9985	pieces	Alfa Aesar
P (red)	30.9738	99.999	pieces	Chempur
P ₂ O ₅	141.9445	99	powder	Sigma-Aldrich
Rb	85.4678	99.75	ingot	Alfa Aesar
Sc	44.9559	99.99	pieces	Smart Elements
Sc ₂ O ₃	137.91	99.9	powder	Alfa Aesar
Sr	87.62	99.95	pieces	Sigma-Aldrich
Ti	47.867	99.5	powder	Alfa Aesar
V	50.9415	99.70	powder	ABCR

2.1.2 Equipment and conditions

All materials were handled in a glove box (MBRAUN, MB150-GL with H_2O and $\text{O}_2 < 1$ ppm and UNIlab Plus with H_2O and $\text{O}_2 < 0.1$ ppm) under an atmosphere of purified argon (99.999 %, Air Liquide).

As reaction containers either alumina crucibles (Friatec) or niobium ampoules (Holdenrieder) were used, whereby the latter were sealed by arc-melting. The containers were then transferred into pre-dried silica ampoules (Vogelsberger, HSQ 300) and sealed under argon atmosphere. The reactions were performed in tubular resistance furnaces with Pt/PtRh or NiCr/Ni thermocouples and PID temperature controllers (Eurotherm, model 2408).

2.1.3 Precursor synthesis

For the syntheses described in Chapters 3 and 5, Cs_4P_6 , Rb_4P_6 , and Ba_5P_4 were used as precursors.

Cs_4P_6 (1 g) was obtained by heating stoichiometric mixtures of Cs and P up to 920 K, enclosed in a niobium ampoule (5.9 cm in length), sealed in a silica ampoule, with a heating rate of 50 K/h, holding this temperature for 48 h and then turning off the furnace.

Rb_4P_6 (1 g) was synthesized analogously but with a heating rate of only 25 K/h and a reaction temperature of 870 K.

For the synthesis of Ba_5P_4 (0.5 g), stoichiometric mixtures of Ba and P were heated up to 1373 K in an alumina crucible, sealed in a silica ampoule, and held at this temperature for 10 h. Thereby, rates of 20 and 50 K/h were chosen for heating and cooling, respectively.

2.2 Powder diffraction

2.2.1 X-ray powder diffraction

X-ray powder-diffraction (XRD) patterns were recorded using the following diffractometers:

- Huber G670 Guinier Imaging Plate diffractometer with $\text{Cu-K}\alpha_1$ radiation ($\lambda = 0.15406$ nm), Ge (111) primary monochromator, silicon as external standard, and an oscillating sample holder, whereby the samples were held between two foils (BoPET).
- Huber G670 Guinier Imaging Plate diffractometer with $\text{Co-K}\alpha_1$ radiation ($\lambda = 0.17890$ nm), Ge (111) primary monochromator, silicon as external standard, an oscillating sample holder, and additionally equipped with the low-temperature device

670.4 with a closed-cycle He cryostat (CTI-Cryogenics, model 22 CP) and a temperature controller (Lakeshore, model 331) for temperature-dependent measurements in the range of 300 to 10 K. The samples were held between two foils (BoPET).

- STOE Stadi P diffractometer with Mo-K α_1 radiation ($\lambda = 0.07093$ nm), Ge (111) primary monochromator, silicon as external standard, using rotating capillaries with an outer diameter of 0.3 mm.

The Huber data were pre-processed with the program HConvert^[26], STOE data were handled with the STOE WinXPOW program package^[27]. For phase analyses the JCPDS^[28] database was used.

2.2.2 Neutron powder diffraction

High-resolution neutron powder-diffraction measurements were performed at SPODI, FRM II, Garching, in a temperature range of 3.5 to 300 K with an incident wavelength of 0.1548 nm in cooperation with *Dr. A. Senyshyn*. Measurements with polarized neutrons were recorded at the polarized-neutron spectrometer DNS, JCNS, Garching, between 2 and 298 K with an incident wavelength of 0.42 nm in cooperation with *Dr. Y. Su*. Polarization analysis of this data was performed via the xyz-method^[29].

The samples were filled into the sample containers (vanadium or aluminum) in a glove box under argon atmosphere and sealed with indium wire.

2.2.3 Rietveld refinements

For Rietveld refinements of the X-ray and neutron data, the TOPAS package^[30] was used with the fundamental parameter approach as reflection profiles. March Dollase or spherical harmonics functions describe the preferred orientation of the crystallites. If necessary, shape anisotropy effects were described by the approach of *Le Bail* and *Jouanneaux*^[31]. The diffractometer specific templates were created by *Dr. M. Tegel* and are explained in [32].

For magnetic refinements of the neutron data, version 5 of TOPAS^[33] was used.

2.3 Magnetic measurements

Magnetic measurements were carried out at a SQUID magnetometer (MPMS-XL5, Quantum Design, Inc.) in a temperature range of 1.8 to 300 K with applied fields of -50 to 50 kOe.

Additionally, a differential dual-coil AC susceptometer was used in a temperature range of 3.5 to 300 K with an applied field of 3 Oe. A detailed description of the experimental setup can be found in [32].

For the magnetic measurements, 5 to 50 mg of the samples were transferred into gelatine capsules, fixed in plastic straws. The data were processed with fully automated processor software^[34,35].

High-temperature susceptibility measurements in the temperature range of 300 to 800 K were performed using a Physical Property Measurement System (PPMS, Quantum Design, Inc.) with VSM-Oven option. The samples were fixed to a heater stick using an alumina-based cement.

2.4 Resistivity measurements

Resistivity measurements were performed using a standard four-probe method. The setup for the measurements is described in [32]. About 100 mg of the samples were pressed into a pellet with a diameter of 4 mm and sintered for 20 h at a temperature 200 or 300 K lower than the synthesis temperature. Afterwards, the pellets were mounted on the sample holder and contacted with conductive paint. The data were processed with a fully automated software^[36].

2.5 Energy-dispersive X-ray analysis

Energy dispersive X-ray (EDX) experiments were performed on a Jeol JSM-6500 FE SEM and a Carl Zeiss EVO-MA 10 with an SE, BSE, and a Bruker Nano EDX (X-Flash 410-M) detector. The samples were measured using adhesive conducting carbon films to fix them on brass sample holders. Therefore, the elements Cu, Zn, and C were not included in the analyses. Depending on the purpose of the measurements, between 5 and 50 (usually about 20) different positions on one sample were chosen to collect the spectra.

2.6 Heat capacity

The heat capacity measurements were carried out with a PPMS (Quantum Design, Inc.) in a temperature range of 2.2 to 80 K at the WWU Münster. The samples were fixed to the platform of a pre-calibrated heat capacity puck using grease (Apiezon N).

2.7 Mössbauer spectroscopy

Mössbauer spectroscopic characterizations were performed by *B. Gerke*, WWU Münster, using the 21.53 keV transition of ^{151}Eu with an activity of 130 MBq (2 % of the total activity of a $^{151}\text{Sm} : \text{EuF}_3$ source) and a $^{57}\text{Co}/\text{Rh}$ source. The measurements were conducted in transmission geometry with a commercial nitrogen-bath (78 K) and helium-flow (4.8 K) cryostat, while the sources were kept at room temperature. Samples of 100 mg (for ^{151}Eu measurements) and 40 mg (for ^{57}Fe measurements) were placed in thin-walled PVC containers at optimized thicknesses of about 16.4 mg Eu / cm² and 1.6 mg Fe / cm². Fitting of the spectra was performed with the Normos-90 program system.^[37]

2.8 Muon spin rotation

Muon spin rotation (μSR) experiments were conducted at the GPS spectrometer at the Swiss Muon Source (PSI, Switzerland) in cooperation with *Dr. H. Luetkens*. Zero field (ZF) data (without externally applied magnetic field) were recorded at temperatures between 1.6 and 310 K. Additionally, a field scan with longitudinally applied magnetic fields (LF) of 30 to 400 G was performed. The data were analyzed using the musrfit package^[38]. The ZF data were fitted with a Bessel and a cosine function (both damped) and a longitudinal tail, while the LF data were fitted with a static Lorentz Kubo-Toyabe function. For a detailed explanation of the fitting functions see [39]. A short introduction into the fundamentals of μSR is given in [40].

2.9 X-ray photoelectron spectroscopy

X-ray photoelectron spectroscopy (XPS) measurements were performed by *A.-K. Henß*, LMU Munich, with a VSW TA10 X-ray source, providing non-monochromated Mg-K α radiation, and a VSW HA100 hemispherical analyzer. The samples were cleaned before the measurement by 30 minutes of Ar⁺ sputtering (1 kV and $\sim 7 \mu\text{A}$). The recorded elemental peaks were fitted with a Doniach-Sunjic line shape convoluted with a Gaussian and linear background subtraction^[41].

2.10 Density functional theory calculations

Electronic band structure calculations were performed with the WIEN2k program package^[42] using density functional theory (DFT) within the full-potential augmented plane-wave plus local-orbital (APW+lo) method and the generalized gradient approximation (GGA). For detailed descriptions see Refs. [43] and [44]. A separation energy for core and valence

states of -6 Ry or -7 Ry was used. The energy and charge convergence criteria were chosen to be 10^{-5} Ry/cell and 10^{-4} e/cell, respectively, and between 56 and 828 irreducible k points were used with a cutoff for plane waves $R_{\text{MT}}k_{\text{max}} = 7.0$. The muffin-tin sphere radii R_{MT} and the exact calculation details are given in the corresponding chapters.

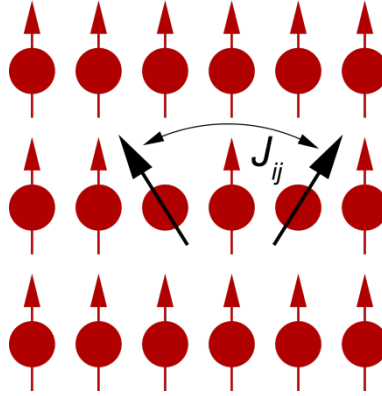


Figure 2.1: Schematic illustration of the interatomic exchange coupling parameter J_{ij} .

Interatomic exchange coupling parameters J_{ij} were calculated by *Dr. S. Mankovskyy*, LMU Munich, within the local spin density approximation (LSDA) for DFT using the Korringa-Kohn-Rostoker (KKR) Green function formalism. The self-consistent electronic structure calculations were performed by means of the spin-polarized relativistic KKR (SPR-KKR) method^[45,46] employing the atomic sphere approximation (ASA). Exchange and correlation effects were treated within the framework of local spin DFT, using the parametrization of *Vosko et al.*^[47]. In order to calculate the exchange coupling parameters, the DFT energy change associated with small deviations of two magnetic moments from their equilibrium directions (Figure 2.1) can be mapped onto the Heisenberg model represented by the Hamiltonian:

$$H_{\text{ex}} = - \sum_{\substack{ij \\ (i \neq j)}} J_{ij} \hat{e}_i \cdot \hat{e}_j,$$

with the lattice sites i and j and the unit vectors \hat{e}_i and \hat{e}_j along the directions of the corresponding magnetic moments.^[48] A rigorous expression for the evaluation of this energy, *i.e.* for J_{ij} calculations was derived by *Lichtenstein*^[49,50] within the magnetic force theorem.

3 Dynamic magnetism in CsMn₂P₂

3.1 Introduction

The proximity of magnetism and superconductivity is a typical feature of high- T_c iron-pnictide superconductors. By doping the parent compounds, antiferromagnetism can be suppressed and superconductivity induced. In order to study the effect of hole doping upon antiferromagnetism, CsMn₂P₂ can serve as a model system. Analogously to 122-type iron-pnictide superconductors, CsMn₂P₂^[51] crystallizes in the BaZn₂P₂ type^[18]. It is a mixed-valent Mn²⁺/Mn³⁺ compound and can be considered as strongly hole-doped BaMn₂P₂, which only contains Mn²⁺. While BaMn₂P₂ is a semiconductor with a small band gap (0.073 eV) and orders antiferromagnetically with G-type ordering at a Néel temperature above 750 K^[52], CsMn₂P₂ was reported to show an antiferromagnetic order at a considerably lower temperature (110 K, see Figure 3.1). The experimentally determined magnetic moment per formula unit is 4.81 μ_B , leading to an average of 3.4 μ_B per manganese atom. Susceptibility measurements also showed a discontinuity below 20 K, the origin of which could not be clarified.

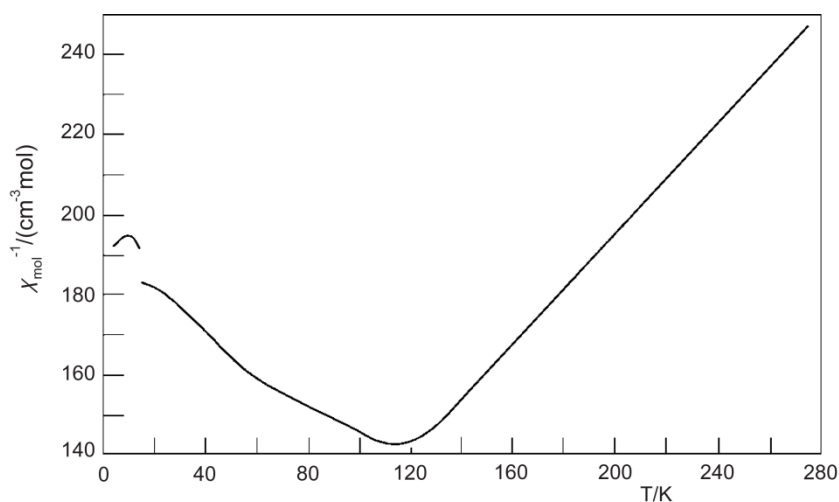


Figure 3.1: Inverse susceptibility of CsMn₂P₂ as published in [51].

However, investigations within my master thesis surprisingly did not show any sign of a magnetic ordering around 110 K but found an antiferromagnetic ordering at 11 K and Curie-Weiss behavior above this temperature^[53]. The magnetic transition at 110 K found in [51] can probably be ascribed to a significant but undetected amount of Mn₂P, an antiferromagnet with a Néel temperature of 110 K^[54]. Mn₂P is often obtained as impurity phase during the

synthesis of CsMn₂P₂ but has probably not been detected in [51] because the structure of CsMn₂P₂ was studied by single-crystal analysis, while susceptibility measurements were performed on a powder sample without further analysis of the composition.

Thus, the difference in the Néel temperatures of BaMn₂P₂ with $T_N > 750$ K and CsMn₂P₂ with $T_N = 11$ K is even bigger than assumed before. This means that a strong hole doping of BaMn₂P₂, which conceptually leads to the electronic state in CsMn₂P₂, considerably weakens the antiferromagnetism of the system. In contrast to this, in iron-based superconductors already small amounts of hole doping often lead to a complete suppression of the magnetism. This difference is ascribed to the significantly larger magnetic moment of Mn in CsMn₂P₂ ($\sim 3.4 \mu_B$) compared to the magnetic moment of Fe in typical iron-pnictide superconductors ($\sim 1 \mu_B$)^[53].

Additionally, resistivity measurements of CsMn₂P₂ revealed metallic behavior, an anomaly around 50 K, and an abrupt increase at 17 K.^[53] It was assumed that the anomaly might originate from an undetected impurity phase. The abrupt upturn at 17 K was ascribed to a possible structural phase transition of CsMn₂P₂ with a metal-to-insulator transition. However, low temperature X-ray diffraction experiments in the temperature range from 300 to 10 K with a minimum step size of 10 K were not detailed enough to prove such a structural transition between 20 and 10 K.

In this chapter, a more detailed study of the structure at low temperatures is presented along with neutron diffraction and muon spin rotation (μ SR) experiments, which give further insights into the magnetic behavior of CsMn₂P₂ and shed some light onto the anomalies observed in the resistivity measurement.

3.2 Experimental details

A polycrystalline sample (2 g) of CsMn₂P₂ was synthesized by heating a mixture of Cs₄P₆, Mn, and P with a ratio of 21:160:34 (5 % excess of Cs), sealed in a niobium crucible in a sealed silica ampoule. The sample was heated up to 1073 K for 14 h at rates of 50 K/h for heating and cooling.

Room-temperature X-ray powder-diffraction patterns were recorded using the STOE diffractometer with Mo-K α_1 radiation. Temperature-dependent X-ray data between 300 K and 10 K were recorded using the Huber diffractometer (Co-K α_1 radiation). For Rietveld refinements of the data the TOPAS package^[30] was used with spherical harmonics functions to describe the preferred orientation of the crystallites. Neutron powder-diffraction measurements of CsMn₂P₂ between 3.5 K and 300 K were performed at SPODI and, using polarized neutrons, at DNS. Magnetic measurements were carried out at the SQUID

magnetometer. Additionally, high-temperature susceptibility, resistivity, heat capacity, and μSR measurements were performed.

3.3 Results and discussion

3.3.1 X-ray experiments

By upscaling and further optimizing the synthesis of CsMn_2P_2 described in [53], a 2-g sample with only 1 % of Mn_2P and 2 % of CsMnP (wt%) as impurity phases was obtained. A Rietveld refinement of the X-ray data at 298 K is shown in Figure 3.2 (top). The corresponding crystallographic data can be found in Table 3.1. Polycrystalline CsMn_2P_2 was obtained as black, air-sensitive sample.

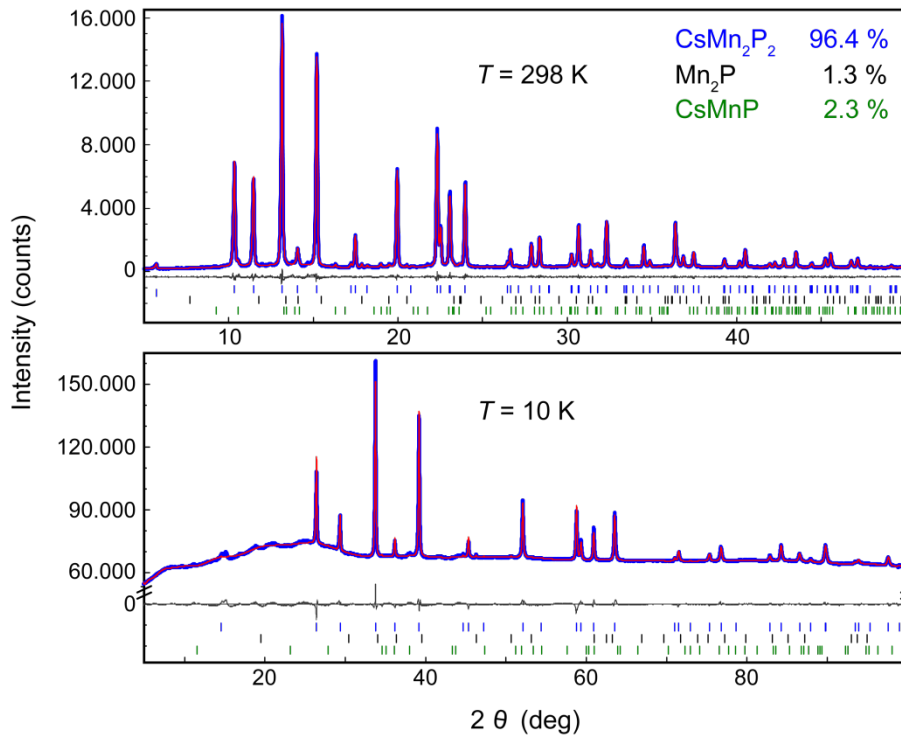


Figure 3.2: X-ray powder-diffraction pattern (blue) at 298 K (top, Mo- $\text{K}\alpha_1$ radiation) and 10 K (bottom, Co- $\text{K}\alpha_1$ radiation) with Rietveld refinements (red) of CsMn_2P_2 .

Table 3.1: Crystallographic data for CsMn₂P₂ at 10 K and 298 K obtained by X-ray measurements.

	CsMn ₂ P ₂	
temperature (K)	10	298
diffractometer	Huber	STOE
wavelength (nm)	0.17890	0.07093
space group	<i>I4/mmm</i> (no. 139)	<i>I4/mmm</i> (no. 139)
molar mass (g/mol)	304.7291	304.7291
lattice parameter <i>a</i> (pm)	407.41(1)	409.48(1)
lattice parameter <i>c</i> (pm)	1411.97(2)	1420.41(2)
cell volume (nm ³)	0.23436(1)	0.23816(1)
density (g/cm ³)	4.32(1)	4.24(1)
<i>Z</i>	2	2
data points	19001	4500
reflections (all phases)	108	263
refined parameters	64	73
<i>R_P</i> , <i>wR_P</i>	0.004, 0.007	0.038, 0.054
<i>R_{bragg}</i> , χ^2	0.011, 1.846	0.036, 1.333
atomic parameters		
Cs 2 <i>a</i> (0, 0, 0)	<i>U_{iso}</i> = 112(6) pm ²	<i>U_{iso}</i> = 171(3) pm ²
Mn 4 <i>d</i> (0, 0.5, 0.25)	<i>U_{iso}</i> = 114(7) pm ²	<i>U_{iso}</i> = 101(4) pm ²
P 4 <i>e</i> (0,0, <i>z</i>)	<i>z</i> = 0.3429(2) <i>U_{iso}</i> = 38(8) pm ²	<i>z</i> = 0.3368(2) <i>U_{iso}</i> = 109(5) pm ²
tetrahedral angle α (°)	107.0(1)	105.4(1)
Mn-P distance (pm)	242.3(2)	239.0(1)

In order to analyze the structure at low temperatures and check for a possible structural transition between 20 and 10 K suggested in [53], low-temperature XRD measurements were performed. The obtained pattern at 10 K is shown in Figure 3.2 (bottom) and the corresponding crystallographic data are listed in Table 3.1.

The refined lattice parameters and cell volume upon cooling (Figure 3.3) exhibit clear signs of structural changes at low temperatures. While initially, as expected, both lattice parameters decrease with decreasing temperature, a distinct increase is observed below 17 K with a second step below 11 K. In the first temperature range between 300 and 17 K the lattice parameter *a* decreases by 0.5 %, *c* by 0.7 % and thus the cell volume *V* decreases by 1.7 %. Upon further cooling down to 10 K, *V* increases by 0.1 %, whereby the increase of *c* is more than twice as big as the increase of *a* (0.07 % and 0.03 %, respectively). Thus, the structural changes at 17 and 11 K lead to an enlargement of the unit cell, which is mainly extended along *c*. Interestingly, the temperatures at which an increase in lattice parameters

is found, coincide with the temperature at which the abrupt upturn in resistivity was observed (17 K) as well as with the Néel temperature $T_N = 11$ K of CsMn₂P₂.

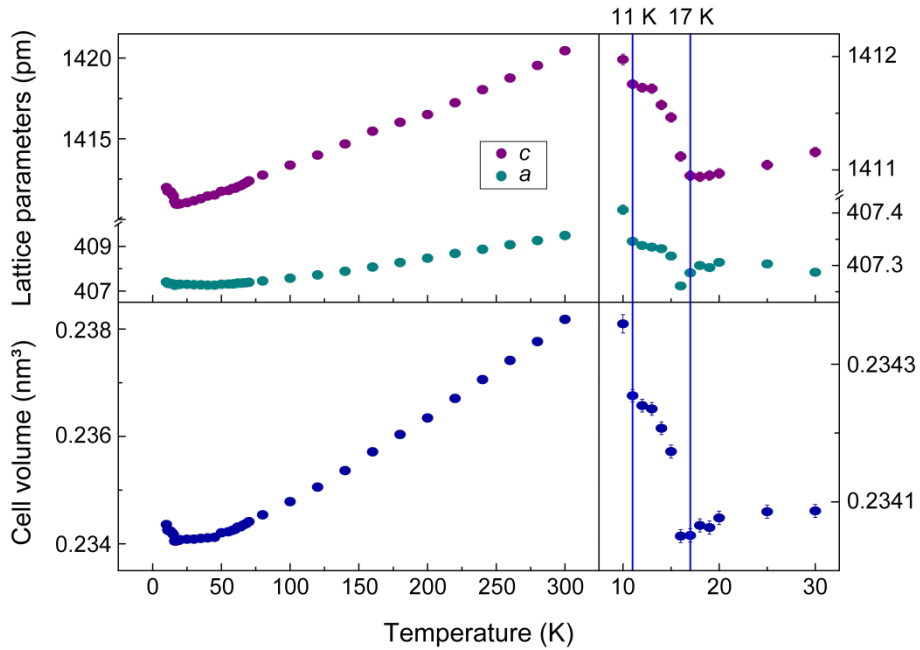


Figure 3.3: Refined lattice parameters (top) and cell volume (bottom) of CsMn₂P₂ as a function of temperature with enlarged low-temperature sections (right).

The Mn-P distance within the MnP_{4/4} tetrahedra, the tetrahedral angle α , and the z coordinate of phosphorus (Figure 3.4) do not show any significant changes in the temperature range between 300 and 10 K. Thus, the structural transitions below 17 K do not affect the geometry of the tetrahedral MnP layers but lead to an increased interlayer distance.

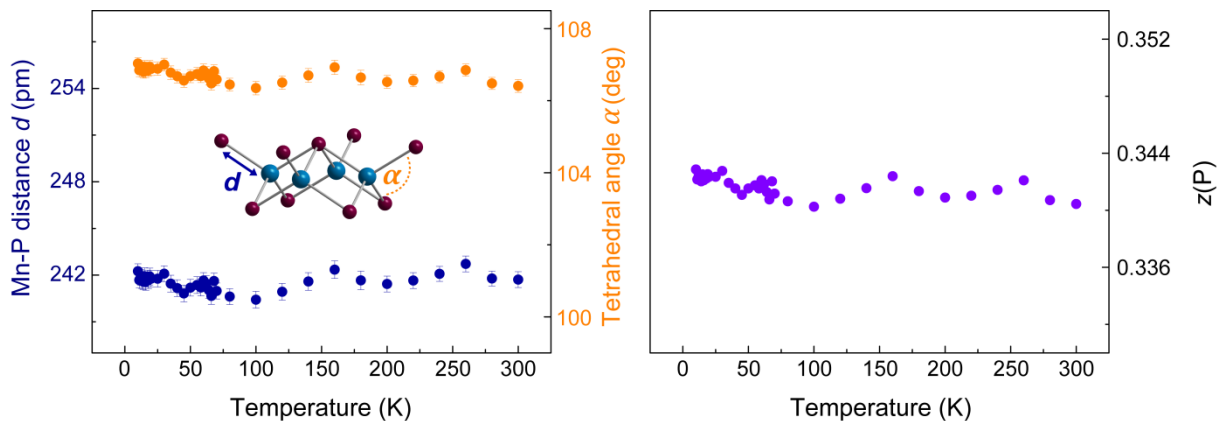


Figure 3.4: Refined Mn-P distance d (blue, left), tetrahedral angle α (orange, left), and z coordinate of phosphorus (right) in CsMn₂P₂ as a function of temperature.

3.3.2 Measurements of physical properties

In order to examine the magnetic purity of the sample, magnetic measurements were performed (Figure 3.5). Similar to the data described in [53], they indicate a Néel temperature of 11 K and Curie-Weiss behavior above this temperature. A Curie-Weiss fit revealed an effective moment of $4.68 \mu_B$ per formula unit, equivalent to $3.31 \mu_B$ per Mn atom. This is very close to the theoretically expected value of $3.35 \mu_B$ for an average of 2.5 unpaired electrons. High-temperature susceptibility measurements revealed an almost linear course of the inverse susceptibility and no signs of additional magnetic transitions up to 800 K. Magnetization isotherms at 1.8 and 300 K increase linearly with the applied field and do not exhibit any hysteresis or other anomalies. Thus, no magnetic impurity was detected.

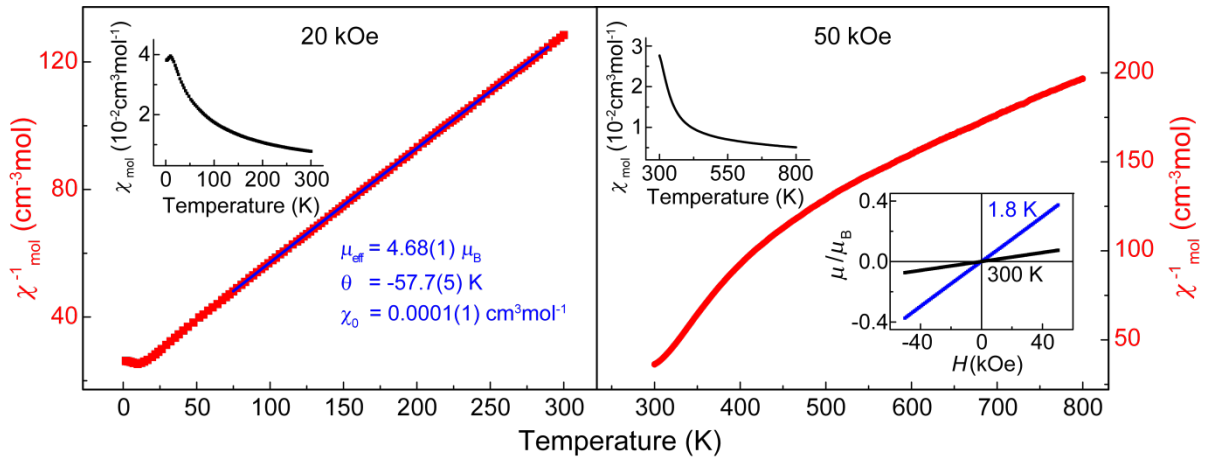


Figure 3.5: SQUID data of CsMn₂P₂. Left: 1.8 to 300 K. Inverse susceptibility at 20 kOe (red) and Curie-Weiss fit (blue). Inset: Susceptibility at 20 kOe. Right: 300 to 800 K. Inverse susceptibility at 50 kOe. Insets: Susceptibility at 50 kOe (top left) and magnetization isotherms at 1.8 K and 300 K (bottom right).

The sample of CsMn₂P₂ was further characterized by heat capacity measurements (Figure 3.6, right). Three peaks are observed indicating transitions at 64, 17, and 11 K.

The temperatures of these transitions are consistent with the temperatures at which anomalies occur in magnetic susceptibility and resistivity data, and in the course of the lattice parameters. The first transition at 64 K coincides with the onset of the broad anomaly found in the resistivity measurement (Figure 3.6, left), while the second one at 17 K matches the abrupt increase in resistivity and the first increase of the lattice parameters. Finally, the third transition at 11 K corresponds to the Néel temperature of CsMn₂P₂ detected by the susceptibility measurement and the temperature of the second lattice parameter step.

As the area below all three heat capacity peaks is very similar in size, each of the three transitions involves a similar change in the total enthalpy of the system. Therefore, it can be concluded that all anomalies detected at these three transition temperatures originate from the main phase. This includes the broad anomaly in resistivity emerging at 64 K, which was originally ascribed to an undetected impurity phase.

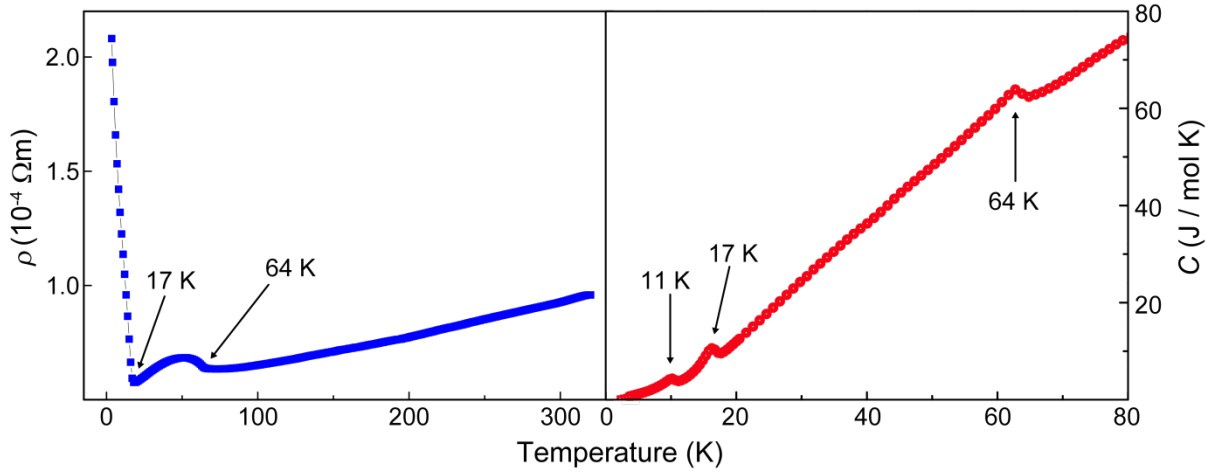


Figure 3.6: Resistivity (left) and heat capacity (right) measurement of CsMn₂P₂.

3.3.3 Neutron experiments

Figure 3.7 (bottom) shows the neutron powder pattern recorded at 3.5 K. Additional magnetic reflections (the strongest ones are marked with an asterisk) could be indexed without enlargement of the original unit cell. However, the centering of the magnetic unit cell is primitive instead of body-centered, as the additional reflections break the extinction rules of body-centered lattices ($h + k + l$ uneven). The body-centering is removed by a ferromagnetic alignment of the magnetic moments along [001] and an antiferromagnetic alignment along [110] (C-type ordering). This can be described best by two crystallographic Mn sites, one with spin-up and one with spin-down configuration, within the magnetic space group $P4_2/m'm'c'$ (Figure 3.8). Hereby, the magnetic moments are oriented along [001] and the origin of the cell is shifted by (0.5, 0, 0).

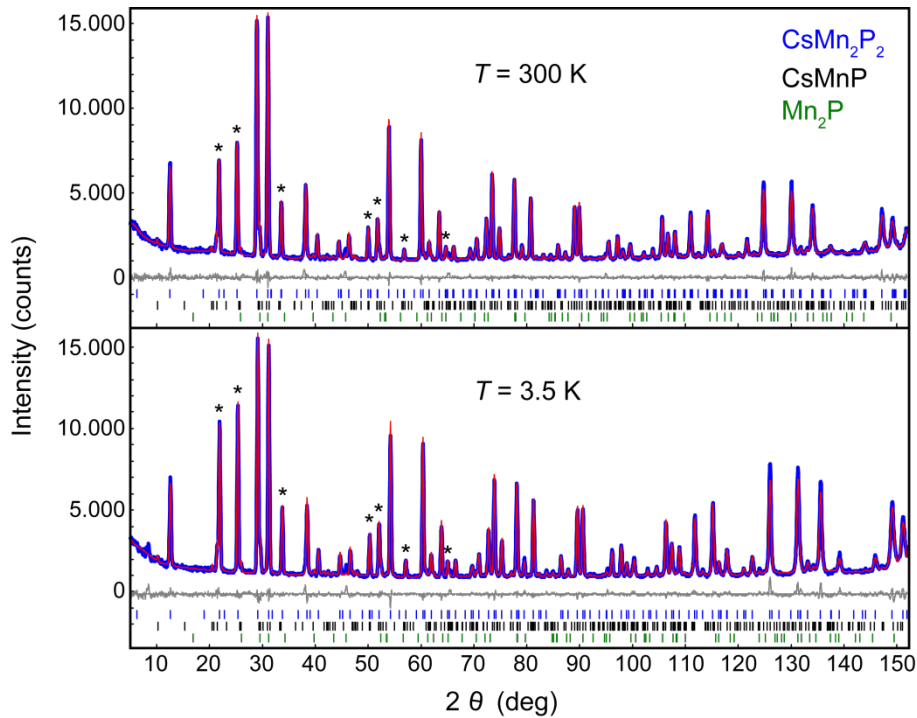


Figure 3.7: SPODI neutron powder-diffraction pattern (blue) of CsMn₂P₂ with Rietveld fit (red) at 3.5 K (bottom) and 300 K (top). The strongest magnetic reflections are marked with an asterisk.

The corresponding magnetic refinement (Figure 3.7) revealed an average magnetic moment of $2.94 \mu_B$ per Mn atom. Hereby, the magnetic structures of the impurity phases CsMnP ($T_N > 800 \text{ K}^{[55]}$) and Mn₂P ($T_N = 110 \text{ K}$) were also included. The resulting crystallographic data of CsMn₂P₂ can be found in Table 3.2.

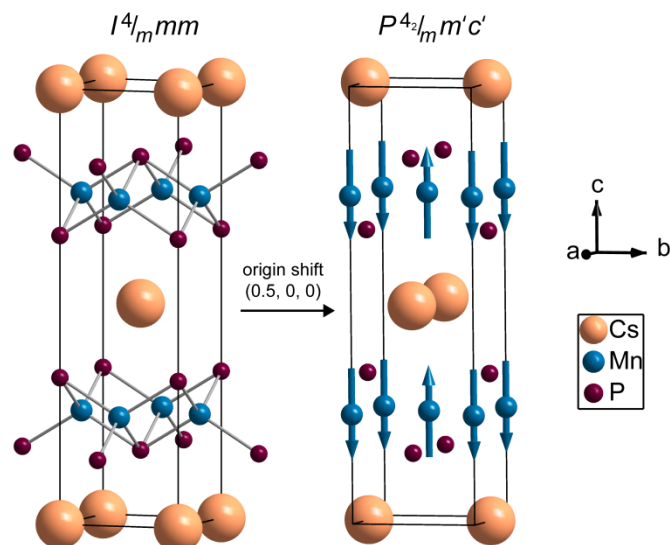


Figure 3.8: Crystal structure (left) and magnetic structure (right) of CsMn₂P₂.

Table 3.2: Crystallographic data for CsMn₂P₂ at 3.5 and 300 K obtained by neutron measurements.

CsMn ₂ P ₂		
temperature (K)	3.5	300
diffractometer	SPODI	SPODI
wavelength (nm)	0.1548	0.1548
space group	<i>P4₂/mm'c'</i> (no. 131.441)	<i>P4₂/mm'c'</i> (no. 131.441)
molar mass (g/mol)	304.7291	304.7291
lattice parameter <i>a</i> (pm)	407.54(1)	409.45(1)
lattice parameter <i>c</i> (pm)	1411.66(2)	1420.39(2)
cell volume (nm ³)	0.23446(1)	0.23813(1)
density (g/cm ³)	4.32(1)	4.25(1)
<i>Z</i>	2	2
data points	2939	2939
reflections (all phases)	522	532
refined parameters	55	61
<i>R_P</i> , <i>wR_P</i>	0.041, 0.054	0.032, 0.043
<i>R_{bragg}</i> , χ^2	0.022, 2.25	0.013, 1.80
atomic parameters		
Cs <i>2d</i> (0.5, 0, 0)	$U_{\text{iso}} = 38(3) \text{ pm}^2$	$U_{\text{iso}} = 170(4) \text{ pm}^2$
Mn1 <i>2e</i> (0, 0, 0.75)	$U_{\text{iso}} = 38(3) \text{ pm}^2$	$U_{\text{iso}} = 84(3) \text{ pm}^2$
Mn2 <i>2f</i> (0.5, 0.5, 0.75)	$U_{\text{iso}} = U_{\text{iso}}(\text{Mn1})$	$U_{\text{iso}} = U_{\text{iso}}(\text{Mn1})$
P <i>4i</i> (0.5, 0, <i>z</i>)	$z = 0.3378(1)$ $U_{\text{iso}} = 24(3) \text{ pm}^2$	$z = 0.3367(1)$ $U_{\text{iso}} = 105(3) \text{ pm}^2$
magnetic moment (Mn)	2.94(1) μ_{B}	2.29(1) μ_{B}

Surprisingly, the additional magnetic reflections of CsMn₂P₂ are observed over the whole measured temperature range, thus also at temperatures above the alleged Néel temperature of 11 K. Even at 300 K the additional reflections are already present (Figure 3.7, top). While the refined magnetic moment of 2.29 μ_{B} per Mn atom at 300 K is considerably smaller than the one found for 3.5 K, the crystal and magnetic structure remain unchanged throughout all measured temperatures.

In order to ensure that the observed additional reflections really originate from magnetic ordering, experiments with polarized neutrons were performed. Hereby nuclear and magnetic scattering contributions are separated via polarization analysis. Figure 3.9 (left) shows the obtained powder pattern at 298 K divided into nuclear and magnetic scattering. It proves the magnetic origin of the additional reflections. Thus, despite the Curie-Weiss behavior in the susceptibility measurement, CsMn₂P₂ is already antiferromagnetically ordered at 298 K.

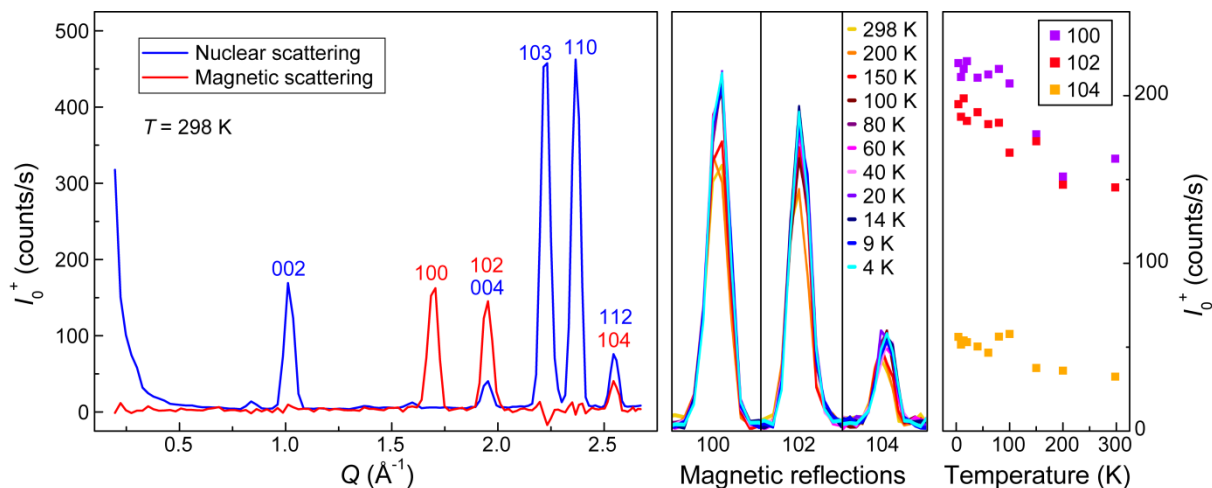


Figure 3.9: DNS polarized-neutron data of CsMn₂P₂. Left: Powder pattern at 298 K with separated nuclear (blue) and magnetic (red) scattering contributions. Middle: Magnetic reflections at different temperatures. Right: Intensity of magnetic reflections as a function of temperature.

Figure 3.9 also shows the course of the three strongest magnetic peaks with temperature (middle) and their intensity as a function of temperature (right). All three peaks become stronger upon cooling, while small discontinuities in the increase are observed. Still, the neutron data (polarized and non-polarized) do not show any structural or magnetic phase transition at 64, 17, or 11 K as indicated by susceptibility, resistivity, heat capacity, and XRD measurements.

3.3.4 μ SR experiments

Unlike neutron measurements, μ SR experiments reveal transitions in CsMn₂P₂ at 64, 17, and 11 K. They indicate changes in the system's dynamics at these temperatures.

At high temperatures ($T > 64$ K) the μ SR signal of CsMn₂P₂ is strongly damped (see polarization at 150 K, Figure 3.10) due to electronic moments. If the damping was only caused by nuclear moments, the effect would be much weaker. By applying longitudinal fields of 0 - 400 G (inset of Figure 3.10), the value at which the polarization saturates is increased, indicating that the system is static on the μ SR time scale^[56]. This is the case for truly static systems as well as for dynamic systems with fast dynamic rates beyond the MHz range. Thus, at temperatures above 64 K we find ordered electronic moments in CsMn₂P₂ which are static on the μ SR time scale.

Below 64 K, the observed oscillations in the muon polarization (see curve at 5 and 50 K in Figure 3.10) arise from muon spin precession and are evidence of a long-range magnetic order.

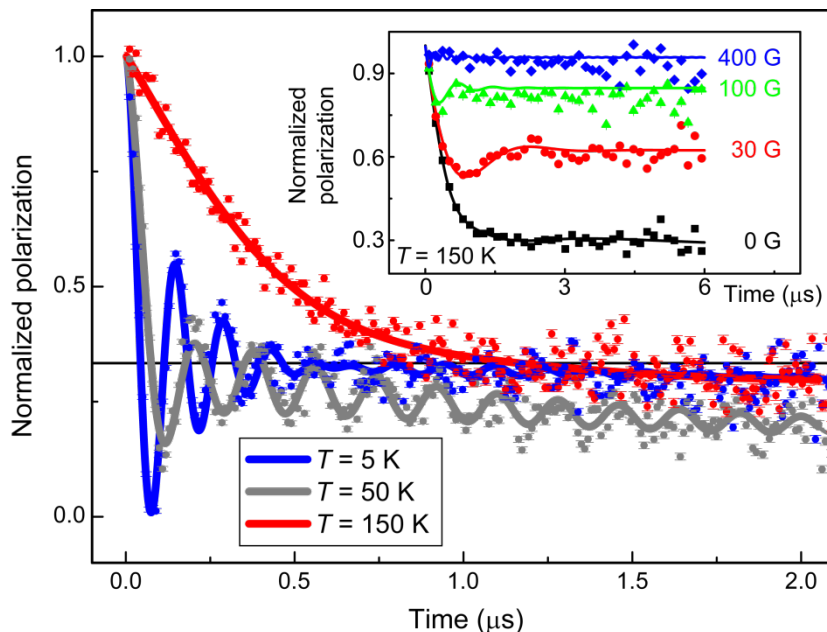


Figure 3.10: μSR data of CsMn_2P_2 at 5, 50, and 150 K. Inset: Field scan at 150 K.

A fast fourier transform (FFT) of the data (Figure 3.11, top) shows a broad distribution of the internal field (0 - 200 G at 70 K; 0 - 600 G at 10 K). In order to describe this properly, the data were fitted with a Bessel and a cosine function (both damped) and a longitudinal tail. The resulting fields of the Bessel and cosine functions and the longitudinal relaxation rate are shown in Figure 3.11 (bottom). Both fields (Bessel and cosine) start increasing strongly at 64 K, indicating a phase transition into the observed long-range ordered state.

At low temperatures (17 K and 11 K) further changes occur in the μSR spectra. A low-field part (0 - 200 G) of the internal field begins to disappear at 17 K and at about 11 K a new contribution at ~ 550 G appears (see FFT, Figure 3.11, top, left). Also, at 17 K the Bessel function field reaches a turning point and the field of the cosine function shows a sudden jump before both fields start saturating close to 11 K (Figure 3.11, bottom, left). Additionally, the fitted longitudinal relaxation rate (Figure 3.11, bottom, right) indicates that the long-range order is quasi-static only (dynamic on a low MHz time scale) in the region below 64 K.

Taking into account the previously described physical properties and neutron measurements, these results point to the following: CsMn_2P_2 is already antiferromagnetically ordered at 300 K and exhibits a time-averaged magnetic component and, in addition, a fast dynamic component. While the latter component is too fast to be observed by μSR in the high-temperature regime above 64 K, it dramatically slows down to the low MHz range at temperatures lower than 64 K and the system becomes truly static only at the lowest measured temperatures. The low-temperature magnetic ground state is reached through a sequence of three transitions at 64, 17, and 11 K. As μSR is a volume-sensitive local-probe

technique it also provides information about the fraction of the sample which undergoes the transition. Here, all three transitions are observable in essentially the full sample volume.

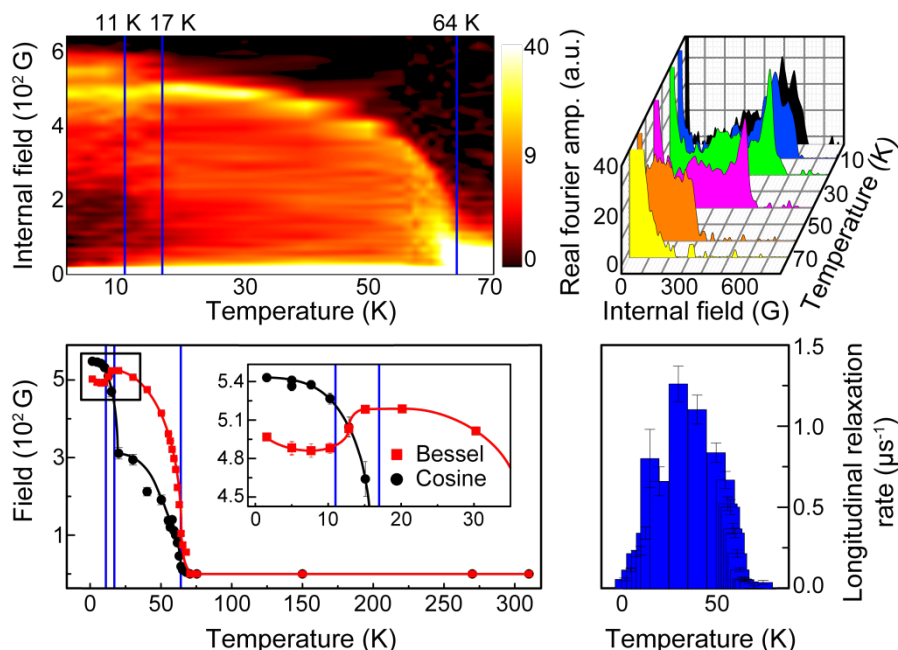


Figure 3.11: Top: Fast fourier transform of the μ SR data; color-coded contour plot (left) and individual plots at different temperatures (right). Bottom: Fitted fields of the Bessel and cosine functions (left) and longitudinal relaxation rate (right) as a function of temperature. The three temperatures at which changes are detected are marked with blue lines.

3.4 Conclusion

The magnetic properties of CsMn₂P₂ turn out to be far more complex than supposed earlier. While the magnetic susceptibility shows a Néel temperature of 11 K and Curie-Weiss behavior above this temperature, neutron measurements unambiguously detect a C-type antiferromagnetic order within the magnetic space group $P4_2/m'm'c'$ already at room temperature. First indications for understanding these seemingly contradictory results are found by μ SR measurements. These exhibit clear evidence of dynamics in the magnetism of CsMn₂P₂. Accordingly, static magnetism in CsMn₂P₂ only exists at low temperatures. The system reaches this magnetic ground state through three transitions at 64, 17, and 11 K, which are detected in μ SR, heat capacity, resistivity, susceptibility, and XRD measurements. These transitions are very likely related to changes in the dynamics of the system, for example due to spin-reorientation processes. As the time scales of the applied experimental techniques strongly differ ($\sim 10^{-2}$ s for susceptibility, $\sim 10^{-12}$ s for neutron, and $\sim 10^{-6}$ s for μ SR measurements) a dynamic system like CsMn₂P₂ can appear very differently when observed by each of them.

One possible approach to explain the unexpected magnetic behavior of CsMn₂P₂ is based upon differences in the inter- and intralayer ordering of the manganese moments. Possibly, at room temperature the manganese moments are already antiferromagnetically ordered within the tetrahedral layers but the interlayer correlation is not yet strong enough. Therefore, the magnetic moments in neighboring layers still fluctuate with regard to each other. In the comparably slow susceptibility measurement, averaging over the fluctuating orientations, the compound doesn't appear to be magnetically ordered, while the comparably fast neutrons already detect the ordered moments within the layers. Then, at low temperatures, the moments of neighboring layers also align and a long-range magnetic order is detected in the magnetic susceptibility. As the magnetic moments of neighboring layers, stacked along *c*, align ferromagnetically to each other, this could lead to a small repulsion between the layers. Therefore, this explanatory approach would also fit together with the low temperature XRD data, where an enlargement of the cell is observed below 17 and 11 K, primarily along the *c* axis. Theoretical calculations supporting these considerations will be discussed in Chapter 4.

Additionally, it is noticeable that the average effective magnetic moment per manganese atom obtained from susceptibility data ($n_{\text{eff}} = 3.31$) and the magnetic moment revealed by neutron measurements ($2.94 \mu_{\text{B}}$ per Mn atom at 3.5 K) are rather small for the average value of 4.5 unpaired electrons per Mn^{2.5+} atom (expected moment from spin-only formula: $5.41 \mu_{\text{B}}$). Thus, we either find a low-spin configuration for Mn with an average of only 2.5 unpaired electrons per Mn atom (expected moment from spin-only formula: $3.35 \mu_{\text{B}}$) or not all manganese atoms are involved in the magnetic order.

By assuming only one magnetic center per formula unit instead of two, susceptibility data reveal an effective moment of $4.68 \mu_{\text{B}}$, which is close to the theoretically expected moment of $4.9 \mu_{\text{B}}$ for Mn³⁺. Analogously, neutron data would indicate a magnetic moment of $5.88 \mu_{\text{B}}$, if only 50 % of the sample volume was magnetic. This is close to the $5.92 \mu_{\text{B}}$ expected for Mn²⁺. However, a phase separation of Mn²⁺ areas with and Mn³⁺ areas without magnetic ordering is not supported by the μSR results.

Despite the large number of experimental techniques applied, a definite and conclusive explanation for the exceptional magnetic behavior of CsMn₂P₂ cannot be given at this point. So far, it appears to be a unique phenomenon, as no indications of a similar behavior are found in literature. Additional experiments are necessary in order to solve the mystery about the magnetic properties of CsMn₂P₂. For example, inelastic neutron scattering experiments can contribute to this.

Very likely, the Mn²⁺/Mn³⁺ mixed valence plays a decisive role in the unusual magnetic behavior of CsMn₂P₂. Therefore, it is also interesting to study the magnetic properties of RbMn₂P₂^[53] more closely. It is the only other known AMn₂P₂ (*A* = alkali metal) compound of

this structure type. Just like CsMn₂P₂ it is an Mn²⁺/Mn³⁺ mixed-valent compound. The magnetic susceptibility is very similar to the one obtained for CsMn₂P₂ and reveals a Néel temperature of 10 K. It is highly probable that RbMn₂P₂ also exhibits interesting, possibly dynamic magnetic properties due to the mixed valence of Mn and that neutron measurements would also reveal a magnetic ordering already at higher temperatures than expected from susceptibility data.

Returning to the initial gedanken experiment of CsMn₂P₂ as strongly hole-doped BaMn₂P₂ and thus a model system for iron-based superconductors, no final conclusion can be drawn about how hole doping affects the magnetism of this system as the dynamic magnetism of CsMn₂P₂ is still not fully understood. Probably, the manganese magnetism is weakened compared to BaMn₂P₂ but it is dominated by Mn²⁺/Mn³⁺ interactions and more complex than expected.

4 The electronic structure of CsMn_2P_2

4.1 Introduction

The dynamics of the magnetism in CsMn_2P_2 are still not fully understood. However, the structure of the magnetic ground state was successfully solved by neutron-diffraction measurements: the manganese moments order antiferromagnetically (AFM) according to the so-called C type (ferromagnetic order along [001], AFM order along [110]), whereby the moments are oriented along [001]. It is therefore possible to study the electronic structure of magnetically ordered CsMn_2P_2 . One approach to this has already been presented in [53], whereby the true magnetic order had not been known by that time. Therefore, three different, hypothetical models were discussed and compared: a non-magnetic one, a ferromagnetically ordered one, and a G-type like AFM ordered one (AFM order along [001] and [110]). This G-type ordering was chosen as probable because it had been found for the isostructural barium compound BaMn_2P_2 ^[52].

For the non-magnetic model a high density of states (DOS) was found at the Fermi level (E_F) which, as expected, was strongly reduced by magnetic ordering. However, for the G-type AFM ordered model, E_F is positioned at a local maximum within the DOS. This unfavorable situation was interpreted as a first indication that the assumed G type does not constitute the actual magnetic ordering in CsMn_2P_2 , which as we know now, is in fact true.

In this chapter, the electronic structure of CsMn_2P_2 in its experimentally determined magnetic ground state will be presented and compared to the hypothetical non-magnetic and G-type like ordered models. Additionally, the exchange coupling between one manganese atom and its neighbors will be discussed based on spin-polarized relativistic Korringa-Kohn-Rostoker (SPR-KKR) calculations which provide indications of possible dynamics within the system.

4.2 Calculation details

Electronic band structure calculations for a non-magnetic, a G-type AFM, and a C-type AFM model were performed with the WIEN2k program package^[42]. The separation energy for core and valence states was -6 Ry (for both antiferromagnetic models) and -7 Ry (for the non-magnetic model). For a primitive lattice, 680 irreducible k points, and for a body-centered lattice, 828 irreducible k points were used. The experimentally obtained lattice parameters ($a = 409.5$ pm, $c = 1420.5$ pm) were used, relaxing the structures by minimization of the Hellman-Feynman forces with variation of the z parameter of phosphorus. The muffin-tin

sphere radii R_{MT} were 2.50 a.u. for Cs, 2.4 a.u. for Mn, and 1.87 a.u. for P. WIEN2k performed the calculations of the non-magnetic and the *G*-type antiferromagnetic model (body-centered lattices) for half a unit cell (5 atoms) and the calculation of the *C*-type AFM order (primitive lattice) for a whole unit cell (10 atoms). All results presented here have been adjusted to each other in order to be comparable.

Exchange coupling parameters for CsMn₂P₂ were calculated with the SPR-KKR package^[45,46] according to the method described in Chapter 2.10.

4.3 Results and discussion

The calculated DOS for the hypothetical non-magnetic and *G*-type AFM models, and for the experimentally determined *C*-type AFM structure of CsMn₂P₂ can be found in Figure 4.1 along with unit cells of the corresponding structures. The area around the Fermi level is clearly dominated by manganese states, which are mainly Mn *d* states. Cesium and phosphorus contributions are predominantly found at lower energies close to -10 eV. Consequently, the magnetic ordering of Mn *d* electrons affects the area around E_{F} . The total density of states at the Fermi level is 10.9 states/eV for the non-magnetic model, 8.7 states/eV for the *G*-type AFM model, and only 4.8 states/eV for the *C*-type AFM model. Thus, the *C*-type ordering reduces the DOS of a non-magnetic CsMn₂P₂ by 55 % at E_{F} , while a hypothetical *G*-type ordering leads to a reduction of only 20 %.

A closer look at the DOS around 0 eV (Figure 4.2) reveals that the Fermi level lies at the slope of a maximum within the DOS for the non-magnetic model and at a local maximum for the *G*-type model. This local maximum at E_{F} has already been interpreted in [53] as indication that this ordering does not reflect the actual magnetic structure in CsMn₂P₂. A different situation is found for the *C*-type model where E_{F} is positioned at a local minimum of the density of states. Therefore, the DOS of the experimentally determined *C*-type antiferromagnetic ordering is clearly more favorable than the DOS of the other two hypothetical models.

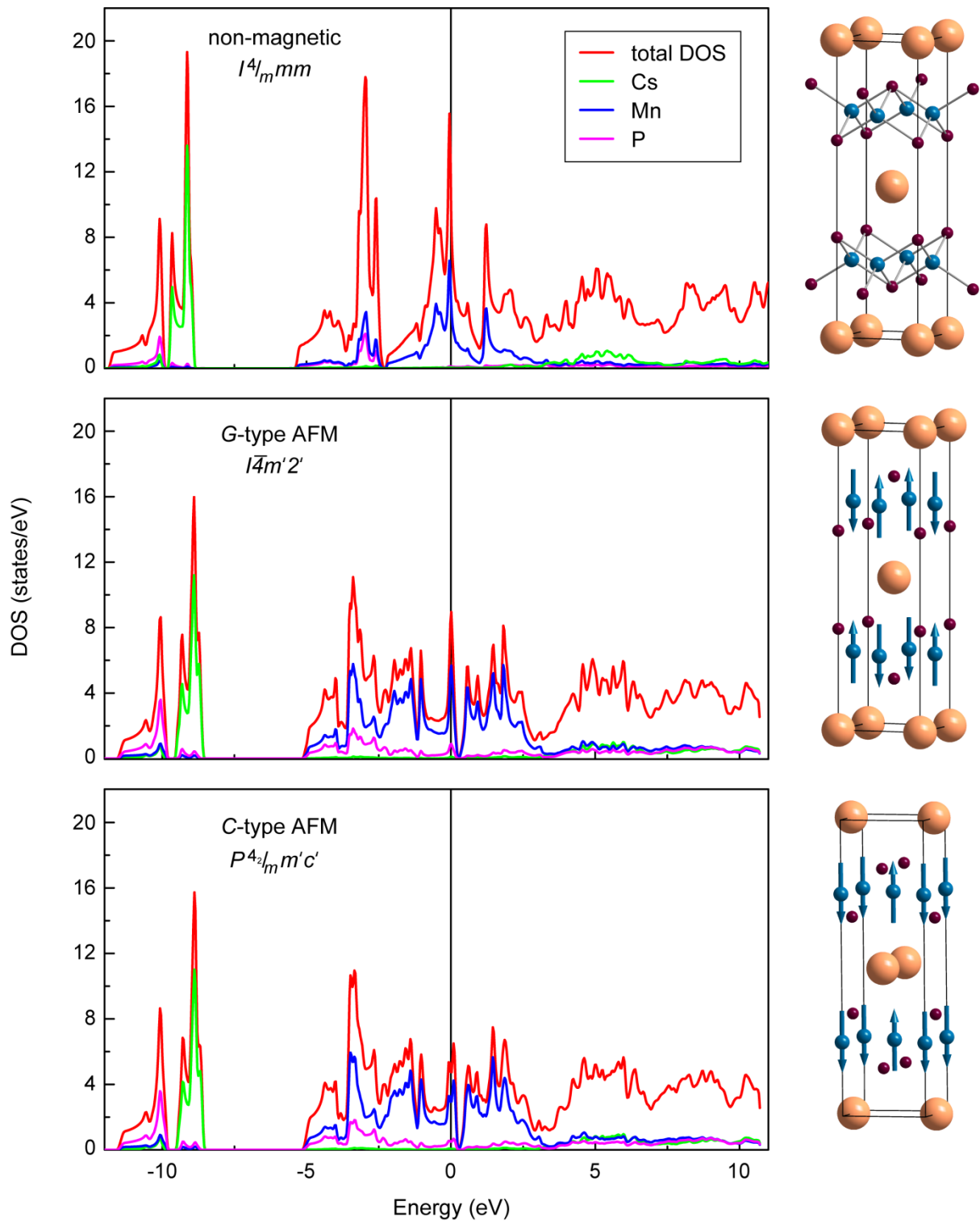


Figure 4.1: DOS of CsMn_2P_2 calculated for a non-magnetic model in the space group $I4/mmm$ (top), a G-type AFM model in the space group $I\bar{4}m'2'$ (middle), and the experimentally determined C-type AFM order in the space group $P4_2/m'm'c'$ (bottom) with corresponding unit cells (right).

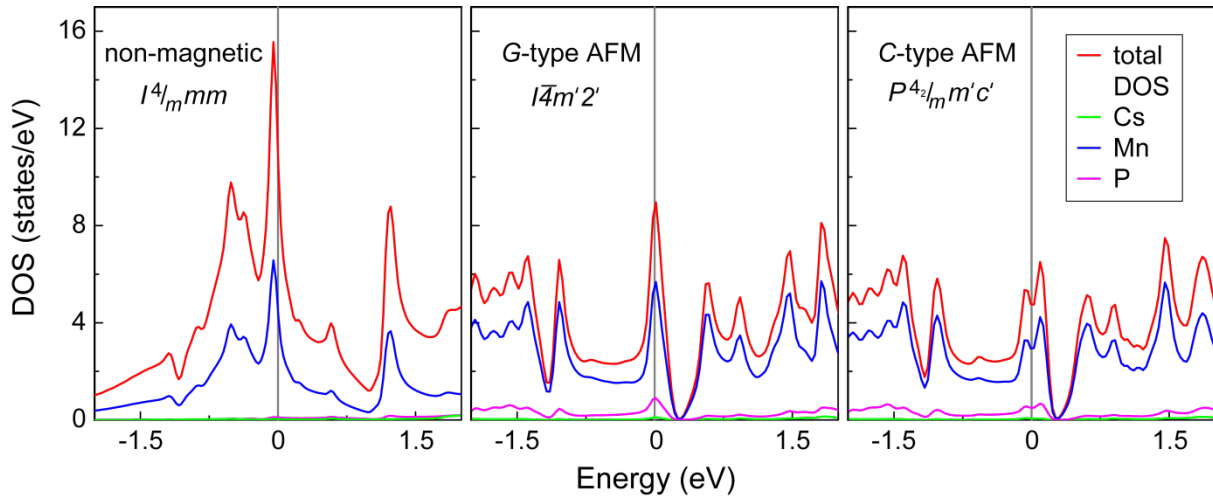


Figure 4.2: Enlarged DOS section of CsMn₂P₂ for the non-magnetic (left), G-type (middle), and C-type (right) antiferromagnetic model.

An overview of the total energy, the optimized z parameter of the phosphorus site, the minimized Hellman-Feynman forces F , and the resulting magnetic moment per manganese atom is given in Table 4.1. Just like the DOS, the total energy indicates that the C-type ordering exhibits the energetically most favorable electronic structure. While the total energy per unit cell of the G-type ordered model is 1.3029 eV lower than the total energy of the non-magnetic model, E_{tot} of the C-type structure is reduced by 1.3506 eV as compared to the non-magnetic model. This corresponds to a difference of 65 kJ/mol between C-type and non-magnetic model and 2 kJ/mol between C-type and G-type model.

The optimized z parameter of phosphorus is smaller than the experimentally obtained one for all three calculated models. Hereby both antiferromagnetic models result in the same value, which is closer to the experiment than the one found for the non-magnetic model. Also, the resulting magnetic moments of $2.95 \mu_{\text{B}}$ and $2.96 \mu_{\text{B}}$ for the G- and C-type model, respectively, are very close to each other and to the magnetic moment revealed by neutron measurements ($2.94 \mu_{\text{B}}$). Hence, regarding only $z(\text{P})$ and $\mu(\text{Mn})$, both antiferromagnetic models are equally probable. However, the density of states and the total energy clearly point to the C-type ordering as the more favorable structure, which is in perfect agreement with the experimentally obtained results.

Figure 4.3 shows the calculated band structures for the non-magnetic (left) and the C-type antiferromagnetically ordered model (right). The corresponding Brillouin zones including the k points chosen for the plotted band structures are also displayed. The direct comparison shows how the bands are altered by the magnetic order: a gap in the band structure appears between ~ 0.2 and ~ 0.3 eV. Raising the Fermi level into this gap by introducing more electrons into the system should therefore lead to a semiconducting or isolating material.

Conceptually, such an electron doping would lead to an electronic structure similar to the one of BaMn_2P_2 , which, as discussed before, is in fact a semiconductor.

Table 4.1: Results of the DFT calculations for non-magnetic, G-type, and C-type AFM CsMn_2P_2 .

	non-magnetic	G-type AFM	C-type AFM
E_{tot} (eV) / unit cell	-587322.8710	-587324.1739	-587324.2216
F (eV)	0.0071	0.0020	0.0003
optimized $z(\text{P})$	0.3150	0.3298	0.3298
$\mu(\text{Mn})$	-	$2.95 \mu_{\text{B}}$	$2.96 \mu_{\text{B}}$

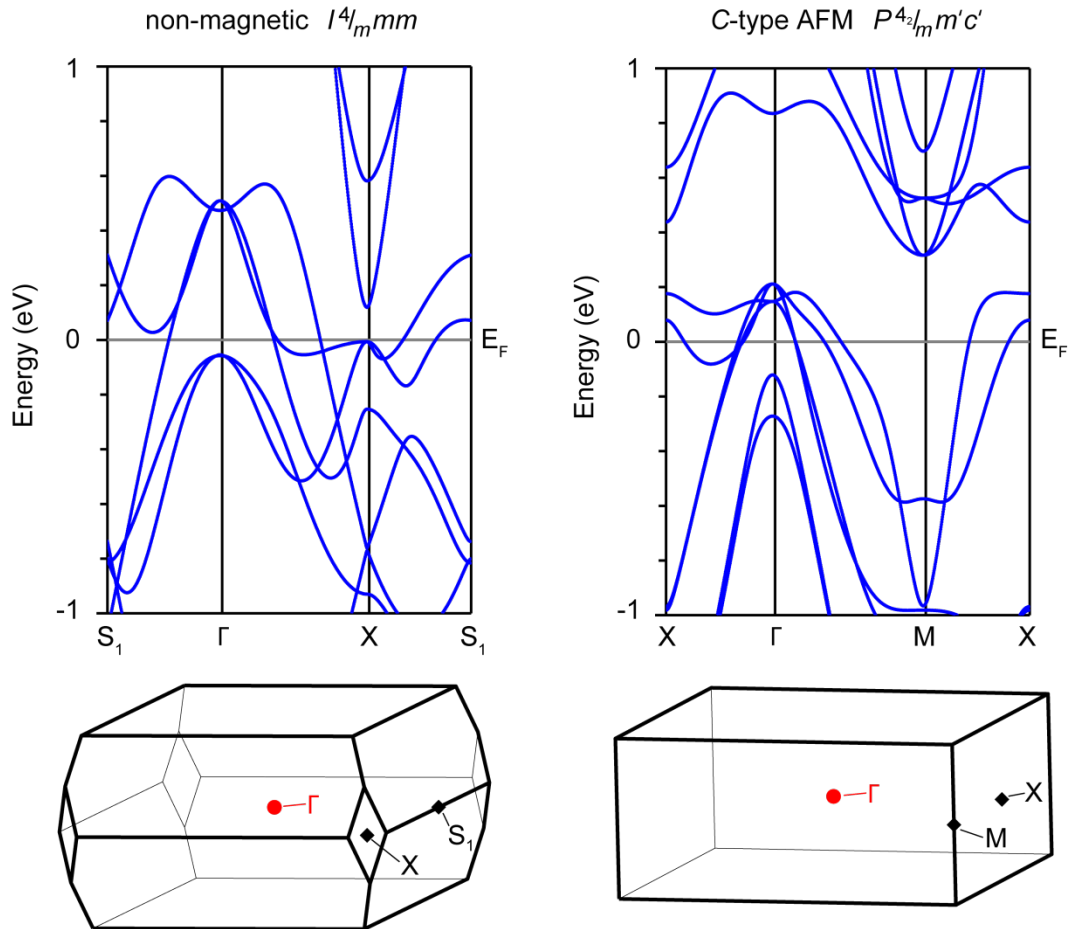


Figure 4.3: Band structure of CsMn_2P_2 for the non-magnetic (left) and C-type antiferromagnetic (right) model. Bottom: Corresponding Brillouin zones with marked relevant points.

In order to obtain indications for possible dynamics within CsMn₂P₂, the exchange coupling parameters J_{ij} between neighboring atoms have been calculated. Figure 4.4 shows the resulting J_{ij} between one atom Mn_{*i*} and its neighbors Mn_{*j*} as a function of the distance between both atoms. For an easier understanding of the data, the first five data points and the corresponding pairs of atoms have been color coded.

The obtained results confirm a strong negative exchange coupling between closest manganese neighbors (marked in red) which are aligned antiferromagnetically to each other in the experimentally determined C-type structure. Mn atoms with a distance of one lattice parameter a (marked in blue) exhibit a weak positive coupling and manganese atoms separated by one length of the [110] diagonal (marked in green) show a strong positive coupling. Both atom pairs are found to align ferromagnetically in the C-type ordering. Manganese atoms separated by $\frac{1}{2}\sqrt{10} a$ (marked in orange) show a weak negative exchange coupling and are also experimentally found to align antiferromagnetically to each other. The coupling between two (001) planes of manganese atoms (marked in pink) is found to be negative, therefore an antiferromagnetic alignment of these planes (G type) would be expected. However, neutron diffraction measurements revealed a ferromagnetic alignment of the planes (C type). This discrepancy between theory and experiment is not unusual, as it is especially complicated to describe the correct electronic situation for manganese compounds by theoretical calculations.

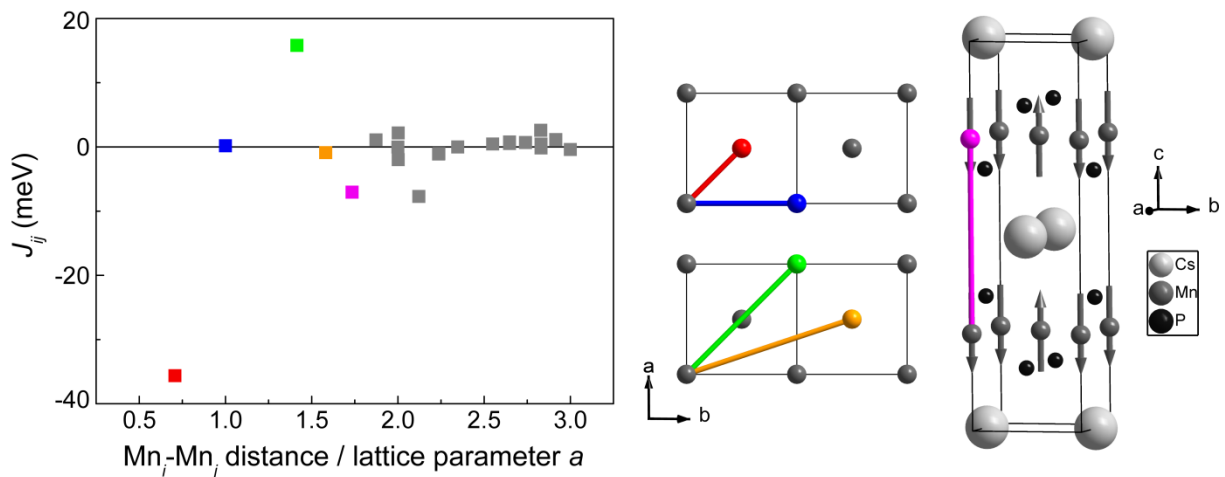


Figure 4.4: Exchange coupling parameters J_{ij} calculated for the Mn atoms in CsMn₂P₂ (left) and visualization of the corresponding coupling pairs (right).

Nevertheless, the calculations reveal a considerably weaker coupling between two planes than within the plane, as the strongest intra-plane coupling is five times as big as the

strongest inter-plane coupling. The ordering temperatures can be estimated very roughly according to

$$T_N \approx J_{01} \cdot n_{01},$$

where J_{01} is the Mn-Mn AFM exchange coupling with the first-neighbor Mn atoms and n_{01} is the number of first-neighbor Mn atoms. This leads to intra-plane ordering at ~ 1400 K and inter-plane ordering at ~ 100 K. Thus, the inter-plane ordering temperature is expected to be approximately one order of magnitude smaller than the intra-plane ordering temperature. This would be consistent with the idea that the experimentally observed dynamics are due to weak inter-plane coupling, which was presented in Chapter 3.

For the sake of completeness, the exchange coupling parameters between manganese atoms and neighboring phosphorus or cesium atoms are depicted in Figure 4.5. As expected, only the nearest neighbors exhibit a very weak positive coupling, whereby the coupling between Mn and Cs is clearly smaller than the coupling between Mn and P atoms.

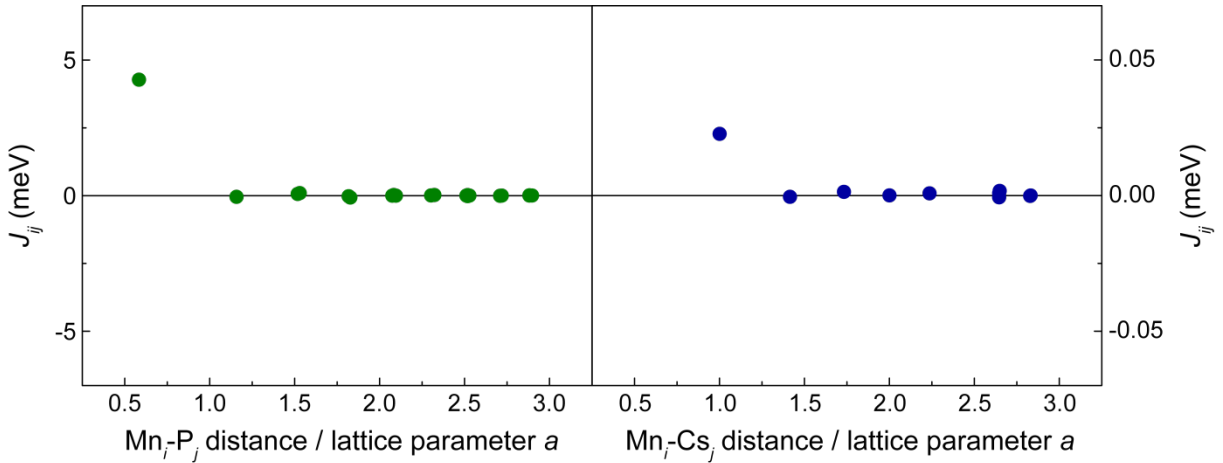


Figure 4.5: Exchange coupling parameters J_{ij} for CsMn₂P₂ between Mn and neighboring P (left) or Cs atoms (right).

4.4 Conclusion

The electronic structure of CsMn₂P₂ was calculated for hypothetical non-magnetic and G -type AFM models and for the experimentally detected C -type AFM ordered structure. In agreement with the experimental data, the density of states around the Fermi level as well as the total energy per unit cell indicate the C -type ordering as most favorable one of the three models. Additionally, the resulting magnetic moment per manganese atom is very close to the one obtained by neutron measurements.

Calculations of exchange coupling parameters between neighboring manganese atoms within MnP tetrahedral planes predict the experimentally obtained alignment of manganese moments. However, inter-plane alignment is predicted antiferromagnetically, while experiments revealed ferromagnetic alignment. Still, the intra-plane coupling is considerably stronger than the inter-plane coupling, which could be the origin of the experimentally observed dynamics within the magnetism of CsMn_2P_2 . For final conclusions this theory needs to be verified by further experiments.

5 Modifying the magnetism in CsMn_2P_2

5.1 Introduction

When studying a complicated system like CsMn_2P_2 with an $\text{Mn}^{2+}/\text{Mn}^{3+}$ mixed valence and unexpected dynamic magnetic properties as described in Chapter 3, it can be useful not to concentrate only on the system as it is, but to examine slightly modified versions of it. The physical properties of the original system CsMn_2P_2 exhibit several anomalies, some of which are detectable with different experimental methods. By partly changing the structure, for example by substitution of one of the elements, some of the features might be less pronounced or completely suppressed, thereby leading to a system which is easier to interpret. Of course, the contrary, *i.e.* obtaining a more complicated system with additional anomalies, can also be the case.

In this chapter four different attempts of modifying the magnetic properties of CsMn_2P_2 will be presented. First, isoelectronic doping by substitution of Cs by Rb. While the magnetic susceptibilities of CsMn_2P_2 and RbMn_2P_2 are very similar to each other, resistivity measurements revealed distinct differences between the two compounds^[53]. The temperature-dependent resistivity of CsMn_2P_2 exhibits anomalies which, as was shown by μSR measurements, are related to changes in the system's dynamics. Although up to now no μSR experiments were performed on RbMn_2P_2 , the absence of anomalies in the resistivity might indicate weaker or different magnetic dynamics in this compound. A completely static magnetism is also possible but less probable, as the alleged origin of the dynamic effects, the manganese mixed valence, is also found in the rubidium compound. Therefore, the solid solution $\text{Cs}_{1-x}\text{Rb}_x\text{Mn}_2\text{P}_2$ could be a means to tune the dynamic effects of the magnetism of the cesium compound.

The second attempt presented here is an electron doping by substitution of Cs by Ba. The resulting solid solution could be especially interesting as BaMn_2P_2 is an Mn^{2+} compound with a well-examined magnetic order where no indications for dynamic effects have been reported. Additionally, the magnetic structure of BaMn_2P_2 (*G* type) is different from the cesium compound (*C* type). Thus, one would expect that within $\text{Cs}_{1-x}\text{Ba}_x\text{Mn}_2\text{P}_2$ the dynamics of CsMn_2P_2 are suppressed and the ordering should change from *C* to *G* type at a certain barium content.

As third and fourth option, O_2 - and H_2 -annealing have been attempted. Modifying the oxidation state of CsMn_2P_2 seems to be a very promising approach to alter the magnetic properties, which are probably dominated by the mixed valence of manganese.

5.2 Experimental details

For the synthesis of Cs_{1-x}Rb_xMn₂P₂ samples mixtures of Cs₄P₆, Rb₄P₆, Mn, and P with 5 % excess of Cs and Rb were sealed in niobium crucibles in sealed silica ampoules. The samples were heated up to 1073 K for 14 h at rates of 50 K/h for heating and cooling. Cs_{1-x}Ba_xMn₂P₂ samples were synthesized by mixing Cs₄P₆, Ba₅P₄, Mn, and P with 5 % excess of Cs and Ba. The mixtures were sealed and heated as described before.

The O₂-annealing was realized by exposing a sample of CsMn₂P₂, synthesized by the method described in Chapter 3.2, to an oxygen atmosphere for two hours. For H₂-annealing a CsMn₂P₂ sample was heated up to 373 K under a constant hydrogen flow for one hour.

The samples were characterized by X-ray powder-diffraction measurements using the STOE diffractometer (Mo-K α_1 radiation). Temperature-dependent X-ray data between 300 K and 10 K were recorded using the Huber G670 diffractometer with Co-K α_1 radiation. For Rietveld refinements of the data the TOPAS package^[30] was used with spherical harmonics functions to describe the preferred orientation of the crystallites. Shape anisotropy effects were described by the approach of *Le Bail* and *Jouanneaux*^[31]. Additionally, SQUID magnetic measurements and resistivity measurements were performed.

5.3 Isoelectronic doping in Cs_{1-x}Rb_xMn₂P₂

Samples of Cs_{1-x}Rb_xMn₂P₂ with nominal rubidium contents $x_{\text{nom}} = 0.2$ and 0.8 were successfully prepared with a main phase fraction of 87 % and 80 %, respectively (Figure 5.1). Mn₂P and CsMnP or RbMnP occur as impurity phases. Rietveld refinements revealed refined rubidium contents of $x_{\text{ref}} = 0.18(1)$ and $0.76(1)$, which deviate from the nominal contents by 10 % and 5 %, respectively. The corresponding crystallographic data are compiled in Table 5.1.

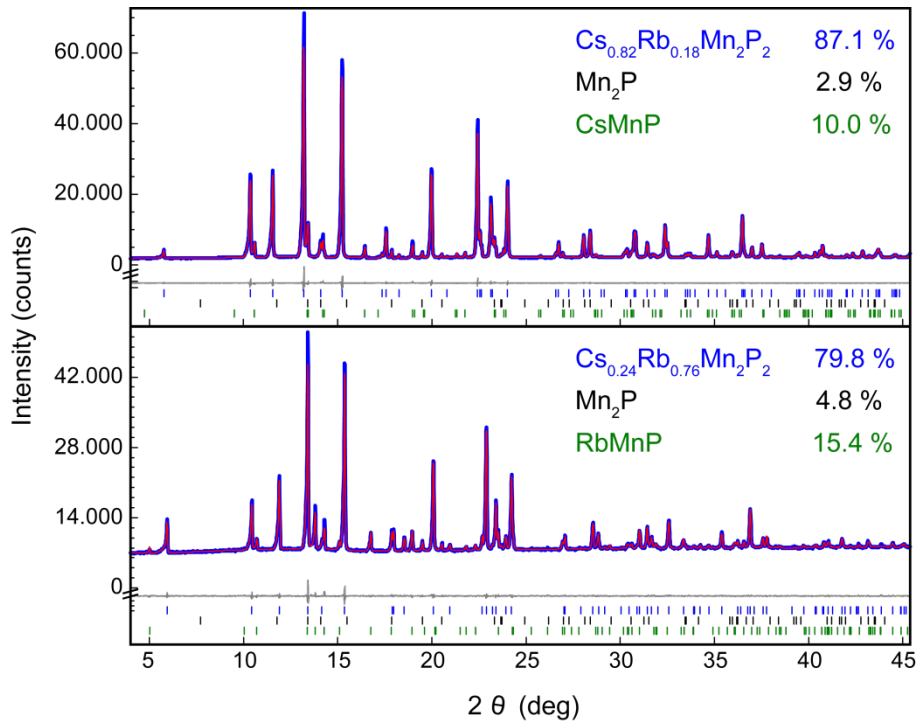


Figure 5.1: X-ray powder-diffraction pattern (blue) of Cs_{0.82}Rb_{0.18}Mn₂P₂ (top) and Cs_{0.24}Rb_{0.76}Mn₂P₂ (bottom) with Rietveld refinements (red).

Table 5.1: Crystallographic data for Cs_{1-x}Rb_xMn₂P₂ obtained by Rietveld refinements.

	Cs _{1-x} Rb _x Mn ₂ P ₂	
refined Rb content <i>x</i>	0.18(1)	0.76(1)
space group	<i>I4/mmm</i> (no. 139)	<i>I4/mmm</i> (no. 139)
molar mass (g/mol)	296.1903	268.6765
lattice parameter <i>a</i> (pm)	409.14(2)	406.97(3)
lattice parameter <i>c</i> (pm)	1410.2(1)	1368.0(1)
cell volume (nm ³)	0.23606(3)	0.22657(4)
density (g/cm ³)	4.17(1)	3.94(1)
<i>Z</i>	2	2
data points	2760	2760
reflections (all phases)	210	199
refined parameters	71	92
<i>R</i> _p , <i>wR</i> _p	0.031, 0.046	0.012, 0.018
<i>R</i> _{bragg} , <i>χ</i> ²	0.007, 2.598	0.004, 1.726
atomic parameters		
Cs/Rb 2 <i>a</i> (0, 0, 0)	<i>U</i> _{iso} = 161(4) pm ²	<i>U</i> _{iso} = 168(8) pm ²
Mn 4 <i>d</i> (0, 0.5, 0.25)	<i>U</i> _{iso} = 127(6) pm ²	<i>U</i> _{iso} = 90(8) pm ²
P 4 <i>e</i> (0,0, <i>z</i>)	<i>z</i> = 0.3372(2)	<i>z</i> = 0.3408(2)
	<i>U</i> _{iso} = 119(7) pm ²	<i>U</i> _{iso} = 110(10) pm ²

The lattice parameters a and c show a linear decrease with increasing rubidium content together with the ones of CsMn₂P₂ ($a = 409.48(1)$ pm, $c = 1420.41(2)$ pm) and RbMn₂P₂ ($a = 406.24(1)$ pm, $c = 1349.19(3)$ pm)^[53]. This leads to a shortening of the Mn-P distance (239.0(1) pm for $x = 0$ and 238.0(1) pm for $x = 1$ ^[53]), although the z parameter of the phosphorus site increases and the MnP_{4/4} tetrahedra are elongated along c .

As the crystallographic data indicates that the partial substitution of Cs by Rb was successful, it is interesting to study how this affects the properties of the compounds and if it really modifies the complicated magnetic features found in CsMn₂P₂. Therefore, the compound with $x = 0.18$ was examined regarding possible structural transitions at low temperatures, the magnetic susceptibility and resistivity.

Temperature-dependent XRD measurements revealed that both lattice parameters a and c , and therefore also the cell volume, continuously decrease upon cooling over the whole measured temperature range of 300 K to 10 K (Figure 5.2). Between 20 K and 15 K a small plateau is found, where the values stay nearly constant but no re-increase, as in CsMn₂P₂ (Chapter 3), is observed. Thus, already at a rubidium content of 18 % the originally existent structural changes of CsMn₂P₂ are completely suppressed.

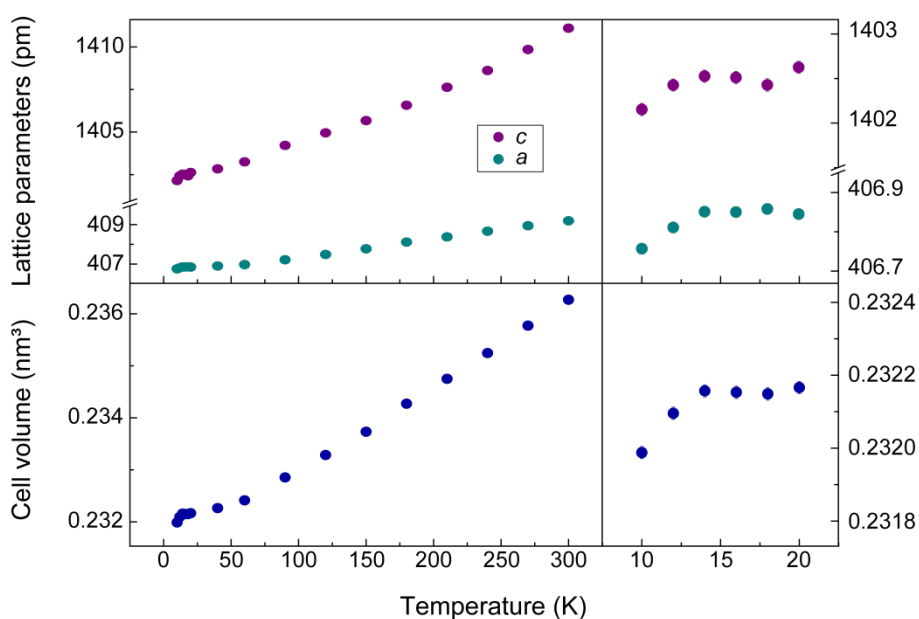


Figure 5.2: Refined lattice parameters (top) and cell volume (bottom) of Cs_{0.82}Rb_{0.18}Mn₂P₂ as a function of temperature with enlarged low-temperature sections (right).

The magnetic susceptibility of Cs_{0.82}Rb_{0.18}Mn₂P₂ (Figure 5.3) indicates an antiferromagnetic transition at 10.6 K. Above this temperature, Curie-Weiss behavior is observed. This is very similar to the results obtained for CsMn₂P₂ ($T_N = 11$ K, Chapter 3) and RbMn₂P₂ ($T_N = 10$ K^[53]). A Curie-Weiss fit reveals an effective magnetic moment of 4.79(1) μ_B per

formula unit. This corresponds to an average effective magnetic moment of $3.39 \mu_B$ per manganese atom and is very close to the value found for CsMn₂P₂ ($3.31 \mu_B$). No additional anomalies or indications of magnetic impurities are observed.

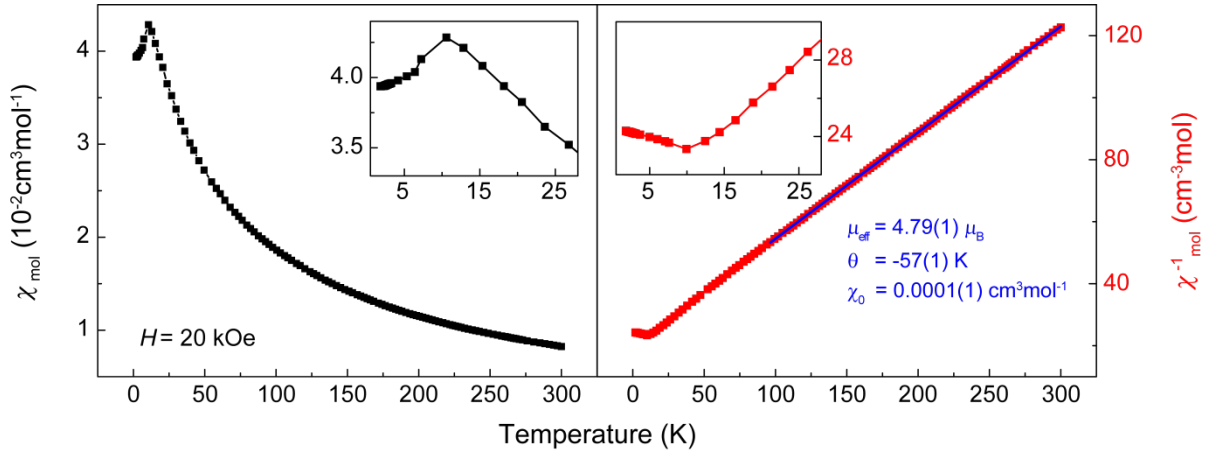


Figure 5.3: Magnetic susceptibility (left) and inverse magnetic susceptibility (right) of Cs_{0.82}Rb_{0.18}Mn₂P₂ with Curie-Weiss fit (blue). Insets: Enlarged low-temperature sections.

The resistivity measurement of Cs_{0.82}Rb_{0.18}Mn₂P₂ (Figure 5.4, left) shows two anomalies, which closely resemble the results obtained for CsMn₂P₂ (Figure 5.4, bottom, right), while not being completely similar. One broad anomaly, beginning at 64 K (just as found for the cesium compound), and an increase in resistivity starting at 22 K are found. This increase is more abrupt in CsMn₂P₂, where it starts at 17 K. For comparison, the resistivity of RbMn₂P₂ (Figure 5.4, top, right), which exhibits no anomalies between 3.5 and 300 K, is also depicted. More details about the synthesis and the properties of RbMn₂P₂ can be found in [53].

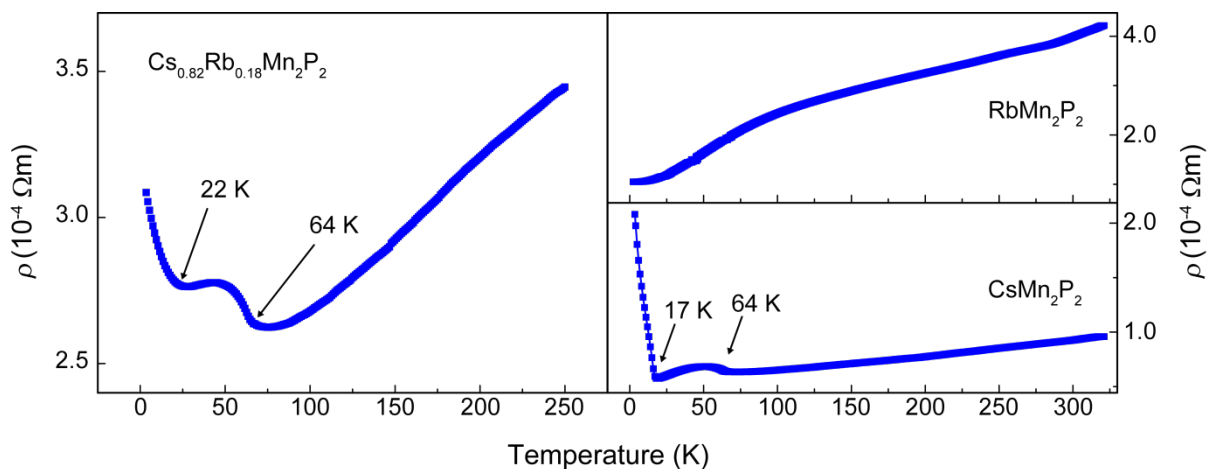


Figure 5.4: Resistivity measurements of Cs_{0.82}Rb_{0.18}Mn₂P₂ (left), CsMn₂P₂ (bottom, right), and RbMn₂P₂ (top, right).

Adding together the results obtained by temperature-dependent XRD, susceptibility, and resistivity measurements, the physical properties of $\text{Cs}_{0.82}\text{Rb}_{0.18}\text{Mn}_2\text{P}_2$ clearly differ from those of CsMn_2P_2 . While the structural changes at low temperatures are already suppressed, the anomalies in the resistivity, which are probably related to dynamic effects in CsMn_2P_2 , are slightly altered but still present. Thus, the compound with $x = 0.18$ can be expected to exhibit at least some of the dynamic effects of the parent compound. However, higher rubidium levels might suppress not only the structural transition but also the dynamics of the magnetism.

5.4 Electron doping in $\text{Cs}_{1-x}\text{Ba}_x\text{Mn}_2\text{P}_2$

$\text{Cs}_{1-x}\text{Ba}_x\text{Mn}_2\text{P}_2$ was synthesized for $x = 0.1, 0.2, 0.3, 0.5$. The samples contain large amounts of impurity phases, mainly BaMn_2P_2 , Mn_2P , and CsMnP . Exemplarily, the X-ray diffraction pattern of the sample with $x = 0.1$ is shown in Figure 5.5. Due to their very similar atomic scattering factors, cesium and barium cannot be distinguished by X-ray diffraction. However, Rietveld refinements of the data revealed that the lattice parameters are only reduced by a maximum of 0.02 % and 0.3 % for a and c , respectively, while they are reduced by 1.4 % and 8.0 % in the pure barium compound^[57]. This indicates that no or only very little barium has been incorporated into CsMn_2P_2 .

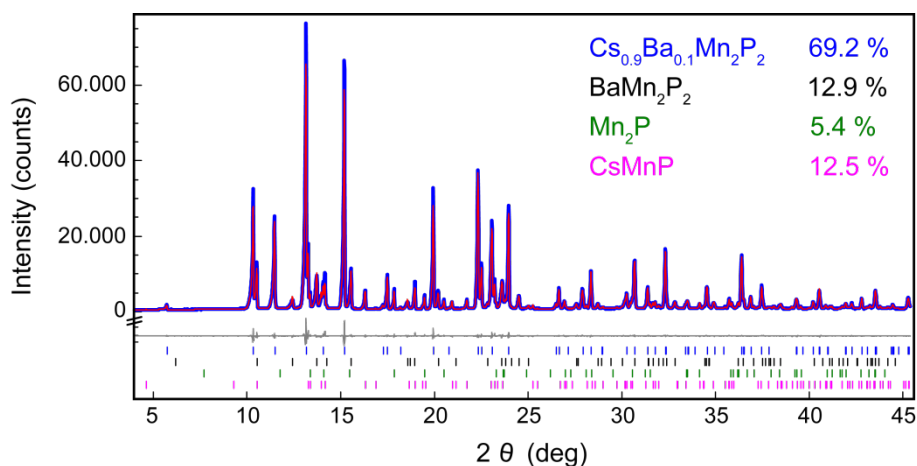


Figure 5.5: X-ray powder-diffraction pattern of $\text{Cs}_{0.9}\text{Ba}_{0.1}\text{Mn}_2\text{P}_2$ (blue) with Rietveld refinement (red).

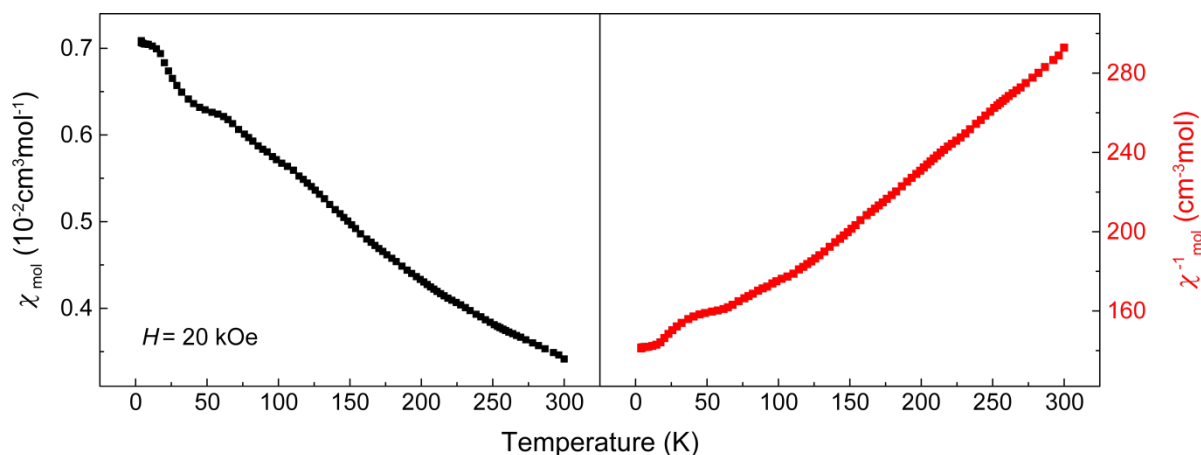


Figure 5.6: Magnetic susceptibility (left) and inverse magnetic susceptibility (right) of $\text{Cs}_{0.9}\text{Ba}_{0.1}\text{Mn}_2\text{P}_2$.

Nevertheless, the magnetic susceptibility of the nominal $\text{Cs}_{0.9}\text{Ba}_{0.1}\text{Mn}_2\text{P}_2$ sample has been measured in order to check for changes in the magnetic behavior (Figure 5.6). While it does not show the drop in the susceptibility at 11 K, which is found for CsMn_2P_2 , additional anomalies appear between 75 and 20 K, which might be ascribed to impurity phases.

5.5 O_2 - and H_2 -annealing

Both the oxygen annealing as well as the hydrogen annealing of CsMn_2P_2 lead to structural changes of the compound. The X-ray powder-diffraction data including Rietveld refinements are plotted in Figure 5.7. The corresponding crystallographic data can be found in Table 5.2. While only the O_2 -annealing led to a slight increase of the lattice parameter a ($\sim 0.08\%$), both annealing treatments resulted in a slight decrease ($\sim 0.02\%$) of the lattice parameter c . This and the slightly reduced z parameter of the phosphorus site leads to flattened MnP tetrahedra with shortened MnP distances after both treatments. The refinements of both samples indicate a small cesium deficiency of less than 1 %.

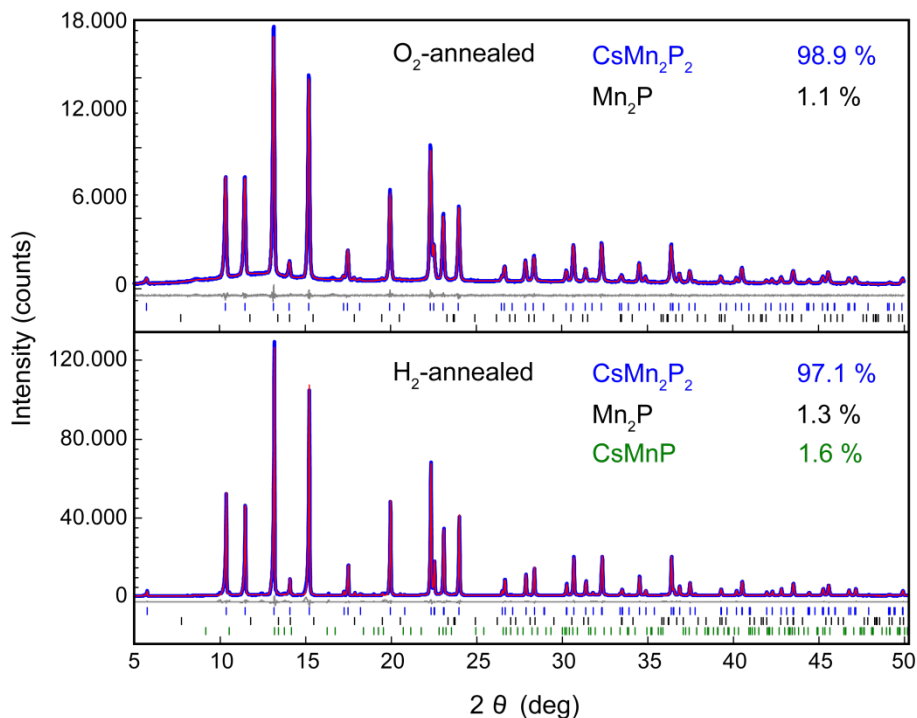


Figure 5.7: X-ray powder-diffraction patterns (blue) of an O₂- (top) and an H₂- (bottom) annealed sample of CsMn₂P₂ with Rietveld refinements (red).

Table 5.2: Crystallographic data for the O₂- and H₂- annealed sample of CsMn₂P₂.

	O ₂ -annealing	H ₂ -annealing
space group	<i>I4/mmm</i> (no. 139)	<i>I4/mmm</i> (no. 139)
molar mass (g/mol)	304.7291	304.7291
lattice parameter <i>a</i> (pm)	409.82(2)	409.46(1)
lattice parameter <i>c</i> (pm)	1420.1(1)	1420.16(2)
cell volume (nm ³)	0.23851(3)	0.23810(1)
density (g/cm ³)	4.24(1)	4.25(1)
<i>Z</i>	2	2
data points	4500	3015
reflections (all phases)	148	267
refined parameters	88	44
<i>R_p</i> , <i>wR_p</i>	0.027, 0.035	0.040, 0.073
<i>R_{bragg}</i> , χ^2	0.006, 1.136	0.009, 3.567
atomic parameters		
Cs	$2a (0, 0, 0)$	$U_{\text{iso}} = 200(2) \text{ pm}^2$
	occupancy	$U_{\text{iso}} = 173(3) \text{ pm}^2$
		0.994(2)
Mn	$4d (0, 0.5, 0.25)$	$U_{\text{iso}} = 112(3) \text{ pm}^2$
		$U_{\text{iso}} = 96(4) \text{ pm}^2$
P	$4e (0,0,z)$	$z = 0.3363(1)$
		$z = 0.3364(2)$
		$U_{\text{iso}} = 126(4) \text{ pm}^2$
		$U_{\text{iso}} = 113(5) \text{ pm}^2$

The magnetic susceptibilities of both samples with enlarged sections of the low-temperature region are shown in Figure 5.8. After oxygen annealing of the sample the drop in the susceptibility at 11 K has disappeared, while hydrogen annealing led to an additional drop at ~ 17 K. A Curie-Weiss fit revealed effective magnetic moments per formula unit of $4.03 \mu_B$ and $3.71 \mu_B$ for the O₂- and H₂-annealed sample, respectively. These values correspond to an average effective magnetic moment per manganese atom of $2.85 \mu_B$ and $2.62 \mu_B$. Compared to the initial values of $4.68 \mu_B$ per formula unit or $3.31 \mu_B$ per manganese atom, which are found for CsMn₂P₂ without further treatment, both annealing experiments have led to a decrease of the effective magnetic moment.

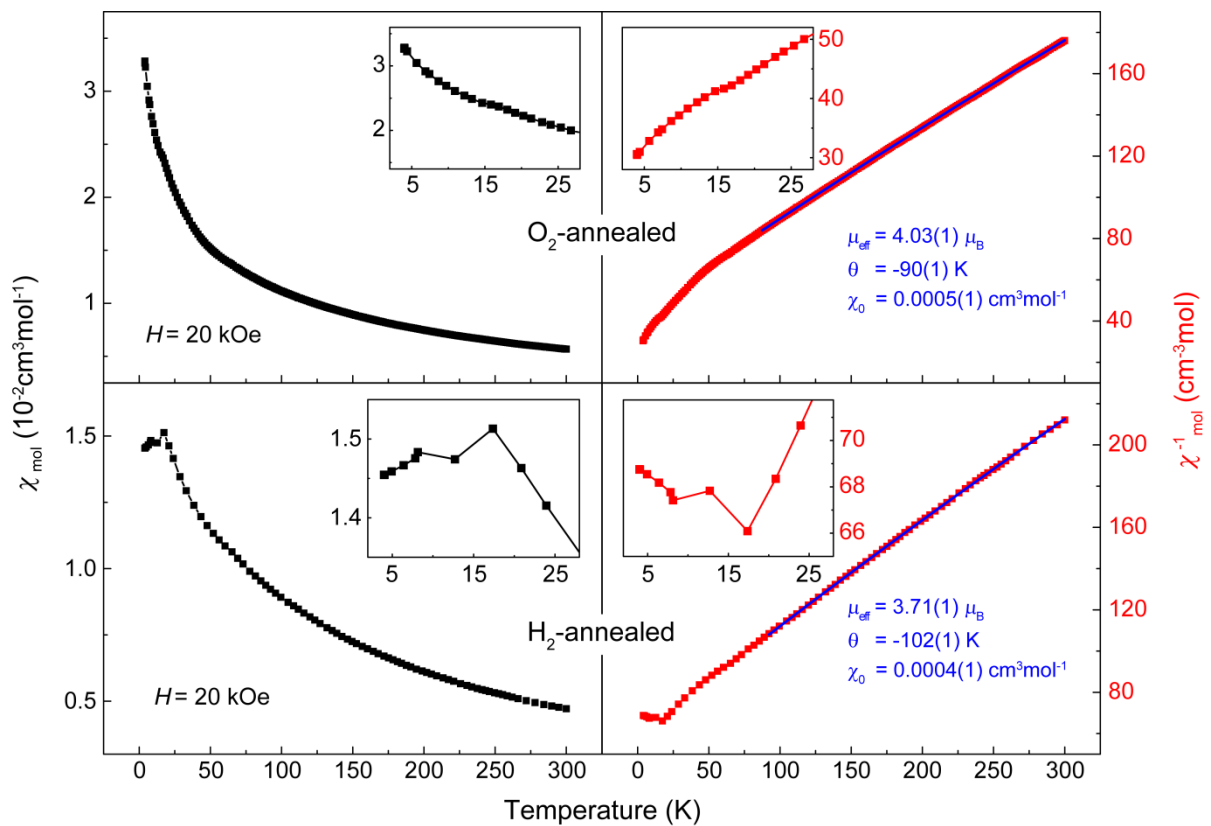


Figure 5.8: Magnetic susceptibility (left) and inverse magnetic susceptibility with Curie-Weiss fit (right) of an O₂- (top) and H₂- (bottom) annealed sample of CsMn₂P₂. Insets: Enlarged low-temperature sections.

While the original value was close to an average of 2.5 electrons ($3.35 \mu_B$) per manganese atom, oxygen annealing results in a moment close to the one expected for an average of 2 electrons ($2.85 \mu_B$) and hydrogen annealing indicates an average of 1.8 electrons ($2.62 \mu_B$) per manganese atom. Thus, both treatments have led to a reduction of the number of electrons participating in the magnetic ordering or maybe present in the system. Such an oxidation would be expected for O₂-annealing but not for the reductive H₂-annealing.

However, both methods have clearly modified the magnetic properties of CsMn₂P₂. In order to examine if this is also true for the dynamic effects further experiments are needed.

For the oxygen-annealed sample preliminary μ SR results were obtained which indicate the presence of two magnetically different phases, whereby both show the same behavior as non-treated CsMn₂P₂ but one with a weaker magnetic moment. This magnetically weaker phase constitutes ~30 % of the sample. Assuming the "original" magnetic moment of 3.31 μ_B for 70 % of the sample leads to a moment of 1.23 μ_B for the remaining 30 % of the sample. This corresponds to an average of 0.5 electrons per manganese atom. Thus, the preliminary μ SR results indicate that the O₂-annealed sample consists of a ~70 % phase with the same properties as non-treated CsMn₂P₂ and an average of 2.5 ordered electrons per manganese atom and a ~30 % phase with an average of only 0.5 ordered electrons per manganese atom.

5.6 Conclusion

The results for Cs_{1-x}Rb_xMn₂P₂ are very promising and indicate that the whole range of the solid solution is easily accessible via the chosen synthesis route in sufficient quality for studying its properties. The magnetic susceptibility is in good agreement with the obtained data for CsMn₂P₂ and RbMn₂P₂. However, the structural changes observed at low temperatures for CsMn₂P₂ are already suppressed at rubidium contents of 18 %, while the anomalies of the resistivity are still present, although slightly altered. Thus, the physical properties have effectively been modified, but probably without a full suppression of the dynamic effects. However, this might be achieved by higher rubidium levels and should be examined in the future.

In order to analyze these properties for Cs_{1-x}Ba_xMn₂P₂, an optimization of the synthesis process is required. The sample quality obtained by now does not suffice to conclusively examine the physical properties of the samples.

The annealing experiments with oxygen and hydrogen have successfully modified the magnetic properties of CsMn₂P₂ and reduced the effective magnetic moment.

However, further neutron and μ SR experiments are required in order to examine how or if the modifications have influenced the complicated dynamic effects of the magnetism in CsMn₂P₂. Additionally, substituting the manganese in CsMn₂P₂ could be a promising way to modify the magnetic properties. Hereby elements which do typically not exhibit magnetic ordering would be especially interesting.

6 $\text{Eu}_3\text{Sc}_2\text{O}_5\text{Fe}_2\text{As}_2$

Parts of this chapter are accepted for publication in *Z. Naturforsch., Part B*.

© 2015 Walter de Gruyter

F. Hummel, M. Tegel, B. Gerke, R. Pöttgen, D. Johrendt, *arXiv: 1506.02925 2015*.

6.1 Introduction

Since the discovery of superconductivity in $\text{LaO}_{1-x}\text{F}_x\text{FeAs}$ ^[5] (so-called 1111 type) many other structure types of iron-based superconductors have been discovered: apart from the three structure types, which are investigated in the present thesis (122^[19], 32522^[21], and 21311^[25]), also the so-called 111^[58,59], 11^[60], 10-3-8, 10-4-8^[61], and the 112 type^[62]. Despite the large variety of compounds reported, only few europium compounds are known. Particularly EuFe_2As_2 has been intensively studied as its properties are strongly related to those of the isostructural alkaline earth compounds. Similar to AEFe_2As_2 ($\text{AE} = \text{Ca}, \text{Sr}, \text{Ba}$), the parent compound undergoes a structural transition (at 190 K in the case of EuFe_2As_2 ^[63]) and superconductivity can be induced by suppressing the transition either by applying pressure^[64] or by different methods of doping^[65-71]. However, EuFe_2As_2 takes a special position among the 122 parent compounds of iron-based superconductors due to the magnetism of europium. In addition to the antiferromagnetic stripe-like ordering of the iron moments at 190 K, it exhibits a second magnetic transition at 19 K where the europium moments order antiferromagnetically (A type)^[63]. Although the ordering of the Eu^{2+} moments is not suppressed when superconductivity is induced, it seems to influence the superconducting properties negatively. In EuFe_2As_2 ^[72] under pressure and in $\text{Eu}_{1-x}\text{Sr}_x\text{Fe}_{2-y}\text{Co}_y\text{As}_2$ ^[73], a small but significant increase in resistivity has been observed at the ordering temperature of the europium moments.

Here, the existence of an europium compound of the 32522-type iron pnictides is reported, where the FeAs layers are widely separated by perovskite-like oxide layers. Up to now the only known iron pnictides with this structure are $\text{Sr}_3\text{Sc}_2\text{O}_5\text{Fe}_2\text{As}_2$ ^[21], $\text{Ba}_3\text{Sc}_2\text{O}_5\text{Fe}_2\text{As}_2$ ^[74], and $\text{Ca}_3\text{Al}_2\text{O}_{5-y}\text{Fe}_2\text{Pn}_2$ ($\text{Pn} = \text{As}, \text{P}$)^[22]. Unlike the 122-type compounds, none of these 32522 compounds undergoes a structural transition. Only the calcium compounds show superconductivity and by doping the strontium compound with titanium, traces of superconductivity have been observed in $\text{Sr}_3\text{Sc}_{2-x}\text{Ti}_x\text{O}_5\text{Fe}_2\text{As}_2$ ^[75].

6.2 Experimental details

A polycrystalline sample of Eu₃Sc₂O₅Fe₂As₂ was synthesized by heating a stoichiometric mixture of Eu, Sc, FeO, and As₂O₃. The reaction mixture was transferred into an alumina crucible and sealed in a silica ampoule. The sample was heated up to 1173 K for 20 h at rates of 50 K/h and 200 K/h for heating and cooling, respectively. Afterwards, the sample was homogenized, pressed into a pellet, and sintered for 60 h at 1373 K (heated at a rate of 100 K/h and cooled at 200 K/h). This sintering step was performed twice.

Temperature-dependent X-ray powder-diffraction patterns between 300 K and 10 K (10 K step size) were recorded using the Huber diffractometer with Co-K α_1 radiation. For Rietveld refinements of the data the TOPAS package^[30] was used with spherical harmonics functions to describe the preferred orientation of the crystallites. Shape anisotropy effects were described by the approach of *Le Bail* and *Jouanneaux*^[31]. Magnetic measurements were performed using both the SQUID magnetometer and the AC susceptometer. Additionally, Mössbauer experiments were conducted.

6.3 Crystal structure

Eu₃Sc₂O₅Fe₂As₂ was obtained as black polycrystalline air-stable sample. The crystal structure and the sample composition were analyzed via Rietveld refinements of the X-ray powder data at 300 K (Figure 6.1). The sample consists of 91 % Eu₃Sc₂O₅Fe₂As₂, 7 % EuFe₂As₂, 1 % Sc₂O₃, and 1 % FeO (wt%). The corresponding crystallographic data can be found in Table 6.1. Further details of the structure determination may be obtained from: Fachinformationszentrum Karlsruhe, 76344 Eggenstein-Leopoldshafen, Germany, by quoting the Registry No. CSD-429704.

Eu₃Sc₂O₅Fe₂As₂ crystallizes in the Sr₃Fe₂O₅Cu₂S₂-type structure^[20] with lattice parameters $a = 406.40(1)$ pm and $c = 2646.9(1)$ pm. It consists of tetrahedral iron-arsenide layers separated by a perovskite-like interlayer (Figure 6.1, right). Eu1 is coordinated by 8+4 oxide ions similar to perovskites like EuTiO₃^[76], where all 12 Eu-O contacts are equal. Eu2 is eightfold coordinated by four oxide- and four arsenide neighbors. Scandium is surrounded by five oxide ions which form a square pyramid. The Fe-As bonds (243.76(6) pm) and As-Fe-As angles (2x 112.9(1)°, 4x 107.8(1)°) in the FeAs_{4/4} tetrahedra are close to the values found in related compounds like Sr₃Sc₂O₅Fe₂As₂ (Fe-As bonds: 243.56(9) pm, As-Fe-As angles: 2x 113.3(1)°, 4x 107.6(1)°^[21]). However, the tetrahedra are strongly compressed as compared to those in EuFe₂As₂ (Fe-As bonds: 256.45(5) pm, As-Fe-As angles: 2x 99.4(1)°, 4x 114.7(1)°^[77]) which becomes superconducting upon doping.

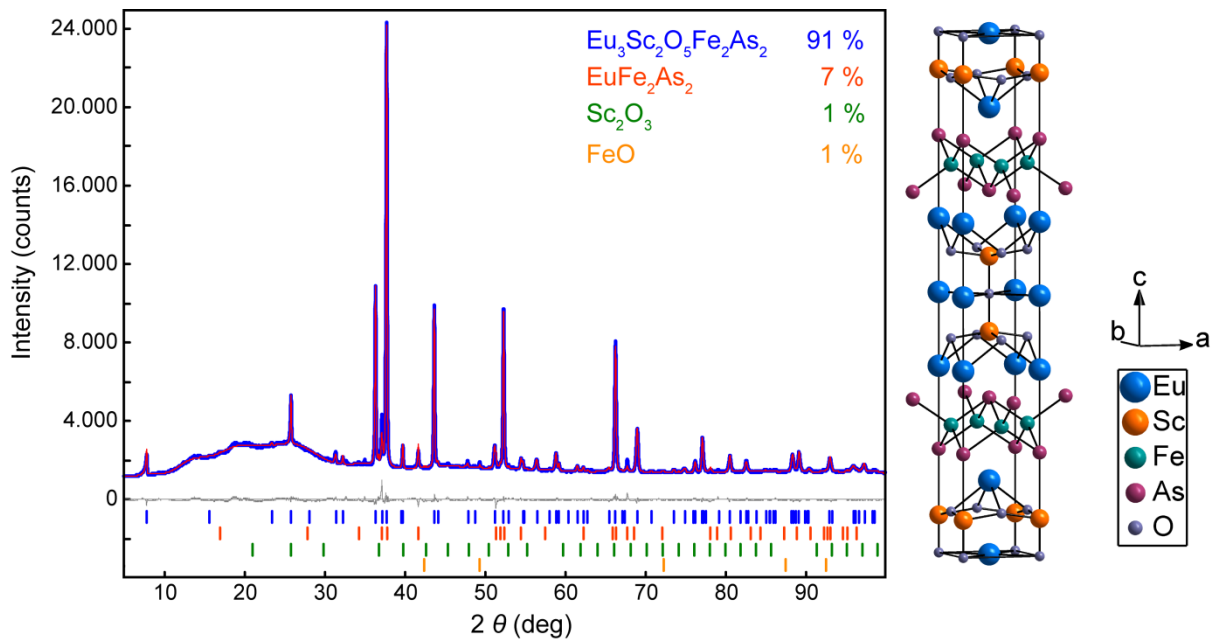


Figure 6.1: X-ray powder-diffraction pattern at 300 K (blue), Rietveld refinement (red) and structure (right) of $\text{Eu}_3\text{Sc}_2\text{O}_5\text{Fe}_2\text{As}_2$.

A selection of X-ray powder-diffraction patterns at different temperatures is shown in Figure 6.2. No signs of a structural transition are observed down to 10 K. The reflections at 15, 25, and 29 $^{\circ}2\theta$ appearing below 250 K are due to the sample environment and the reflection at about 42 $^{\circ}2\theta$ belongs to the impurity phase EuFe_2As_2 . This phase undergoes a structural transition below 190 K (tetragonal $I4/mmm$ to orthorhombic $Fmmm$ ^[78]).

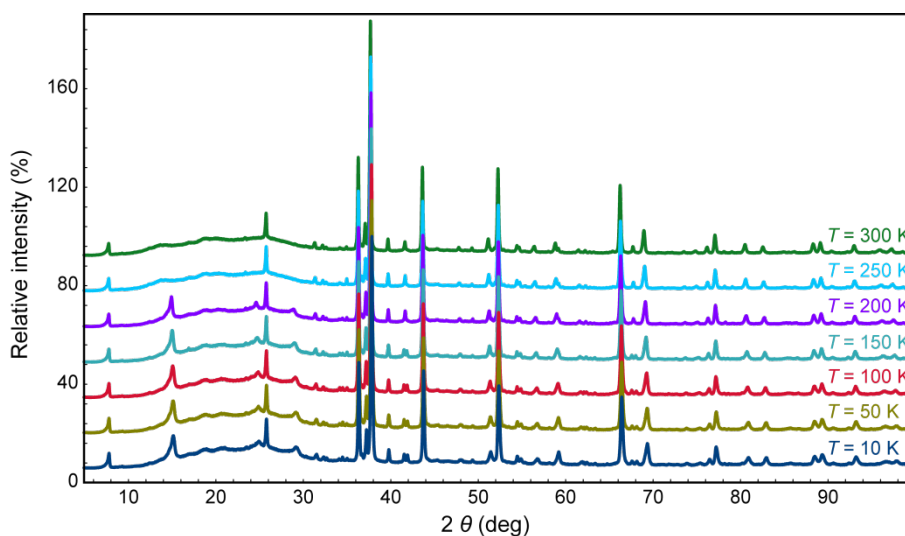


Figure 6.2: X-ray powder-diffraction patterns of $\text{Eu}_3\text{Sc}_2\text{O}_5\text{Fe}_2\text{As}_2$ at different temperatures.

Table 6.1: Crystallographic data for $\text{Eu}_3\text{Sc}_2\text{O}_5\text{Fe}_2\text{As}_2$ at 10 and 300 K.

$\text{Eu}_3\text{Sc}_2\text{O}_5\text{Fe}_2\text{As}_2$			
	10	300	
temperature (K)	10	300	
space group	$I4/mmm$ (no. 139)	$I4/mmm$ (no. 139)	
molar mass (g/mol)	887.334	887.334	
lattice parameter a (pm)	405.69(1)	406.40(1)	
lattice parameter c (pm)	2630.11(2)	2646.9(1)	
cell volume (nm ³)	0.43288(1)	0.43717(2)	
density (g/cm ³)	6.81(1)	6.74(1)	
Z	2	2	
data points	19001	19001	
reflections (all phases)	175	161	
refined parameters	59	88	
R_p, wR_p	0.023, 0.033	0.017, 0.025	
R_{bragg}, χ^2	0.012, 1.436	0.010, 1.094	
atomic parameters			
Eu1	$2b$ (0, 0, 0.5)	$U_{\text{iso}} = 101(8) \text{ pm}^2$	$U_{\text{iso}} = 186(6) \text{ pm}^2$
Eu2	$4e$ (0, 0, z)	$z = 0.3574(1)$ $U_{\text{iso}} = 23(5) \text{ pm}^2$	$z = 0.3583(1)$ $U_{\text{iso}} = 62(5) \text{ pm}^2$
Sc	$4e$ (0, 0, z)	$z = 0.0721(1)$ $U_{\text{iso}} = 38(9) \text{ pm}^2$	$z = 0.0722(1)$ $U_{\text{iso}} = 58(7) \text{ pm}^2$
O1	$8g$ (0, 0.5, z)	$z = 0.0825(2)$ $U_{\text{iso}} = 230(20) \text{ pm}^2$	$z = 0.0838(2)$ $U_{\text{iso}} = 290(10) \text{ pm}^2$
O2	$2a$ (0, 0, 0)	$U_{\text{iso}} = U_{\text{iso}}(\text{O1})$	$U_{\text{iso}} = U_{\text{iso}}(\text{O1})$
Fe	$4d$ (0, 0.5, 0.25)	$U_{\text{iso}} = 38(9) \text{ pm}^2$	$U_{\text{iso}} = 56(8) \text{ pm}^2$
As	$4e$ (0, 0, z)	$z = 0.1988(1)$ $U_{\text{iso}} = 183(9) \text{ pm}^2$	$z = 0.1991(1)$ $U_{\text{iso}} = 253(6) \text{ pm}^2$

The course of the lattice parameters, the Fe-As distance d , and the tetrahedral angle α as obtained by Rietveld refinements of the low-temperature data is shown in Figure 6.3. The crystallographic data of $\text{Eu}_3\text{Sc}_2\text{O}_5\text{Fe}_2\text{As}_2$ at 10 K can be found in Table 6.1. While the lattice parameter a is contracted by only 0.2 % upon cooling, c decreases by 0.6 %. The course of both lattice parameters as a function of temperature does not imply any anomaly which would indicate a structural transition. The Fe-As distance d and the tetrahedral angle α do not change significantly upon cooling.

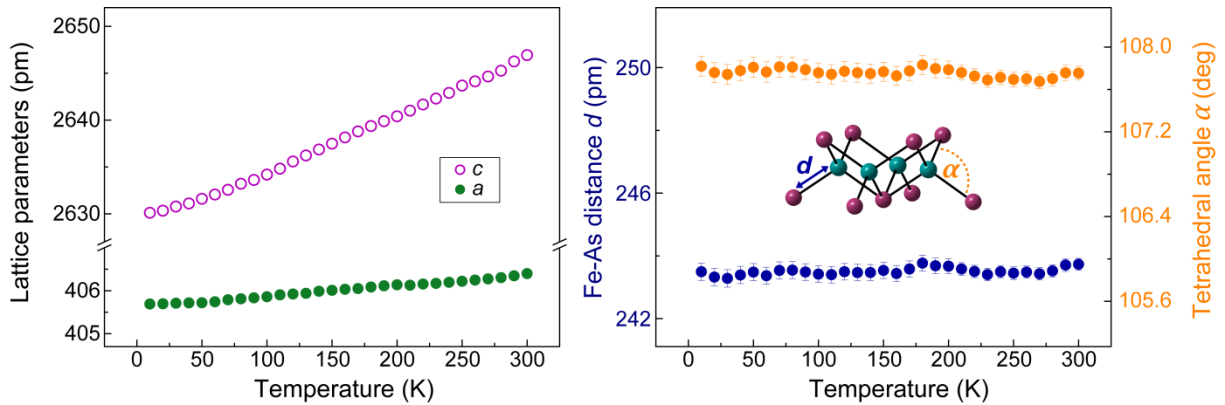


Figure 6.3: Refined lattice parameters (left), Fe-As distance d (right, blue), and tetrahedral angle α (right, orange) of $\text{Eu}_3\text{Sc}_2\text{O}_5\text{Fe}_2\text{As}_2$ as a function of temperature.

6.4 Magnetic properties

Magnetic susceptibility measurements show Curie-Weiss behavior between 5 and 300 K and a drop in the susceptibility below 5 K (Figure 6.4, left). A Curie-Weiss fit revealed an effective magnetic moment of $\mu_{\text{eff}} = 13.49(1) \mu_{\text{B}}$ per formula unit, equivalent to $7.79 \mu_{\text{B}}$ per europium atom. This is close to the theoretically expected value of $7.94 \mu_{\text{B}}$ per Eu^{2+} [79]. The negative Weiss constant $\theta = -9.5(3)$ K together with the drop in $\chi(T)$ suggests antiferromagnetic ordering at 5 K. The magnetization isotherms at 300 and 100 K increase linearly with the applied field, while the isotherm at 1.8 K can be fitted with a Brillouin function (Figure 6.4, right).

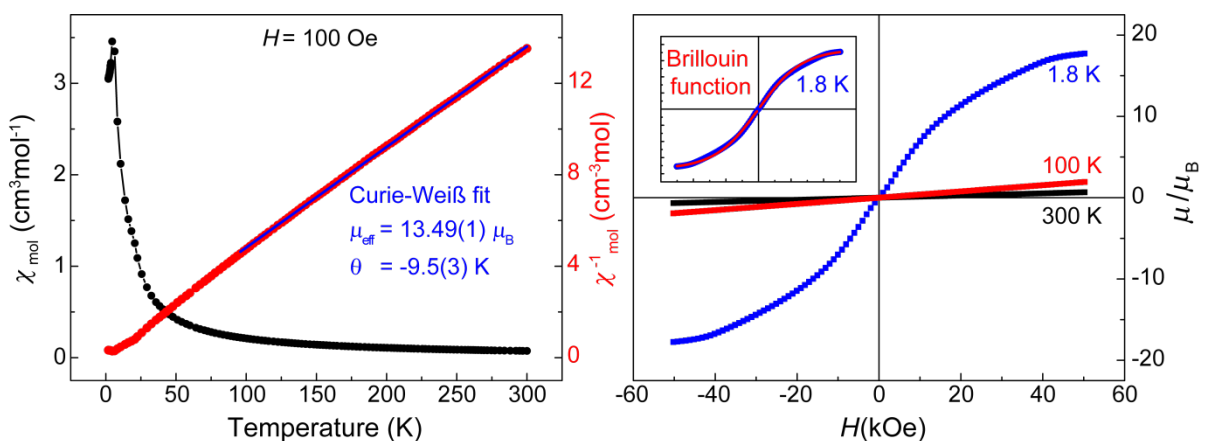


Figure 6.4: SQUID data of $\text{Eu}_3\text{Sc}_2\text{O}_5\text{Fe}_2\text{As}_2$. Left: Magnetic susceptibility (black) and inverse magnetic susceptibility (red) measured at 100 Oe with Curie-Weiss fit (blue). Right: Magnetization isotherms at 300 (black), 100 (red), and 1.8 K (blue). Inset: Brillouin function fitted to the isotherm at 1.8 K.

Figure 6.5 (left) shows the obtained ^{151}Eu Mössbauer spectra of $\text{Eu}_3\text{Sc}_2\text{O}_5\text{Fe}_2\text{As}_2$ at 78 and 4.8 K. The parameters of the transmission integral fits are compiled in Table 6.2. In accordance with the determined crystal structure, the ^{151}Eu signal could be well reproduced by a superposition of two resonances (light and dark green in Figure 6.5) with isomer shifts of $-13.26(3)$ and $-10.84(2)$ mm s^{-1} indicating Eu^{2+} . The areas of both contributions were kept fixed with the ideal values derived from the multiplicity of the atomic Eu1 and Eu2 sites. With respect to its nearly ideal cuboctahedral coordination by 8+4 oxygen atoms, Eu1 was assumed to be the nucleus of less electron density (more ionic) compared to Eu2 and therefore the origin of the resonance at $-13.26(3)$ mm s^{-1} . The isomer shifts of ionic Eu1 compare well with the values of the perovskites EuTiO_3 (-13.5 mm s^{-1}) and EuZrO_3 (-14.1 mm s^{-1})^[80,81] as well as for several borate glasses containing divalent europium^[82]. The Eu2 signal is close to the value observed for EuFe_2As_2 (-11.3 mm s^{-1})^[83].

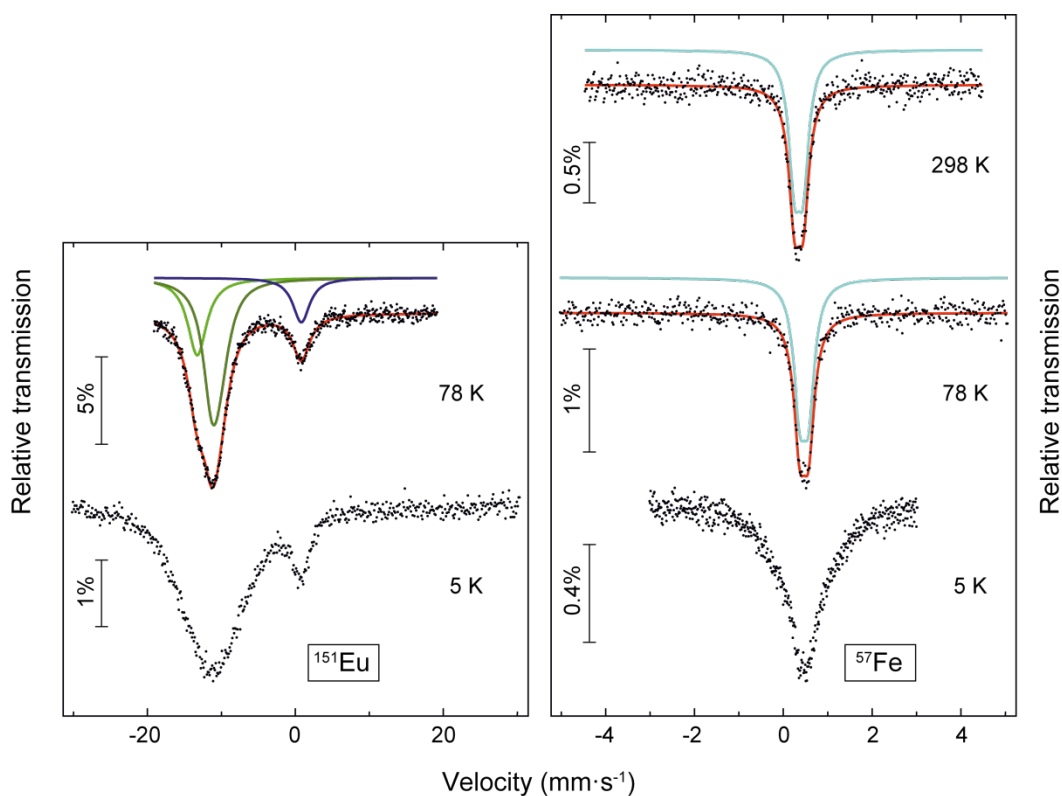


Figure 6.5: Experimental and simulated ^{151}Eu (left) and ^{57}Fe (right) Mössbauer spectra of $\text{Eu}_3\text{Sc}_2\text{O}_5\text{Fe}_2\text{As}_2$ at 298 K (top), 78 K (middle), and 4.8 K (bottom).

Table 6.2: Fitting parameters of ¹⁵¹Eu and ⁵⁷Fe Mössbauer spectroscopic measurements of Eu₃Sc₂O₅Fe₂As₂ at ambient temperature and at 78 K. δ = isomer shift, ΔE_Q = electric quadrupole splitting, Γ = experimental line width. Parameters marked with an asterisk were kept fixed during the fitting procedure.

	T (K)	δ (mm s ⁻¹)	ΔE_Q (mm s ⁻¹)	Γ (mm s ⁻¹)	ratio (%)
¹⁵¹ Eu	78	-13.26(3)	0*	3.11(6)	28*
		-10.84(2)	-3.3(2)	2.8(1)	57*
		0.80(4)	0*	2.8(1)	15(1)
⁵⁷ Fe	298	0.35(1)	0.20(1)	0.31(1)	100
	78	0.47(1)	0.20(1)	0.32(1)	100

Furthermore, a quadrupole splitting for Eu1 was excluded because of the symmetric arrangement around the nucleus (almost cubic site symmetry). A small resonance at an isomer shift of 0.80(4) mm s⁻¹ (dark blue in Figure 6.5) indicates trivalent europium possibly due to extrinsic Eu³⁺ because of surface oxidation.

The ⁵⁷Fe Mössbauer spectra of Eu₃Sc₂O₅Fe₂As₂, recorded at 298, 78, and 4.8 K, are presented in Figure 6.5 (right). At ambient temperature and at 78 K the spectrum shows a single signal which can be attributed to an isomer shift of 0.35(1) mm s⁻¹ at 298 K and 0.47(1) mm s⁻¹ at 78 K (intermetallic iron^[78,84,85]). Additionally, a small interaction is observed between quadrupole and electric field gradient, resulting in a splitting of 0.20(1) mm s⁻¹.

With regard to the magnetic ordering indicated by susceptibility data, ¹⁵¹Eu and ⁵⁷Fe Mössbauer spectroscopic measurements were repeated at 4.8 K (Figure 6.5, bottom), quite close to the observed drop in the magnetic susceptibility data. Both the ¹⁵¹Eu and ⁵⁷Fe spectra clearly show broadened resonances confirming a cooperative magnetic phenomenon. A fitting of the obtained spectra in order to determine the magnitude of the hyperfine field was difficult as there are too many parameters that cannot be fitted confidentially and the experimental setup is at its limit at 4.8 K. The temperature varies in the range of about ± 0.3 K, which has an influence on the exact splitting, especially for measurements close to the ordering temperature, leading to too many correlations within the refinement procedures.

6.5 Substitution experiments on Eu₃Sc₂O₅Fe₂As₂

As europium and alkaline earth compounds show a strong similarity in the 122-type iron pnictides, one could expect that Eu₃Sc₂O₅Fe₂As₂ might become superconducting upon doping just like the isostructural strontium compound Sr₃Sc_{2-x}Ti_xO₅Fe₂As₂ where traces of

superconductivity were reported^[75]. Therefore, different substitution experiments on $\text{Eu}_3\text{Sc}_2\text{O}_5\text{Fe}_2\text{As}_2$ were performed. As the 32522 structure contains five different elements on altogether seven crystallographic sites, there are numerous possibilities for such substitutions. Here, substitutions were attempted on both Eu sites, the Sc, and the As site, whereby hole, electron, or isostructural doping was intended. For reasons of simplicity, the compounds are labeled as $\text{Eu}_{3-x}\text{A}_x\text{Sc}_{2-y}\text{B}_y\text{O}_5\text{Fe}_2\text{As}_{2-z}\text{C}_z$ with three substitution positions A, B, and C. An overview of the tested substitutions presented here is given in Table 6.3.

Table 6.3: Overview of the substitution experiments on $\text{Eu}_3\text{Sc}_2\text{O}_5\text{Fe}_2\text{As}_2$.

$\text{Eu}_{3-x}\text{A}_x\text{Sc}_{2-y}\text{B}_y\text{O}_5\text{Fe}_2\text{As}_{2-z}\text{C}_z$					
substituting element	substituted position	degree of substitution	substituting element	substituted position	degree of substitution
Ca	A	$x = 0.1$	Mg	B	$y = 0.3$
		$x = 0.2$			$y = 0.5$
Ti	B	$y = 0.5$	Ti/Mg	B	$y = 1.0$
		$y = 1.0$			$y_{\text{Ti}} = 1.5$
		$y = 2.0$			$y_{\text{Mg}} = 0.5$
V	B	$y = 0.2$	Al	B	$y = 0.5$
		$y = 0.5$	P	C	$z = 1.0$
		$y = 2.0$			$z = 2.0$

The compounds were synthesized according to the synthesis described in Chapter 6.2. Only the sintering temperatures were varied in some cases. As impurity phases different amounts of various oxides were obtained. In most samples, the desired 32522 compound constitutes the main phase, while in some only small amounts of this phase were detected. Figure 6.6 exemplarily shows the X-ray powder-diffraction patterns of two samples with the nominal compositions $\text{Eu}_3\text{Sc}_2\text{O}_5\text{Fe}_2\text{AsP}$ (top) and $\text{Eu}_{2.9}\text{Ca}_{0.1}\text{Sc}_2\text{O}_5\text{Fe}_2\text{As}_2$ (bottom) including their Rietveld refinements. These revealed a refined composition of $\text{Eu}_3\text{Sc}_2\text{O}_5\text{Fe}_2\text{As}_{1.2}\text{P}_{0.8}$ and $\text{Eu}_{2.7}\text{Ca}_{0.3}\text{Sc}_2\text{O}_5\text{Fe}_2\text{As}_2$, respectively. Hereby, calcium is mainly found on the second Eu site (4e). Unfortunately, a reasonable refinement of the composition was not possible for all samples, therefore the actual degree of substitution in some of them might differ strongly from the nominal composition. Nevertheless, for the purpose intended here, *i.e.* checking for signs of superconductivity, a more detailed analysis of the sample composition is not essential.

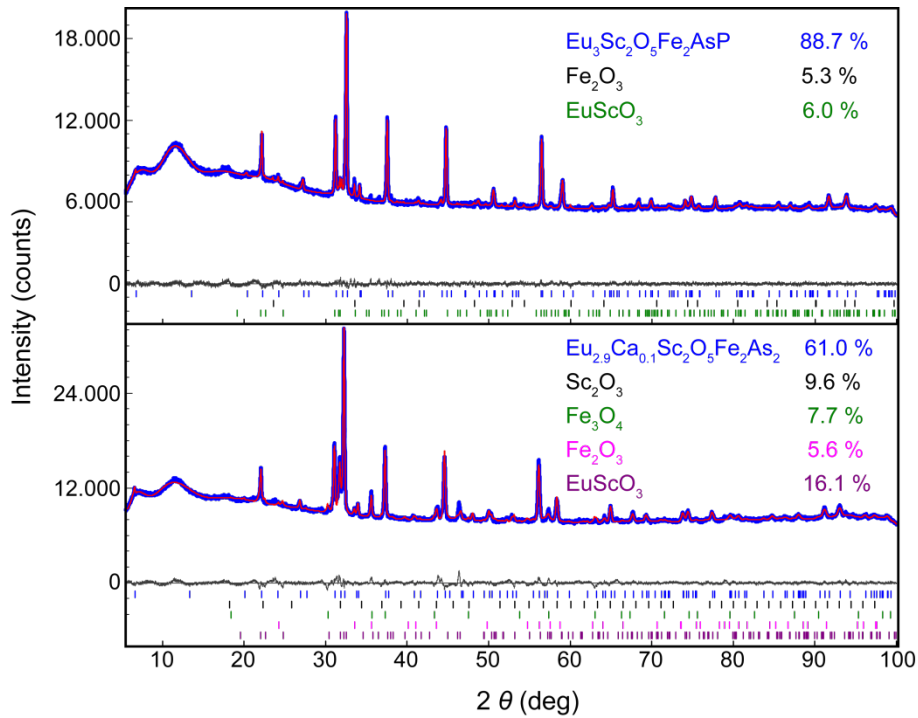


Figure 6.6: X-ray powder-diffraction pattern (blue) of $\text{Eu}_3\text{Sc}_2\text{O}_5\text{Fe}_2\text{AsP}$ (top) and $\text{Eu}_{2.9}\text{Ca}_{0.1}\text{Sc}_2\text{O}_5\text{Fe}_2\text{As}_2$ (bottom) with Rietveld refinement (red).

In order to check for superconductivity in all samples, magnetic measurements were performed. The magnetic susceptibilities of all samples with the 32522 compound as main phase are plotted in Figure 6.7. The antiferromagnetic transition of $\text{Eu}_3\text{Sc}_2\text{O}_5\text{Fe}_2\text{As}_2$ at $T_N = 5$ K is in some samples shifted towards slightly higher temperatures (6 or 7 K) and in most samples a second transition is found at 20 K. The biggest change is observed upon substitution of As with P. Here the original antiferromagnetic transition is completely suppressed at $z = 2.0$ and a new transition is found at 27 K. At higher temperatures, all samples exhibit Curie-Weiss behavior. The origin of the observed transitions is unclear and they could also be due to impurity phases. However, no superconductivity or traces thereof were detected. This also applies to the remaining samples with only small amounts of the 32522 phase (not shown).

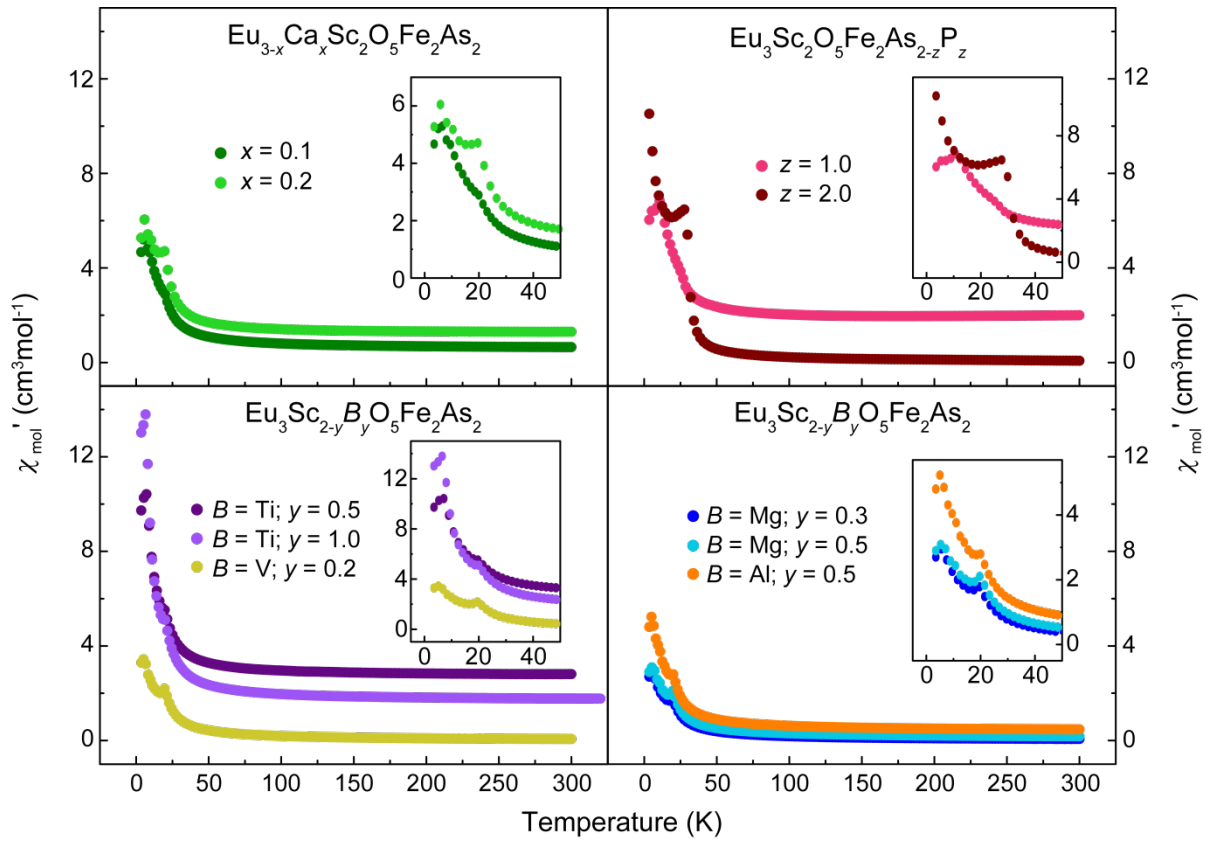


Figure 6.7: Magnetic susceptibility measurements of $\text{Eu}_{3-x}\text{A}_x\text{Sc}_{2-y}\text{B}_y\text{O}_5\text{Fe}_2\text{As}_{2-z}\text{C}_z$. Samples with substitution on position A (top, left), B (bottom), and C (top, right).

6.6 Conclusion

$\text{Eu}_3\text{Sc}_2\text{O}_5\text{Fe}_2\text{As}_2$ is a new member of the 32522-type iron pnictides with the $\text{Sr}_3\text{Fe}_2\text{O}_5\text{Cu}_2\text{S}_2$ -type structure. Similar to the already known members of this group, no signs for a structural phase transition down to 10 K were found. Magnetic measurements revealed an effective magnetic moment of $7.79 \mu_B$ per europium atom, which is in good agreement with the theoretical value of $7.94 \mu_B$ for Eu^{2+} . Additionally, indications of an antiferromagnetic ordering at $T_N = 5$ K were found. ^{151}Eu and ^{57}Fe Mössbauer spectroscopic experiments confirm the magnetic data by showing resonances for Eu^{2+} and intermetallic iron. Low-temperature measurements show a beginning magnetic ordering. As traces of superconductivity were reported for $\text{Sr}_3\text{Sc}_{2-x}\text{Ti}_x\text{O}_5\text{Fe}_2\text{As}_2$, one could expect similar results for the isostructural europium compound. However, substitution experiments on $\text{Eu}_3\text{Sc}_2\text{O}_5\text{Fe}_2\text{As}_2$ revealed no signs of superconductivity up to now. Hereby, three different substitution positions were tested. Europium was substituted by calcium, scandium by titanium, vanadium, magnesium, and aluminum, and arsenic by phosphorus.

7 The effects of chemical pressure in the solid solution $\text{Sr}_2\text{ScO}_3\text{FeAs}_{1-x}\text{P}_x$

7.1 Introduction

Superconductivity in iron-based superconductors can often be induced by applying physical or chemical pressure. Additionally, if a system is already superconducting both types of pressure are useful to tune its superconducting properties. Hereby, it depends on the symmetry of the iron-pnictide layer how a system responds to the pressure applied, as the symmetry of the $\text{FePn}_{4/4}$ tetrahedra has a big influence on the critical temperature of a superconducting system. The tetrahedral angle or the so-called pnictogen height h_{Pn} (the distance of the pnictogen atom from the Fe plane) are often chosen as parameters for characterizing the tetrahedral symmetry^[86,87]. Consequently, a system's response to pressure depends on how these structural parameters are altered by it.

For BaFe_2As_2 the maximum T_c under physical pressure ($T_{c,\text{max}} = 31$ K at $p = 5.5$ GPa) is obtained when the tetrahedral angle is close to the ideal tetrahedral value of 109.5° ^[88]. Chemical pressure can be applied to BaFe_2As_2 by partially substituting arsenic by smaller phosphorus atoms. This isoelectronic substitution leads to the emergence of superconductivity with $T_{c,\text{max}} = 30$ K for a phosphorus content of 32 %^[89]. Unlike what was initially expected, the decisive criterion for the superconducting properties in this chemically compressed system isn't the cell volume but the Fe-Pn distance^[90]. This distance is closely related to the pnictogen height h_{Pn} and constitutes a more comprehensible parameter from a crystal chemical point of view.

In 2009 $\text{Sr}_2\text{ScO}_3\text{FeP}$ was discovered as the first representative of a new structure type of iron-based superconductors: the 21311 type^[25]. Its structure is composed of the typical $(\text{FeP}_{4/4})^-$ tetrahedral layers separated by perovskite-like layers of $(\text{Sr}_2\text{ScO}_3)^+$ with a large Fe-Fe interlayer distance of 1554 pm. $\text{Sr}_2\text{ScO}_3\text{FeP}$ is superconducting with $T_c = 17$ K. This critical temperature is exceptionally high for an iron-phosphide system, which is why a lot of attention was drawn towards $\text{Sr}_2\text{ScO}_3\text{FeP}$. However, the tetrahedral symmetry is not ideal with a small fourfold tetrahedral angle of 105.2° and a short Fe-P distance of 233.8 pm. With these structural features, applying pressure leads to a decreasing T_c as the fourfold tetrahedral angle and the Fe-P distance are only reduced further, away from the ideal values^[91].

Shortly after $\text{Sr}_2\text{ScO}_3\text{FeP}$, the isostructural arsenic compound $\text{Sr}_2\text{ScO}_3\text{FeAs}$ was reported^[92]. Due to the larger arsenic atoms its cell volume is bigger than the one of the phosphide compound with an enlarged Fe-Fe interlayer distance of 1581 pm. The symmetry of the FeAs layer is closer to ideal values with a fourfold tetrahedral angle of 107.9° and an Fe-As distance of 243.4 pm. The compound exhibits a Curie-Weiss-like behavior and no signs of superconductivity were detected. By applying pressure on $\text{Sr}_2\text{ScO}_3\text{FeAs}$ the structure should approach the structure of the phosphide compound, whereby the Fe-As distance would be reduced and superconductivity might be induced. However, so far, no pressure experiments on $\text{Sr}_2\text{ScO}_3\text{FeAs}$ were reported.

In this chapter, the effects of chemical pressure through isoelectronic substitution of arsenic by smaller phosphorus atoms in the solid solution $\text{Sr}_2\text{ScO}_3\text{FeAs}_{1-x}\text{P}_x$ with $x = 0 - 1$ are studied. Particularly, it is examined how this chemical pressure affects the FePn tetrahedral structure and the magnetic properties of the system.

7.2 Experimental details

Polycrystalline samples of $\text{Sr}_2\text{ScO}_3\text{FeAs}_{1-x}\text{P}_x$ with $x = 0 - 1$ were synthesized by heating stoichiometric mixtures of Sr, Sc_2O_3 , Fe_2O_3 , As, and P. The reaction mixtures were transferred into alumina crucibles, sealed in silica ampoules, and heated up to 1373 K for 40 h at rates of 60 K/h and 200 K/h for heating and cooling, respectively. Hereby, all samples containing arsenic were heated at a rate of only 25 K/h between 573 K and 873 K. Then, the samples were homogenized, pressed into pellets, and sintered for 40 h at 1373 K with heating rates of 100 K/h and cooling rates of 200 K/h. This sintering step was performed twice.

X-ray powder-diffraction patterns were recorded using both Huber diffractometers with $\text{Cu-K}\alpha_1$ and $\text{Co-K}\alpha_1$ radiation. For Rietveld refinements of the data the TOPAS package^[30] was used with March Dollase functions to describe the preferred orientation of the crystallites. Energy dispersive X-ray (EDX) experiments were performed on the Jeol JSM-6500 FE SEM and magnetic measurements on the AC susceptometer.

7.3 Sample composition

$\text{Sr}_2\text{ScO}_3\text{FeAs}_{1-x}\text{P}_x$ samples with nominal phosphorus contents between 0 and 100 % were obtained with the desired 21311 compound as main phase. The actual phosphorus content within this phase was determined via EDX measurements. As can be seen in Figure 7.1, the experimentally determined P content is very close to the nominal one for all samples except one, whereby this maximum deviation is found for $x_{\text{nom}} = 0.70$ and $x = 0.52$.

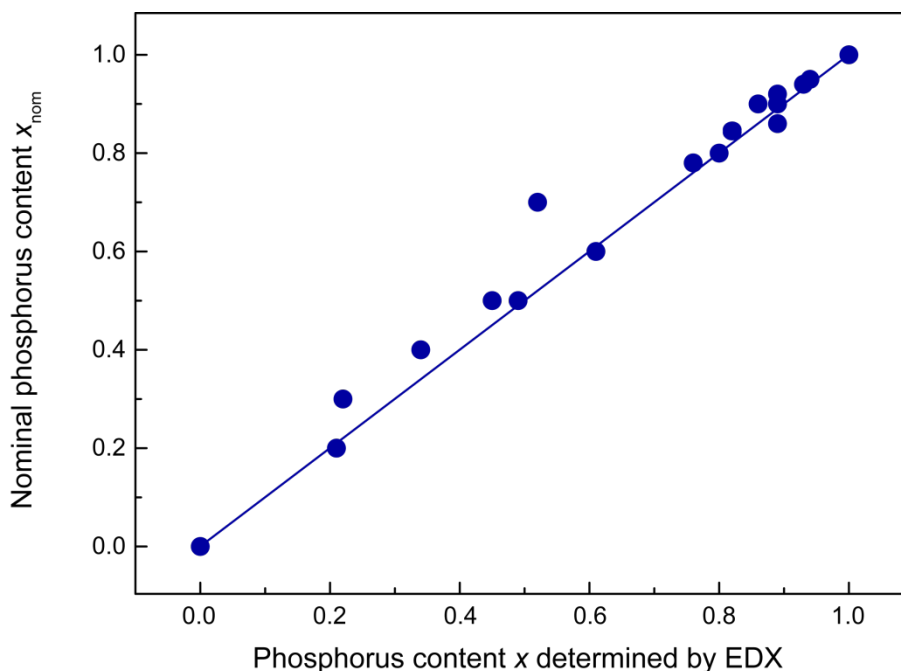


Figure 7.1: Relation between the nominal phosphorus content in $\text{Sr}_2\text{ScO}_3\text{FeAs}_{1-x}\text{P}_x$ and the one determined by EDX.

As impurity phases SrFe_2P_2 , SrSc_2O_4 , Sr_2As , and SrO occurred with differing amounts. In two samples an additional impurity phase was detected which could not be identified. The composition of all samples is listed in Table 7.1. The amount of impurity phases is increased with increasing phosphorus content. While SrFe_2P_2 is nearly always formed in samples with $x > 0.61$, the analogous As compound is not found as impurity phase for lower P contents.

Table 7.1: Composition of the $\text{Sr}_2\text{ScO}_3\text{FeAs}_{1-x}\text{P}_x$ samples according to Rietveld refinements.

x	$\text{Sr}_2\text{ScO}_3\text{FeAs}_{1-x}\text{P}_x$	amount (wt%) of				SrO	unidentified phase
		SrFe_2P_2	SrSc_2O_4	Sr_2As			
0	100	-	-	-	-	-	
0.21	99	-	-	-	1	-	
0.22	95.7	-	-	2.3	2	-	
0.34	94.1	-	2.8	1.8	1.3	-	
0.45	93	-	4	1.5	1.5	-	
0.49	100	-	-	-	-	-	
0.52	86.6	-	8.4	5	-	-	
0.61	>66	1	23	-	-	< 10	
0.76	94.4	3.3	2.3	-	-	-	
0.8	84.8	5.8	7.4	2	-	-	
0.82	89.6	7.2	3.2	-	-	-	
0.82	82.5	11.2	-	-	6.3	-	
0.86	84.9	9.9	-	-	5.2	-	
0.89	58.4	17.4	13.2	2.9	8.1	-	
0.89	92.7	7.3	-	-	-	-	
0.89	89.6	6.6	2.8	-	1	-	
0.93	>74	-	16	-	-	<10	
0.94	76.1	12.1	5.9	-	5.9	-	
1	92.6	7.4	-	-	-	-	
1	86.2	9.5	-	-	4.3	-	

7.4 Crystal structure

The structural properties of $\text{Sr}_2\text{ScO}_3\text{FeAs}_{1-x}\text{P}_x$ are studied based on the crystallographic data obtained from Rietveld refinements of the X-ray data. Exemplarily, the X-ray diffraction patterns of samples with $x = 0, 0.49$, and 1 are displayed in Figure 7.2 and the corresponding crystallographic data can be found in Table 7.2.

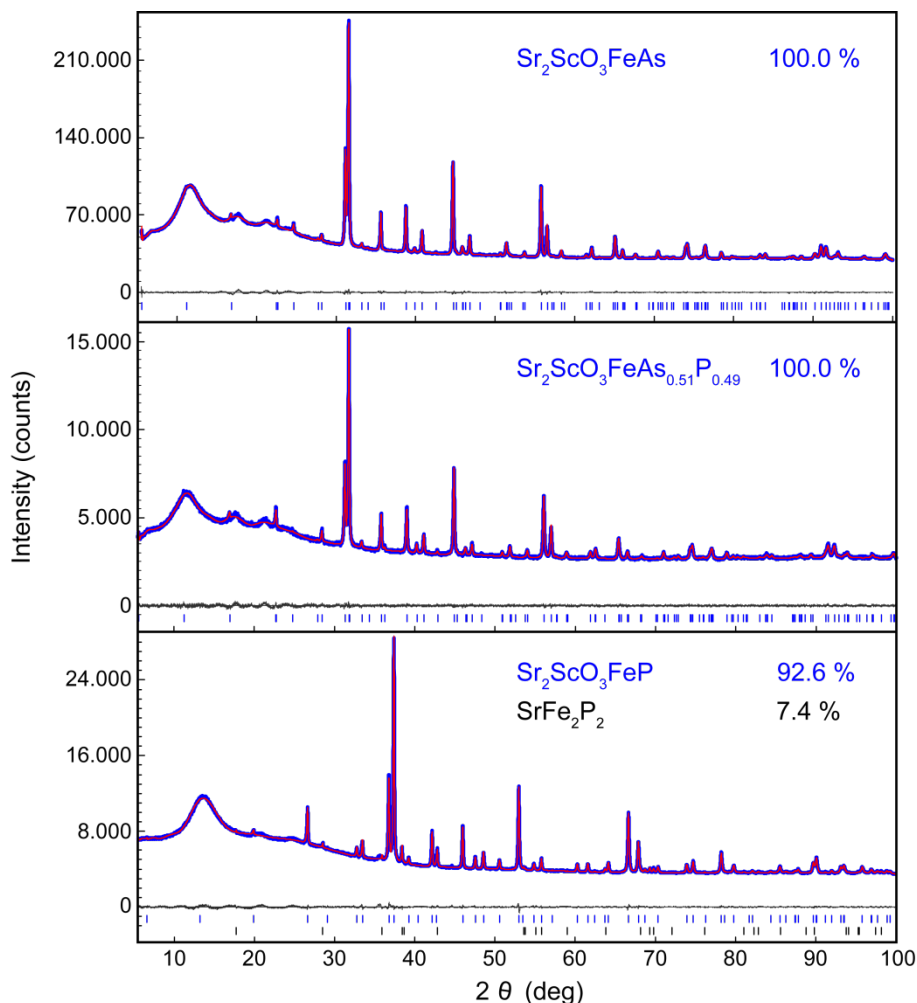


Figure 7.2: X-ray powder-diffraction pattern (blue) of $\text{Sr}_2\text{ScO}_3\text{FeAs}_{1-x}\text{P}_x$ with $x = 0$ (top, $\text{Cu-K}\alpha_1$ radiation), 0.49 (middle, $\text{Cu-K}\alpha_1$), and 1 (bottom, $\text{Co-K}\alpha_1$) with Rietveld refinements (red).

Although the structural parameters for $\text{Sr}_2\text{ScO}_3\text{FeAs}$ and $\text{Sr}_2\text{ScO}_3\text{FeP}$ differ slightly from the ones given in literature^[25,92], the same clear trend is found here: the arsenic compound exhibits the larger unit cell with a longer Fe-Fe interlayer distance. Hereby, the $\text{FeAs}_{4/4}$ tetrahedra are closer to the symmetry of an ideal tetrahedron than the $\text{FeP}_{4/4}$ tetrahedra. In order to analyze the structural changes within the solid solution $\text{Sr}_2\text{ScO}_3\text{FeAs}_{1-x}\text{P}_x$ in more detail, the lattice parameters and the cell volume are plotted in Figure 7.3 as function of the phosphorus content.

Table 7.2: Crystallographic data for $\text{Sr}_2\text{ScO}_3\text{FeAs}_{1-x}\text{P}_x$ with $x = 0, 0.49, \text{ and } 1$.

		$\text{Sr}_2\text{ScO}_3\text{FeAs}_{1-x}\text{P}_x$		
		$P4/nmm$ (no. 129, o1)		
space group				
phosphorus content x	0	0.49	1	
wavelength (nm)	0.15406	0.15406	0.17890	
molar mass (g/mol)	398.961	377.426	355.013	
lattice parameter a (pm)	404.79(1)	403.14(1)	401.01(1)	
lattice parameter c (pm)	1579.86(1)	1565.93(2)	1552.82(1)	
cell volume (nm ³)	0.25886(1)	0.25449(1)	0.24971(1)	
density (g/cm ³)	5.20(1)	4.96(1)	4.72(1)	
Z	2	2	2	
data points	18901	18901	18901	
reflections (all phases)	114	111	108	
refined parameters	87	88	73	
R_P, wR_P	0.007, 0.009	0.009, 0.012	0.008, 0.011	
R_{bragg}, χ^2	0.004, 1.942	0.002, 0.681	0.003, 0.762	
atomic parameters				
Sr1	$2c (0, 0.5, z)$	$z = 0.8098(1)$ $U_{\text{iso}} = 93(3) \text{ pm}^2$	$z = 0.8163(1)$ $U_{\text{iso}} = 38(4) \text{ pm}^2$	$z = 0.8188(1)$ $U_{\text{iso}} = 65(3) \text{ pm}^2$
Sr2	$2c (0, 0.5, z)$	$z = 0.5820(1)$ $U_{\text{iso}} = U_{\text{iso}}(\text{Sr1})$	$z = 0.5848(1)$ $U_{\text{iso}} = U_{\text{iso}}(\text{Sr1})$	$z = 0.5861(1)$ $U_{\text{iso}} = U_{\text{iso}}(\text{Sr1})$
Sc	$2c (0, 0.5, z)$	$z = 0.3115(2)$ $U_{\text{iso}} = 200(6) \text{ pm}^2$	$z = 0.3045(2)$ $U_{\text{iso}} = 167(8) \text{ pm}^2$	$z = 0.3021(2)$ $U_{\text{iso}} = 71(6) \text{ pm}^2$
O1	$4f (0, 0, z)$	$z = 0.2863(2)$ $U_{\text{iso}} = 260(10) \text{ pm}^2$	$z = 0.2827(3)$ $U_{\text{iso}} = 120(10) \text{ pm}^2$	$z = 0.2801(2)$ $U_{\text{iso}} = 115(8) \text{ pm}^2$
O2	$2c (0, 0.5, z)$	$z = 0.4316(3)$ $U_{\text{iso}} = U_{\text{iso}}(\text{O1})$	$z = 0.4322(4)$ $U_{\text{iso}} = U_{\text{iso}}(\text{O1})$	$z = 0.4288(3)$ $U_{\text{iso}} = U_{\text{iso}}(\text{O1})$
Fe	$2a (0, 0, 0)$	$U_{\text{iso}} = 69(4) \text{ pm}^2$	$U_{\text{iso}} = 61(7) \text{ pm}^2$	$U_{\text{iso}} = 153(6) \text{ pm}^2$
Pn	$2c (0, 0.5, z)$	$z = 0.0887(1)$ $U_{\text{iso}} = 52(4) \text{ pm}^2$	$z = 0.0831(2)$ $U_{\text{iso}} = 40(10) \text{ pm}^2$	$z = 0.0772(2)$ $U_{\text{iso}} = 40(10) \text{ pm}^2$
tetrahedral angle α (°)		108.9(1)	107.1(1)	105.3(1)
Fe-Pn distance (pm)		246.2(1)	239.9(1)	233.6(1)

The chemical pressure applied by partially substituting arsenic by smaller phosphorus atoms leads to a reduction of both lattice parameters and thus also the cell volume. Hereby, all three parameters decrease linearly with increasing P content. While the lattice parameter a only decreases by 0.9 %, c is reduced nearly twice as much by 1.7 %, which results in a reduction of the cell volume by 3.5 %. In the 21311 structure type the lattice parameter c corresponds to the Fe-Fe interlayer distance. Hence, this distance is also reduced by 1.7 %. However, this is not achieved by a compression of the (SrScO_3) interlayer but only by compressing the FePn layer, as demonstrated in Figure 7.4. The total height of the FeP tetrahedral layer in $\text{Sr}_2\text{ScO}_3\text{FeP}$ is 14.4 % smaller than the FeAs layer in $\text{Sr}_2\text{ScO}_3\text{FeAs}$ (highlighted in red in Figure 7.4), whereas the perovskite-like interlayer (highlighted in blue) is even slightly expanded along c by 1.1 %. It is not surprising that only the FePn layer is compressed, as the perovskite-like interlayer is quite stiff in its structure. In $\text{Sr}_2\text{CrO}_3\text{FeAs}$ (cf. Chapter 9), where scandium has been replaced by chromium, the interlayer is only compressed by 2 % as compared to $\text{Sr}_2\text{ScO}_3\text{FeAs}$, although the effective ionic radius of Cr^{3+} (61.5 pm) is ~ 17 % smaller than the one of Sc^{3+} (74.5 pm)^[93]. For comparison: P^{3-} (166 pm) is only ~ 6 % smaller than As^{3-} (176 pm)^[94].

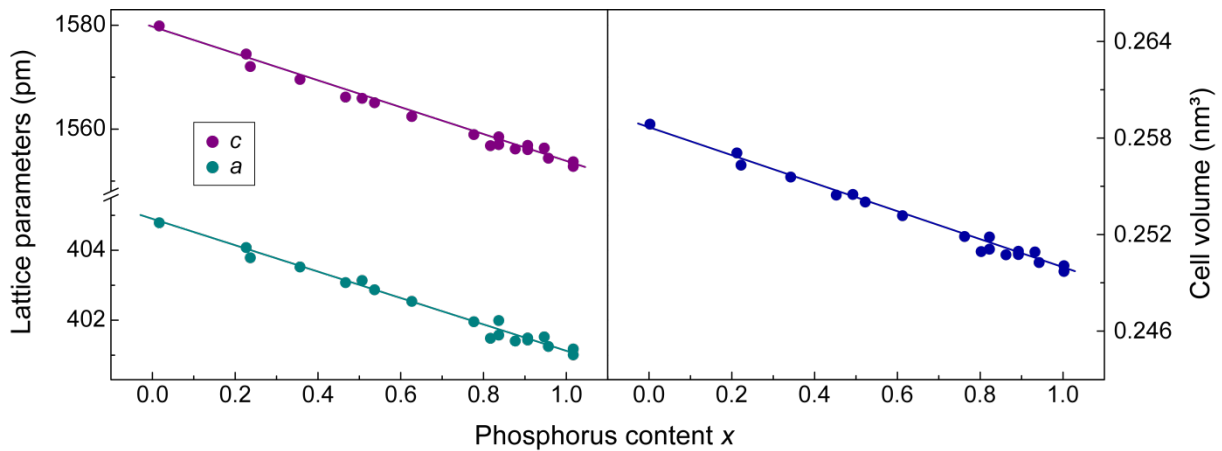


Figure 7.3: Refined lattice parameters (left) and cell volume (right) of $\text{Sr}_2\text{ScO}_3\text{FeAs}_{1-x}\text{P}_x$ as a function of the phosphorus content x .

The strong compression of the FePn layer within the solid solution $\text{Sr}_2\text{ScO}_3\text{FeAs}_{1-x}\text{P}_x$ leads to a significant flattening of the tetrahedra. Figure 7.5 shows the Fe-Pn distance and the tetrahedral angle α (marked in Figure 7.4) as a function of the phosphorus content x . The symmetry of the FeAs tetrahedra in $\text{Sr}_2\text{ScO}_3\text{FeAs}$ is very close to the ideal tetrahedral symmetry with a fourfold tetrahedral angle of 108.9° .

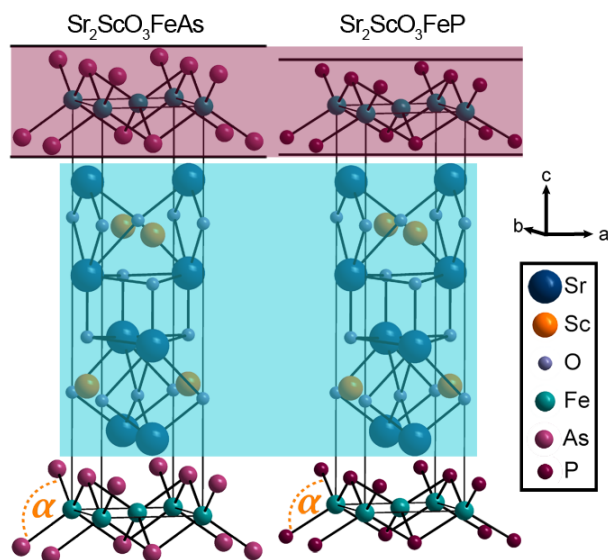


Figure 7.4: Crystal structures of $\text{Sr}_2\text{ScO}_3\text{FeAs}$ (left) and $\text{Sr}_2\text{ScO}_3\text{FeP}$ (right) in direct comparison.

By substitution of As by P, the tetrahedra are compressed along c , whereby α is reduced by 3.3 %. While this reduction proceeds linearly up to phosphorus contents of 61 %, a broader distribution is found for higher contents. The same applies to the course of the Fe- Pn distance. Starting with 246.2 pm at $x = 0$, d is reduced linearly up to $x = 0.61$, then exhibits a broader distribution, and is overall reduced by 5.1 % at $x = 1$. This broad distribution might be due to the higher amount of impurity phases at high P contents, impeding a reliable refinement of the atomic positions.

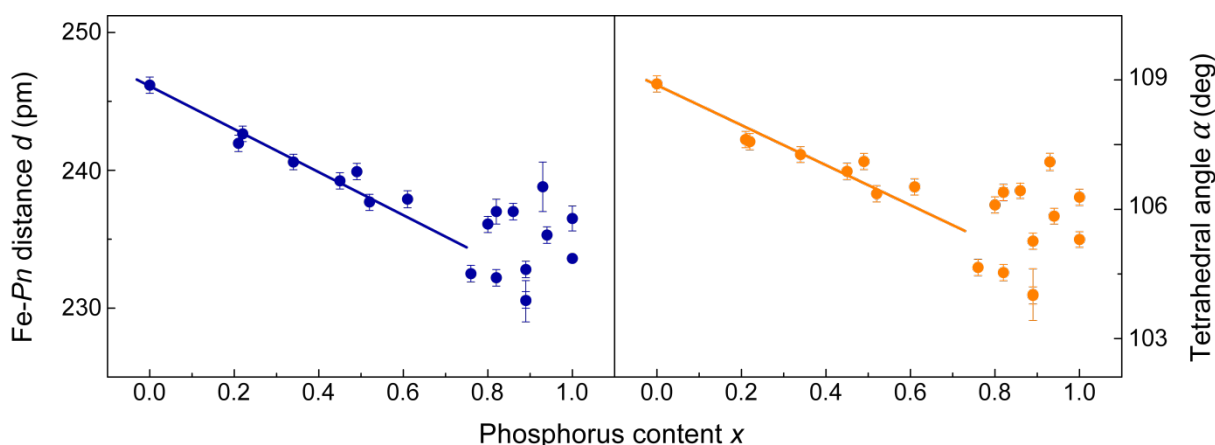


Figure 7.5: Refined Fe- Pn distance d (left) and tetrahedral angle α (right) of $\text{Sr}_2\text{ScO}_3\text{FeAs}_{1-x}\text{P}_x$ as a function of the phosphorus content x .

7.5 Magnetic properties

As the pure phosphorus compound exhibits superconductivity while the pure arsenic compound does not, it is interesting to study at which phosphorus content superconductivity is induced. Figure 7.6 shows the magnetic susceptibilities of several samples with $x = 0.76 - 1.00$. For samples with equal phosphorus contents, superconducting transitions with similar T_c but strongly differing superconducting volume fractions are found (see samples with $x = 0.82$ and $x = 1.00$).

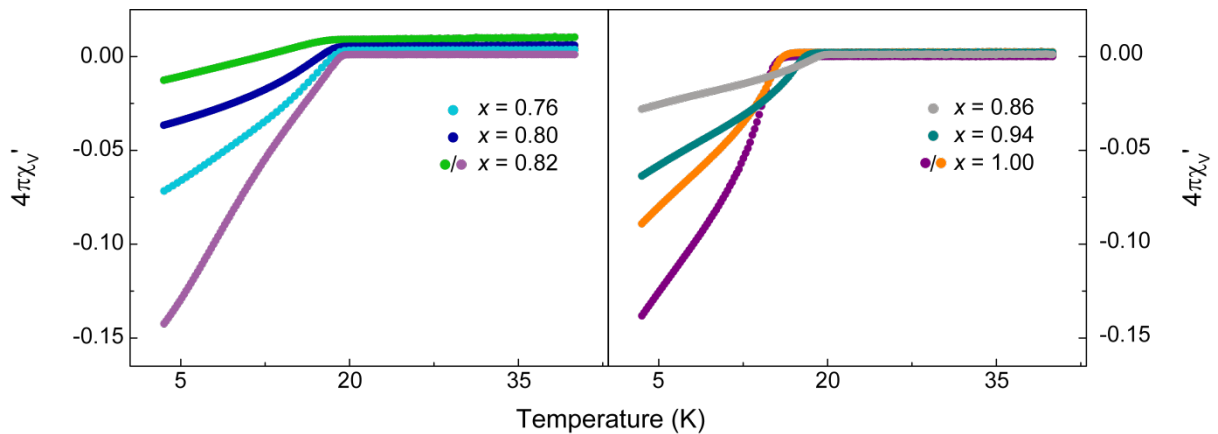


Figure 7.6: Magnetic susceptibilities of several $\text{Sr}_2\text{ScO}_3\text{FeAs}_{1-x}\text{P}_x$ samples.

For a detailed overview of the superconducting properties within this system, the critical temperature T_c and the superconducting volume fraction f_{sc} are plotted in Figure 7.7 as a function of the phosphorus content x . No superconductivity is observed up to $x = 0.45$. However, already in the phosphorus content range of 49 to 61 % traces of superconductivity are detected with superconducting volume fractions of less than 2 %. By further increasing the P content, the critical temperature quickly increases until it reaches its maximum at $x = 0.86$ with $T_c = 19.5$ K. At higher phosphorus contents T_c is reduced again. The samples with $x = 1$ exhibit a T_c of 15.5 K and 15.9 K, thus slightly lower than the critical temperature of 17 K reported in literature^[25].

The small superconducting volume fractions within this system with a maximum of 27 % for $x = 0.89$ might be due to grain boundary effects or so far unknown peculiarities concerning the sample composition. However, as all samples with similar phosphorus contents have similar T_c s but some exhibit strongly differing f_{sc} s, the small volume fractions cannot be ascribed to inhomogeneities within the 21311 phase as this would also affect the critical temperatures. Additionally, small superconducting volume fractions seem to be a general characteristic of the 21311 type of iron-based superconductors, which is still not fully understood, and have been reported before^[95,96].

Nevertheless, analyzing the magnetic properties of $\text{Sr}_2\text{ScO}_3\text{FeAs}_{1-x}\text{P}_x$ has revealed a range of chemical pressure within this solid solution where the superconducting properties are enhanced as compared to the pure phosphorus compound. All samples with a phosphorus content of 67 - 94 % clearly and reproducibly become superconducting at higher temperatures than $\text{Sr}_2\text{ScO}_3\text{FeP}$. Therefore, the optimal structural conditions for superconductivity in this system occur in compounds with less compressed FePn layers than found for $x = 1$.

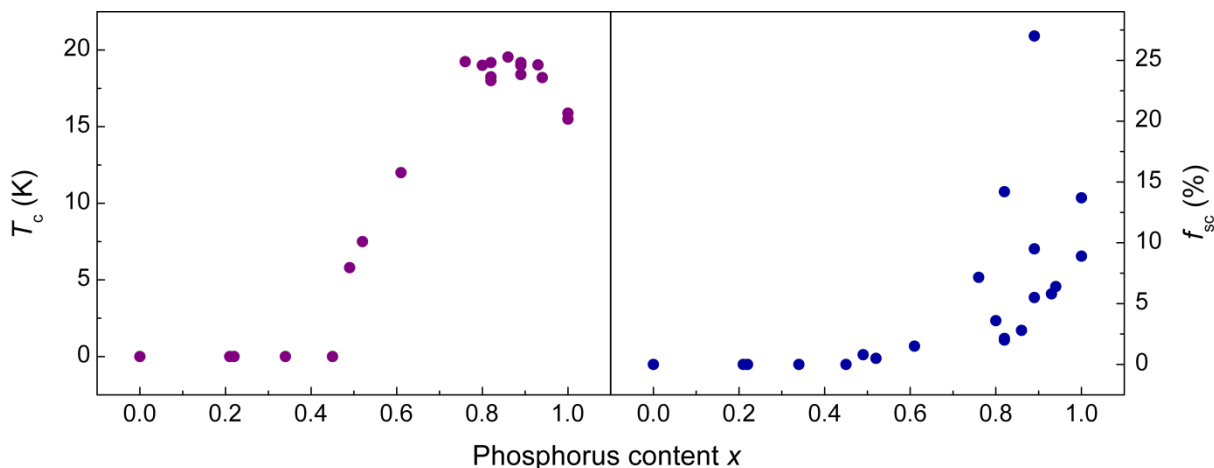


Figure 7.7: Critical temperature (left) and superconducting volume fraction (right) of $\text{Sr}_2\text{ScO}_3\text{FeAs}_{1-x}\text{P}_x$ as a function of the phosphorus content x .

7.6 Conclusion

Applying chemical pressure to $\text{Sr}_2\text{ScO}_3\text{FeAs}$ by substituting arsenic by phosphorus within the solid solution $\text{Sr}_2\text{ScO}_3\text{FeAs}_{1-x}\text{P}_x$ leads to a compression of the $\text{FePn}_{4/4}$ layer, while the perovskite-like interlayer is slightly decompressed. Hereby, the nearly ideal tetrahedral symmetry within the pure arsenic compound is lost and the FePn tetrahedra are flattened. As iron-based superconductors often exhibit the highest critical temperatures when the tetrahedra are close to an ideal symmetry, it is surprising that the pure phosphorus compound with flat tetrahedra is superconducting while the pure arsenic compound with nearly ideal tetrahedra isn't. This indicates that other, still unknown parameters are decisive for the occurrence of superconductivity in this system.

In $\text{Sr}_2\text{ScO}_3\text{FeAs}_{1-x}\text{P}_x$ superconductivity emerges at phosphorus contents of more than 61 %, while traces of superconductivity are already detected at $x = 0.49$. Within this solid solution the maximum T_c of 19.5 K was found for $x = 0.86$ and therefore in a compound with slightly less compressed tetrahedra than in $\text{Sr}_2\text{ScO}_3\text{FeP}$.

It would be interesting to compare the effects of chemical pressure upon $\text{Sr}_2\text{ScO}_3\text{FeAs}$ studied here with the effects of physical pressure as the results might be different. On the one hand, physical pressure might lead to a more uniform compression of the unit cell, whereby not only the FePn layer might be flattened. On the other hand, as mentioned above, the emergence of superconductivity in this system does not seem to depend mainly on structural parameters. Thus, applying physical pressure to $\text{Sr}_2\text{ScO}_3\text{FeAs}$ without introducing phosphorus into the structure might not induce superconductivity at all.

For the isostructural vanadium compound $\text{Sr}_2\text{VO}_3\text{FeAs}$, which is superconducting with a critical temperature of up to 37 K^[97] and will be discussed in detail in Chapter 8, experiments under physical pressure have been reported in literature and led to an enhancement of the critical temperature up to 45 K^[91]. The corresponding phosphorus compound is not known until now. Nevertheless, first experiments on phosphor substitution in $\text{Sr}_2\text{VO}_3\text{FeAs}$ have been performed and revealed promising results. Indications of an enhanced critical temperature at a phosphorus content of 30 % were found. However, in contrast to scandium compounds the reproducibility of T_c for vanadium compounds of the 21311 type is problematic, as will be discussed in Chapter 9.

8 Weak magnetism and the Mott state of vanadium in superconducting $\text{Sr}_2\text{VO}_3\text{FeAs}$

Parts published in: F. Hummel, Y. Su, A. Senyshyn, D. Johrendt, *Physical Review B* **2013**, 88, 144517. DOI: 10.1103/PhysRevB.88.144517

<http://journals.aps.org/prb/abstract/10.1103/PhysRevB.88.144517>

© 2013 American Physical Society

8.1 Introduction

High critical temperatures above 30 K in iron-based superconductors are obviously confined to the scenario of parent compounds exhibiting an antiferromagnetic order of the iron moments, which must be destabilized in order to induce superconductivity. Other iron-pnictide superconductors like LaFePO ,^[98] KFe_2As_2 ,^[99] and LiFeAs ^[58] without magnetic ordering of the stoichiometric parent compound only exhibit critical temperatures well below 20 K. An exception seems to be the iron-arsenide $\text{Sr}_2\text{VO}_3\text{FeAs}$ which is superconducting up to 37 K^[97] and even 45 K under pressure^[91] in its stoichiometric phase. No magnetic ordering in the FeAs layer or structural phase transitions have been found up to now. However, the true stoichiometry of this compound remained a subject of discussion.^[100,101] It was debated whether intrinsic electron doping through oxygen deficiency or $\text{V}^{3+}/\text{V}^{4+}$ mixed valence might play a role.^[102,103] The latter may explain the absence of magnetic ordering; however, oxygen deficiency has never been detected experimentally.

Shortly after the discovery of $\text{Sr}_2\text{VO}_3\text{FeAs}$ it was suspected that this material may constitute a new paradigm, as its electronic structure did not seem to fulfill the Fermi surface (FS) quasineesting condition, which is believed to be essential for high critical temperatures. Hereby, the FS consists of cylinders, which are separated by a so-called nesting vector q (Figure 8.1). These cylinders originate from bands crossing the Fermi level, which are electron like (with the shape of an upwardly open parabola) and hole like (with the shape of a downwardly open parabola).^[10]

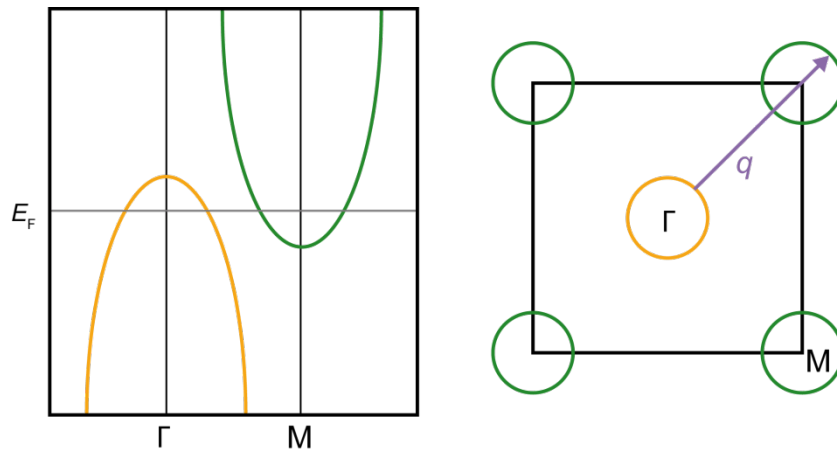


Figure 8.1: Left - Schematic band structure with a hole-like band around Γ and an electron-like band around M. Right - Corresponding schematic Brillouin zone with Fermi surface cylinders and the nesting vector q .

Indeed, first generalized gradient approximation (GGA) calculations predicted half-metallic V $3d$ bands and magnetic properties inconsistent with experimental data.^[104] Weak hybridization between the V $3d$ and Fe $3d$ bands near E_F changes the FS topology significantly and destroys the quasinesting.^[104,105] However, by weighting the electronic states of this more complex FS with their Fe character, an FS was obtained that again supports the quasinesting model.^[106] The latter was also confirmed by angle-resolved photoemission experiments with $\text{Sr}_2\text{VO}_3\text{FeAs}$ crystals.^[107] It was suggested that magnetic ordering of the V sublattice could remove the V $3d$ states from the Fermi level by magnetic exchange splitting, so as to maintain the characteristic quasinested FS topology. First evidence for such magnetic ordering was found by neutron scattering,^[95] but the magnetic structure remained unclear. Antiferromagnetic ordering of the V sublattice was also indicated by muon spin rotation (μSR) and NMR-spectroscopy.^[108,109] Local-density approximation calculations with the Hubbard U correction (LDA+ U) revealed an antiferromagnetic ground state with a gap in the V $3d$ bands and a magnetic moment of $\sim 1.8 \mu_B$ per vanadium.^[110] In this case, the magnetic exchange splitting would be large enough to open a significant gap in the V $3d$ bands, but on the other hand, a magnetic moment of such magnitude has not been observed by any experiment so far.

In this chapter neutron powder-diffraction data of polycrystalline $\text{Sr}_2\text{VO}_3\text{FeAs}$ are presented along with density functional theory (DFT) calculations to understand the results. By using polarized neutrons it is shown that antiferromagnetic ordering evolves around 45 K with a magnetic moment of $\sim 0.1 \mu_B$ per vanadium, thus more than one order of magnitude smaller than the LDA+ U prediction. GGA plus exact exchange of correlated electrons (EECE) calculations reveal that the V $3d$ orbitals are in a Mott state and subject to strong on-site

repulsion correlations which remove the V states from the Fermi level without significant magnetic moment, leading to a consistent picture of this superconducting material.

8.2 Experimental details

A polycrystalline sample of $\text{Sr}_2\text{VO}_3\text{FeAs}$ (4 g) was synthesized in four separate 1-g batches. Stoichiometric mixtures of Sr, V, Fe_2O_3 , and As_2O_3 were transferred into alumina crucibles and sealed in silica ampoules. The samples were heated up to 1323 K for 60 h at rates of 60 K/h and 200 K/h for heating and cooling, respectively. Afterwards, the samples were homogenized, pressed into pellets, and sintered for 60 h at 1323 K. The batches were then united, homogenized, pressed into two pellets (both pellets being placed in the same alumina crucible), and sintered again for 60 h at 1323 K. The product was obtained as a black, polycrystalline air-stable sample.

Room-temperature X-ray powder-diffraction patterns were recorded using the STOE diffractometer (Mo- $K_{\alpha 1}$ radiation). Room-temperature high-resolution neutron diffraction data were measured at SPODI. Measurements with polarized neutrons were recorded at the polarized neutron spectrometer DNS. For Rietveld refinements of the data the TOPAS package^[30] was used with March Dollase or spherical harmonics functions to describe the preferred orientation of the crystallites. Magnetic measurements were performed using the SQUID magnetometer.

Electronic band structure calculations were performed with the WIEN2k program package^[42] with a separation energy for core and valence states of -6 Ry, whereby 56 irreducible k points were used. The muffin-tin sphere radii R_{MT} (in a.u.) were 2.30 for Sr, 1.92 for V, 2.30 for Fe, 2.21 for As, and 1.73 for O. In order to reproduce the Mott insulating state of the vanadium-oxide layer in $\text{Sr}_2\text{VO}_3\text{FeAs}$, the EECE approach implemented in the package was used.^[111] The functional is obtained by removing the local exchange-correlation energy of the V 3d orbitals and replacing it with the exact Hartree-Fock exchange energy. Thus the exchange term is corrected by an exact expression instead of approximations, as in LDA+ U or GGA+ U schemes.

8.3 Crystal structure

Rietveld refinements of the X-ray and SPODI neutron data (Figure 8.2 and Table 8.1) revealed the sample composition 91.3 % $\text{Sr}_2\text{VO}_3\text{FeAs}$ with 3.2 % $\text{Sr}_3\text{V}_2\text{O}_{7-x}$, 2.2 % orthorhombic Sr_2VO_4 , and 3.3 % FeAs as impurity phases (wt %). No oxygen deficiency was detected in the $\text{Sr}_2\text{VO}_3\text{FeAs}$ phase, since both oxygen sites remained fully occupied within the experimental errors during the refinement. Also, no vanadium was detected on the iron site; hence, the $\text{Sr}_2\text{VO}_3\text{FeAs}$ phase in the sample turns out to be stoichiometric.

Compared to the isostructural scandium compound which has been discussed in the previous chapter, the lattice parameters of $\text{Sr}_2\text{VO}_3\text{FeAs}$ are decreased by 3 % (a) and 0.7 % (c). Thus, the cell volume of this compound is 6 % smaller than the one found for $\text{Sr}_2\text{ScO}_3\text{FeAs}$. The Fe-As distance of ~ 242 pm is about 2 % longer in the vanadium compound and the FeAs tetrahedra are nearly ideal with a fourfold tetrahedral angle of 109.7° . While the total height of the FeAs layer is ~ 281 pm and bigger than the one in $\text{Sr}_2\text{ScO}_3\text{FeAs}$, the interlayer height in $\text{Sr}_2\text{VO}_3\text{FeAs}$ is smaller with only ~ 972 pm.

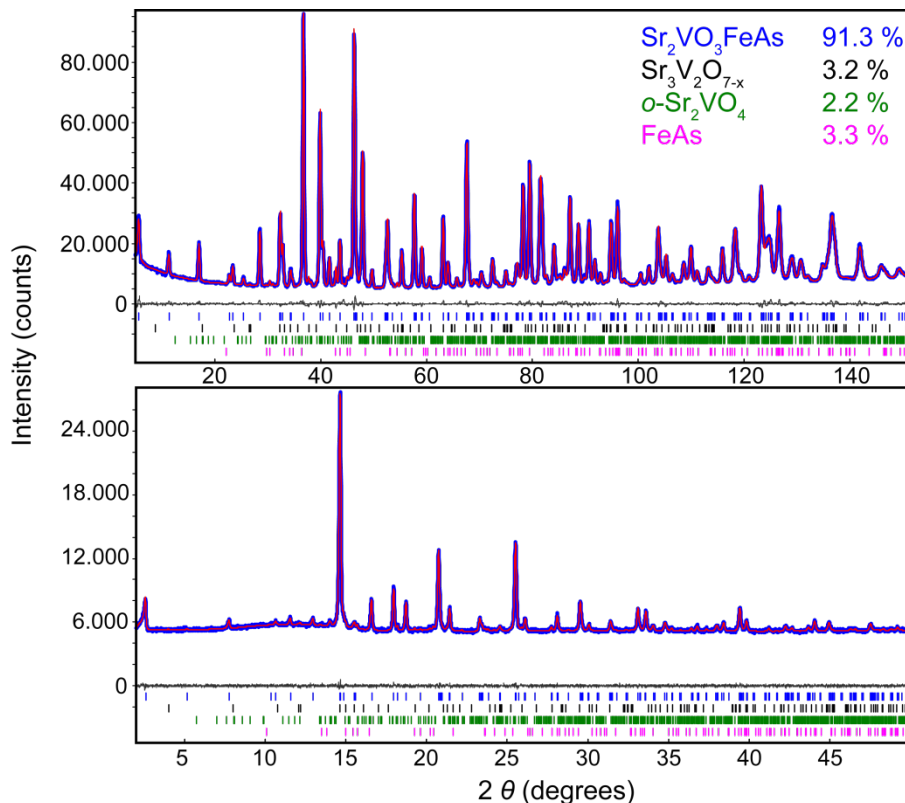


Figure 8.2: X-ray (bottom) and SPODI neutron (top) powder-diffraction pattern (blue) of $\text{Sr}_2\text{VO}_3\text{FeAs}$ with Rietveld refinements (red).

Table 8.1: Crystallographic data for Sr₂VO₃FeAs.

Sr ₂ VO ₃ FeAs		
diffractometer	STOE (X-ray)	SPODI (neutron)
wavelength (nm)	0.07093	0.1548
space group	<i>P4/nmm</i> (no. 129, o1)	<i>P4/nmm</i> (no. 129, o1)
molar mass (g/mol)	404.9463	404.9463
lattice parameter <i>a</i> (pm)	393.67(1)	393.47(1)
lattice parameter <i>c</i> (pm)	1569.18(4)	1569.01(1)
cell volume (nm ³)	0.24318 (1)	0.24292(1)
density (g/cm ³)	5.53(1)	5.53(1)
<i>Z</i>	2	2
data points	4800	2939
reflections (all phases)	1209	1369
refined parameters	73	76
<i>R_p</i> , <i>wR_p</i>	0.010, 0.013	0.021, 0.028
<i>R_{bragg}</i> , χ^2	0.002, 0.977	0.009, 3.005
atomic parameters		
Sr1 2 <i>c</i> (0, 0.5, <i>z</i>)	<i>z</i> = 0.8097(2) <i>U_{iso}</i> = 74(9) pm ²	<i>z</i> = 0.8099(1) <i>U_{iso}</i> = 43(3) pm ²
Sr2 2 <i>c</i> (0, 0.5, <i>z</i>)	<i>z</i> = 0.5861(3) <i>U_{iso}</i> = 130(10) pm ²	<i>z</i> = 0.5860(1) <i>U_{iso}</i> = 89(3) pm ²
V 2 <i>c</i> (0, 0.5, <i>z</i>)	<i>z</i> = 0.3092(3) <i>U_{iso}</i> = 70(20) pm ²	<i>z</i> = 0.3020(20) <i>U_{iso}</i> = 40(40) pm ²
O1 4 <i>f</i> (0, 0, <i>z</i>)	<i>z</i> = 0.2955(6) <i>U_{iso}</i> = 40(30) pm ²	<i>z</i> = 0.2934(1) <i>U_{iso}</i> = 52(3) pm ²
O2 2 <i>c</i> (0, 0.5, <i>z</i>)	<i>z</i> = 0.4293(7) <i>U_{iso}</i> = <i>U_{iso}</i> (O1)	<i>z</i> = 0.4299(1) <i>U_{iso}</i> = 80(4) pm ²
Fe 2 <i>a</i> (0, 0, 0)	<i>U_{iso}</i> = 100(10) pm ²	<i>U_{iso}</i> = 38(2) pm ²
As 2 <i>c</i> (0, 0.5, <i>z</i>)	<i>z</i> = 0.0896(3) <i>U_{iso}</i> = 80(10) pm ²	<i>z</i> = 0.0894(1) <i>U_{iso}</i> = 38(3) pm ²
tetrahedral angle α (°)	109.8(1)	109.7(1)
Fe-As distance (pm)	241.9(2)	241.6(1)

8.4 Magnetic properties

Magnetic susceptibility measurements (Figure 8.3) revealed that the sample is superconducting with $T_c = 25$ K. Thus, this stoichiometric $\text{Sr}_2\text{VO}_3\text{FeAs}$ has a comparably low T_c , which contradicts to the work of Han *et al.* where nominally stoichiometric samples exhibit the highest critical temperatures and decreasing values were attributed to oxygen deficiencies.^[102] The superconducting volume fraction of the sample presented here is roughly estimated to be about 26 %. Although most experimental works about $\text{Sr}_2\text{VO}_3\text{FeAs}$ do not mention the superconducting volume fractions achieved, such small values have been reported before^[95] and seem to be another general peculiarity in this system besides the strongly differing superconducting transition temperatures.

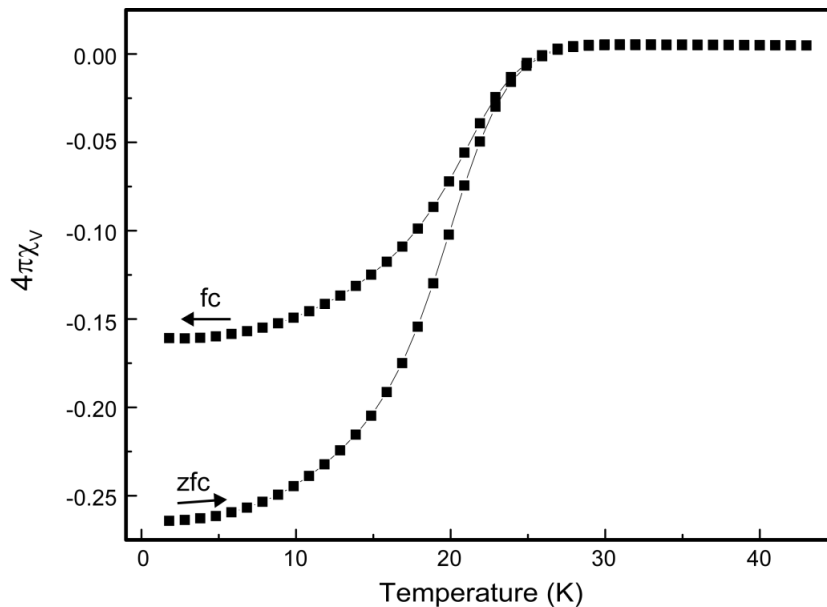


Figure 8.3: Zero-field-cooled/field-cooled susceptibility of $\text{Sr}_2\text{VO}_3\text{FeAs}$ at 15 Oe.

Earlier neutron-diffraction experiments revealed weak additional reflections at low temperatures which indicate possible magnetic ordering of vanadium.^[95] In order to clarify the origin of these reflections, low-temperature diffraction experiments with polarized neutrons were performed. Hereby, nuclear and magnetic reflections can be separated from each other and from the spin incoherent scattering. Figure 8.4 shows the intensity relation between all three contributions. All intensities have been normalized to the total spin incoherent scattering cross section of vanadium. It is evident that the magnetic scattering is very small compared to the nuclear part. Nevertheless, significant magnetic peaks are visible (see the inset of Figure 8.4).

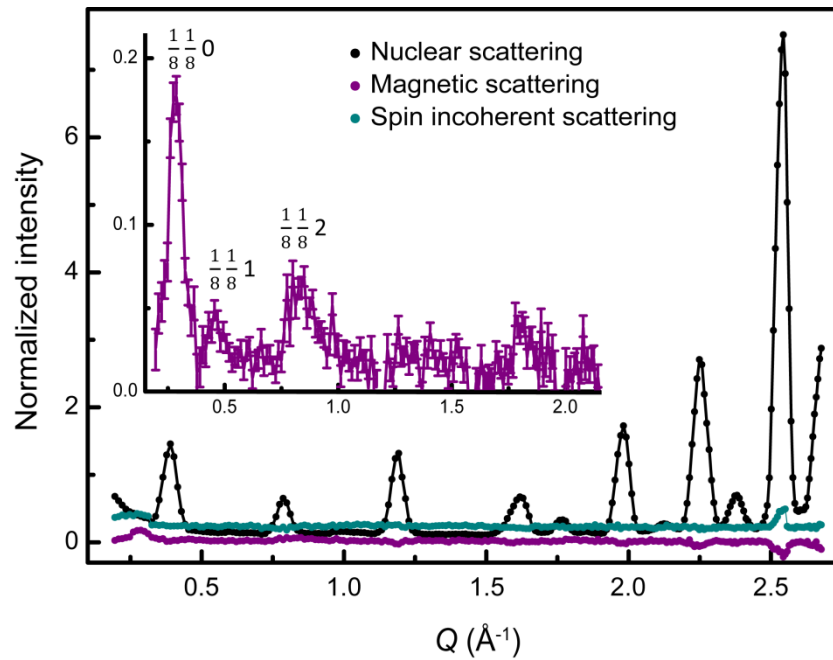


Figure 8.4: DNS neutron scattering pattern of $\text{Sr}_2\text{VO}_3\text{FeAs}$ at 2 K divided into nuclear (black), magnetic (purple) and spin incoherent (green) contributions. Inset: Enlarged image of the magnetic contribution.

These reflections differ from those observed earlier^[95] because of the spin incoherent scattering contribution. Due to the large incoherent scattering length of ^{51}V this contribution causes a strong scattering background. As can be seen in Figure 8.5, the overall scattering intensities obtained at DNS at 2 K before polarization analysis (Figure 8.5, top) would have led to very similar results as published by *Tege/ et al.*^[95] (Figure 8.5, bottom, assumed magnetic reflections marked by black arrows). However, the polarization analysis allows to filter out the true magnetic reflections shown in the inset of Figure 8.4. These reflections can be indexed as $\frac{1}{8} \frac{1}{8} l$ and thus point to a magnetic ordering of the vanadium moments with a propagation vector $q = \left(\frac{1}{8}, \frac{1}{8}, 0\right)$. Due to different intensities of the reflections, it is assumed that the magnetic moments are aligned along [001].

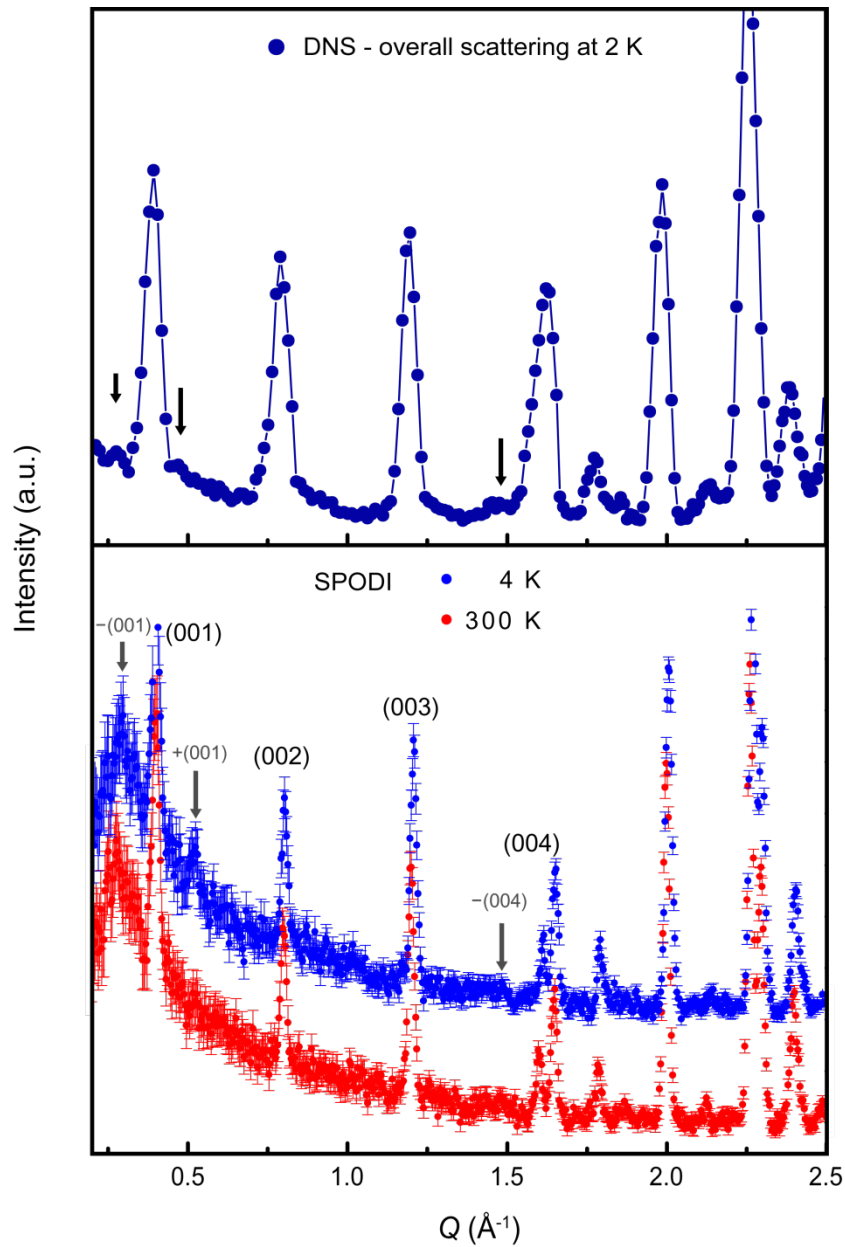


Figure 8.5: Overall DNS neutron scattering pattern of $\text{Sr}_2\text{VO}_3\text{FeAs}$ at 2 K (top) and SPODI neutron scattering patterns at 4 K and 300 K as published by *TegeI et al.*^[95] (bottom).

The temperature dependency of the magnetic ordering parameter is shown in Figure 8.6. The magnetic transition at about 45 K is consistent with magnetic susceptibility measurements.^[95,103] These showed anomalies around 50 K, which are related to the magnetic transition reported here. However, the neutron experiments showed no significant change of the diffraction pattern in the temperature range of the further reported susceptibility anomalies around 70 K and 150 K.

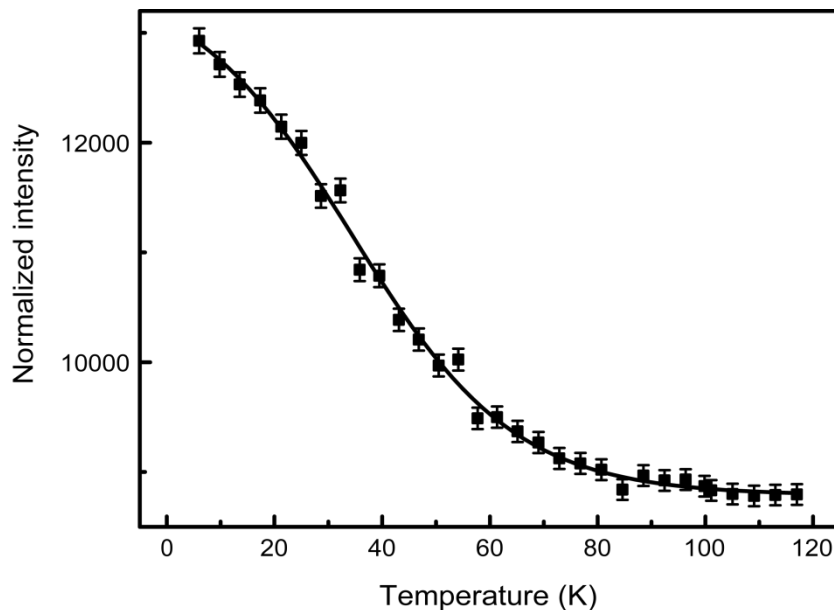


Figure 8.6: Temperature dependency of the magnetic ordering parameter of the V sublattice in $\text{Sr}_2\text{VO}_3\text{FeAs}$ measured at $Q = 0.29 \text{ \AA}^{-1}$.

From the magnetic scattering intensity an ordered magnetic moment of $\sim 0.1 \mu_B/\text{V}$ is estimated in agreement with the μSR experiments,^[108] but in stark contrast to LDA+ U calculations, which predicted much higher values around $1.8 \mu_B/\text{V}$.^[110] However, the magnetic exchange splitting of a $0.1\text{-}\mu_B$ magnetic moment is certainly too small to remove the V $3d$ states from the Fermi energy. This suggests that the V atoms in $\text{Sr}_2\text{VO}_3\text{FeAs}$ are in a Mott state where the electronic correlation is dominated by the on-site Coulomb repulsion, but without magnetic ordering.

8.5 DFT calculations

In order to check this idea, GGA+EECE calculations were performed with an exact (Hartree-Fock) exchange correction applied to the V $3d$ orbitals without magnetic moment. Figure 8.7 shows the band structures and Fermi surfaces of non-magnetic $\text{Sr}_2\text{VO}_3\text{FeAs}$ calculated with standard GGA and with GGA+EECE, respectively. The standard GGA calculation produces metallic V $3d$ bands and consequently an FS which is more complex due to the hybridization of V $3d$ with Fe $3d$ bands. By applying the EECE functional, the V $3d$ bands are shifted to much lower energies, and the vicinity of the Fermi energy is now dominated by the Fe $3d$ states as known from other iron-arsenide materials. Even without magnetic moment, the FS shows the quasineesting between hole-like and electron-like cylinders, which is the typical FS topology of iron-arsenide superconductors.

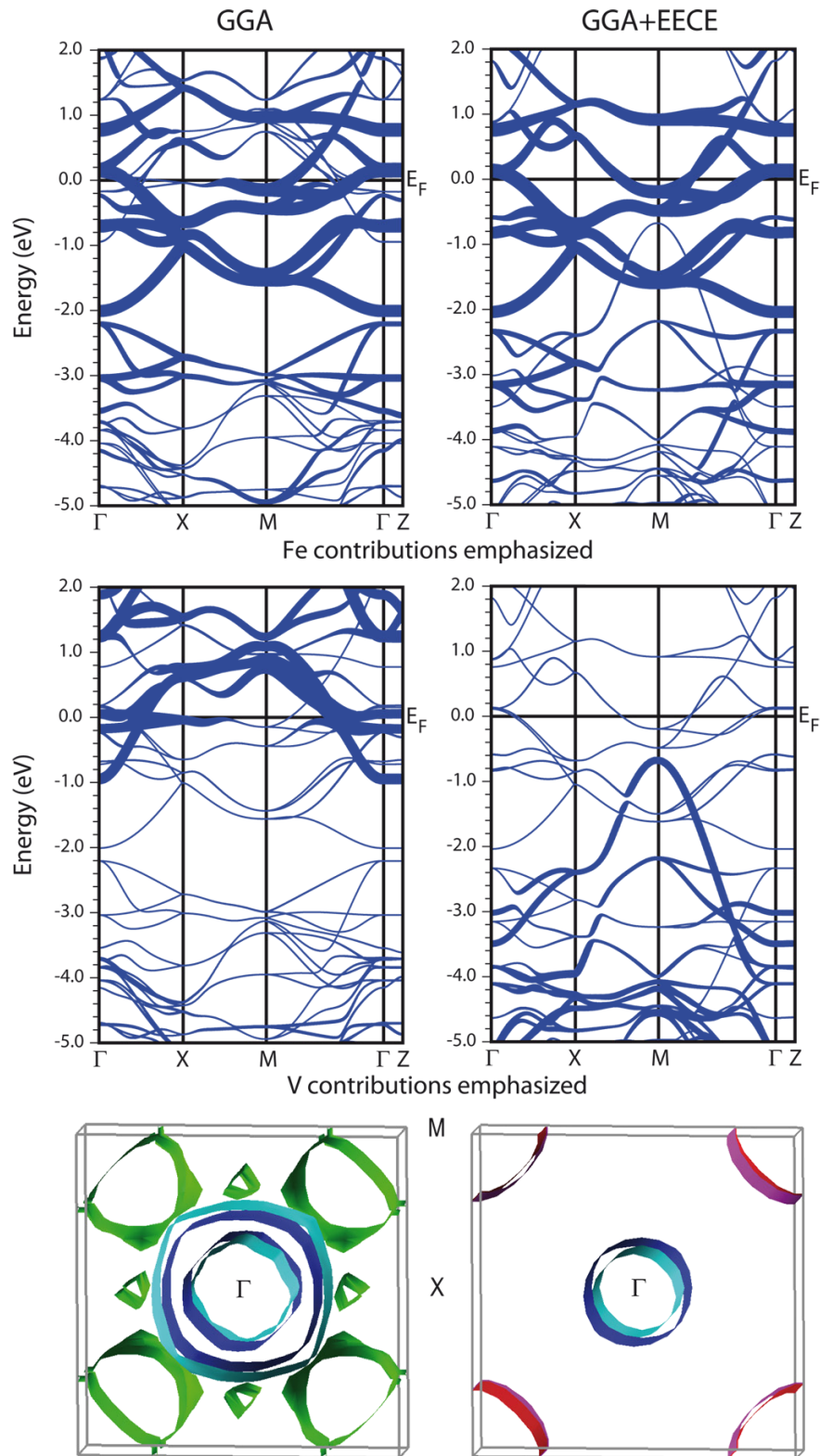


Figure 8.7: Band structure of $\text{Sr}_2\text{VO}_3\text{FeAs}$ with iron (top) and vanadium (middle) contributions emphasized and Fermi surface (bottom) calculated with GGA (left) and GGA+EECE (right).

LDA plus dynamical mean-field theory (DMFT) calculations provide similar results.^[112] However, the absence of magnetic ordering in the Fe sublattice and the emergence of superconductivity in the stoichiometric phase indicates that $\text{Sr}_2\text{VO}_3\text{FeAs}$ is intrinsically doped, probably by a certain degree of $\text{V}^{3+}/\text{V}^{4+}$ mixed valence.

8.6 Conclusion

These results consistently show that $\text{Sr}_2\text{VO}_3\text{FeAs}$ is a typical iron-arsenide superconductor with quasinested FS topology. No deviations from the ideal composition were found by Rietveld refinements of neutron powder patterns, ruling out oxygen deficiency as well as V doping at the Fe site. Magnetic ordering in the V sublattice was detected by polarized-neutron scattering with a probable propagation vector $q = \left(\frac{1}{8}, \frac{1}{8}, 0\right)$. The estimated ordered moment of $0.1 \mu_{\text{B}}/\text{V}$ is much smaller than recently predicted by LDA+ U calculations, and certainly too small to produce a significant gap in the V $3d$ bands by magnetic exchange splitting. However, DFT calculations using a GGA+EECE functional revealed the typical quasinested FS even without magnetic moment. The V atoms are in a Mott state where the electronic correlations are dominated by on-site Coulomb repulsion, which shifts the V $3d$ states away from the Fermi energy. Given the ideal stoichiometry of $\text{Sr}_2\text{VO}_3\text{FeAs}$, intrinsic electron doping through $\text{V}^{3+}/\text{V}^{4+}$ mixed valence may be responsible for the absence of spin-density wave ordering and thus for superconductivity.

9 Superconductivity in $\text{Sr}_2\text{V}_{1-x}\text{Cr}_x\text{O}_3\text{FeAs}$

9.1 Introduction

In iron-based superconductors it is still not fully understood which factors are decisive for the emergence of superconductivity. Typically, superconductivity can be induced in parent compounds by electron, hole, or isoelectronic doping or by applying pressure. Through these methods it is also possible to vary the critical temperature of a system. As all of these modifications always affect more than only one property of the system, it is often hard to find out which feature is the most decisive one. For example, hole doping of BaFe_2As_2 by partial substitution of Ba by K^[113], which leads to superconductivity, does not only result in a reduction of the total number of electrons but also structural changes due to the smaller size of potassium compared to barium.

For $\text{Sr}_2\text{VO}_3\text{FeAs}$ superconductivity has been reported with strongly differing T_c s, varying from 13 to 37 K^[97,102]. It is still unclear, by which factors this critical temperature can be controlled. As possible influencing factors the lattice parameters, a mixed valence of vanadium, or a hypothetical oxygen deficiency are discussed.^[97,101,103] What is known with certainty from muon spin rotation (μSR), NMR, and neutron experiments is that the compound exhibits a weak magnetic ordering of the vanadium moments.^[96,108,109]

In contrast to this, the isostructural compound $\text{Sr}_2\text{CrO}_3\text{FeAs}$ is not superconducting, but shows robust antiferromagnetic ordering of the Cr^{3+} moments ($2.75 \mu_B/\text{Cr}$, $T_N = 36 \text{ K}$)^[114]. From this, one might infer that the strong magnetic moments at the Cr sites interfere with superconductivity, while the weak moments at the V sites do not. However, neutron diffraction studies suggest that the absence of superconductivity in $\text{Sr}_2\text{CrO}_3\text{FeAs}$ is not inevitably ascribed to magnetic ordering. A slight substitution of chromium for iron atoms in the superconducting FeAs layer ($\sim 7\%$) was detected, which may also be a reason for the absence of superconductivity.

Here, the solid solution $\text{Sr}_2\text{V}_{1-x}\text{Cr}_x\text{O}_3\text{FeAs}$ is reported. This system comprises a large amount of possible control factors for the emergence and the critical temperature of superconductivity. Firstly, there are the factors discussed above for both $\text{Sr}_2\text{VO}_3\text{FeAs}$ and $\text{Sr}_2\text{CrO}_3\text{FeAs}$, like the mixed valence of vanadium, the strong magnetism of chromium and a mixed occupancy of the iron site. Secondly, there are additional factors due to the mixing of V and Cr, such as the structural change by partially substituting vanadium by chromium and a possible electronic doping. Therefore, the solid solution $\text{Sr}_2\text{V}_{1-x}\text{Cr}_x\text{O}_3\text{FeAs}$ opens an opportunity to study the effects of these factors upon the physical properties of the

compounds. By a combined X-ray, EDX, SQUID, neutron scattering, and XPS analysis it is investigated at which point superconductivity is suppressed and whether oxidation states, structural features, magnetism, or the composition of the FeAs layer are crucial to the superconducting properties of the system.

9.2 Experimental details

Polycrystalline samples (0.3 g) of $\text{Sr}_2\text{V}_{1-x}\text{Cr}_x\text{O}_3\text{FeAs}$ (nominal values for $x = 0 - 1$ with a step size of 0.1) were synthesized by heating stoichiometric mixtures of Sr, V, Cr, Fe_2O_3 , and As_2O_3 in alumina crucibles which were sealed in silica ampoules. The reaction mixtures were heated up to 1323 K for 60 h at rates of 60 and 200 K/h for heating and cooling, respectively. After this, the samples were homogenized, pressed into pellets, and sintered for 60 h at 1323 K (with rates of 100 and 200 K/h for heating and cooling, respectively). This sintering step was performed twice. For neutron experiments larger samples (2 - 4 g; with $x = 0, 0.1, 0.3, 0.4, 0.5, 0.8$) were synthesized likewise but using two to four separate 1- or 1.1-g batches for each sample. The separate batches were united after the first sintering step, homogenized together, then pressed into pellets, and sintered for the second time. If the sample quality, verified by X-ray powder-diffraction and susceptibility measurements, was insufficient, a third sintering step was performed.

Room-temperature X-ray powder-diffraction patterns were recorded using the Huber diffractometer with $\text{Cu-K}\alpha_1$ radiation. High-resolution neutron diffraction patterns at 4 K and 297 K were measured at SPODI. For Rietveld refinements of the diffraction data the TOPAS package^[30] was used with March Dollase or spherical harmonics functions to describe the preferred orientation of the crystallites. Shape anisotropy effects were described by the approach of *Le Bail* and *Jouanneaux*^[31]. Energy dispersive X-ray (EDX) experiments were performed on the Jeol JSM-6500 FE SEM. For magnetic measurements the SQUID magnetometer and the AC susceptometer were used. X-ray photoelectron spectroscopy (XPS) measurements were performed as described in Chapter 2.9. For the fitting of the data, the FWHM of the V^{5+} signal was held at 0.95 eV according to [115]. Because of broad variations in literature^[115-118], the FWHM of the V^{4+} signal was freely refined at first, then averaged, and held at this value (1.9 eV) for the final fitting of the data. To neglect charging effects, a fixed energy spacing between V^{5+} and V^{4+} was set ($E_{\text{B}}(\text{V}^{5+}) - E_{\text{B}}(\text{V}^{4+}) = 1.0$ eV), while the absolute energy values were refined freely in the fitting routine.

9.3 Results and discussion

The solid solution $\text{Sr}_2\text{V}_{1-x}\text{Cr}_x\text{O}_3\text{FeAs}$ was successfully synthesized with nominal values for x of 0 to 1 with a step size of 0.1 and the products were obtained as black polycrystalline air-stable samples. The effective chromium content of each sample was determined via EDX measurements. Only a small discrepancy between nominal and actual chromium content was observed (Figure 9.1). Hereafter only the experimentally determined values for x will be used.

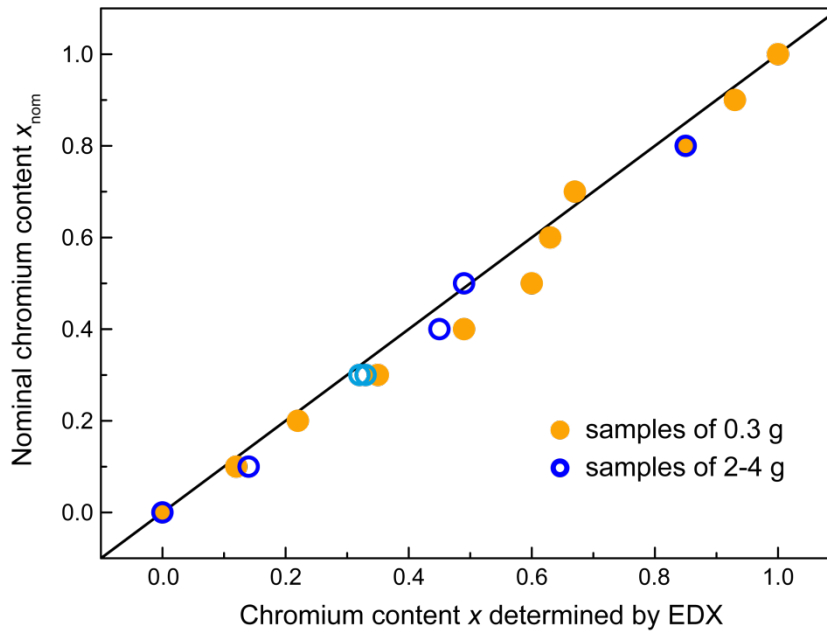


Figure 9.1: Relation between the nominal Cr content and the one determined by EDX.

Rietveld refinements of the X-ray and SPODI neutron data revealed that samples with higher chromium contents contain less impurity phases. Figure 9.2 exemplarily shows an X-ray powder-diffraction pattern of two of the 0.3-g samples and the neutron data of one of the 2- to 4-g samples, each including the respective Rietveld refinement. The corresponding crystallographic data are compiled in Table 9.1. As impurity phases orthorhombic Sr_2VO_4 , tetragonal Sr_2VO_4 , SrO, and FeAs were detected. The 0.3-g samples exhibit a main phase fraction of 97 to 100 wt% and of 91 wt% in only one sample, while the larger samples have a main phase fraction of 81 to 95 wt% and of only 65 wt% in one sample.

Table 9.1: Crystallographic data for $\text{Sr}_2\text{V}_{1-x}\text{Cr}_x\text{O}_3\text{FeAs}$ with $x = 0.45, 0.67, \text{ and } 1$.

$\text{Sr}_2\text{V}_{1-x}\text{Cr}_x\text{O}_3\text{FeAs}$				
space group	$P4/nmm$ (no. 129, $o1$)			
chromium content x	0.45	0.67	1	
diffractometer	SPODI (neutron)	Huber (X-ray)	Huber (X-ray)	
wavelength (nm)	0.1548	0.15406	0.15406	
molar mass (g/mol)	405.421	405.653	406.001	
lattice parameter a (pm)	392.32(1)	391.23(1)	390.65(1)	
lattice parameter c (pm)	1570.02(3)	15.6893(3)	1575.52(3)	
cell volume (nm^3)	0.24164(1)	0.24013(1)	0.24044(1)	
density (g/cm^3)	5.28(1)	5.61(1)	5.61(1)	
Z	2	2	2	
data points	2939	18901	18901	
reflections (all phases)	425	108	107	
refined parameters	75	81	81	
R_p, wR_p	0.033, 0.044	0.013, 0.019	0.012, 0.016	
R_{bragg}, χ^2	0.013, 2.429	0.006, 1.353	0.006, 1.156	
atomic parameters				
Sr1	$2c$ (0, 0.5, z)	$z = 0.8081(2)$ $U_{\text{iso}} = 38(6) \text{ pm}^2$	$z = 0.8061(1)$ $U_{\text{iso}} = 84(3) \text{ pm}^2$	$z = 0.8044(1)$ $U_{\text{iso}} = 68(3) \text{ pm}^2$
Sr2	$2c$ (0, 0.5, z)	$z = 0.5859(2)$ $U_{\text{iso}} = 57(7) \text{ pm}^2$	$z = 0.5848(1)$ $U_{\text{iso}} = 157(4) \text{ pm}^2$	$z = 0.5845(1)$ $U_{\text{iso}} = 100(3) \text{ pm}^2$
V/Cr	$2c$ (0, 0.5, z)	$z = 0.3073(7)$ $U_{\text{iso}} = 40(30) \text{ pm}^2$	$z = 0.3126(1)$ $U_{\text{iso}} = 98(6) \text{ pm}^2$	$z = 0.3124(1)$ $U_{\text{iso}} = 94(5) \text{ pm}^2$
O1	$4f$ (0, 0, z)	$z = 0.2933(1)$ $U_{\text{iso}} = 38(5) \text{ pm}^2$	$z = 0.2976(3)$ $U_{\text{iso}} = 137(9) \text{ pm}^2$	$z = 0.2951(2)$ $U_{\text{iso}} = 43(8) \text{ pm}^2$
O2	$2c$ (0, 0.5, z)	$z = 0.4298(2)$ $U_{\text{iso}} = 64(8) \text{ pm}^2$	$z = 0.4284(3)$ $U_{\text{iso}} = U_{\text{iso}}(\text{O1})$	$z = 0.4295(3)$ $U_{\text{iso}} = U_{\text{iso}}(\text{O1})$
Fe	$2a$ (0, 0, 0)	$U_{\text{iso}} = 38(5) \text{ pm}^2$	$U_{\text{iso}} = 135(5) \text{ pm}^2$	$U_{\text{iso}} = 121(4) \text{ pm}^2$
As	$2c$ (0, 0.5, z)	$z = 0.0896(2)$ $U_{\text{iso}} = 38(6) \text{ pm}^2$	$z = 0.0920(1)$ $U_{\text{iso}} = 41(4) \text{ pm}^2$	$z = 0.0907(1)$ $U_{\text{iso}} = 79(4) \text{ pm}^2$

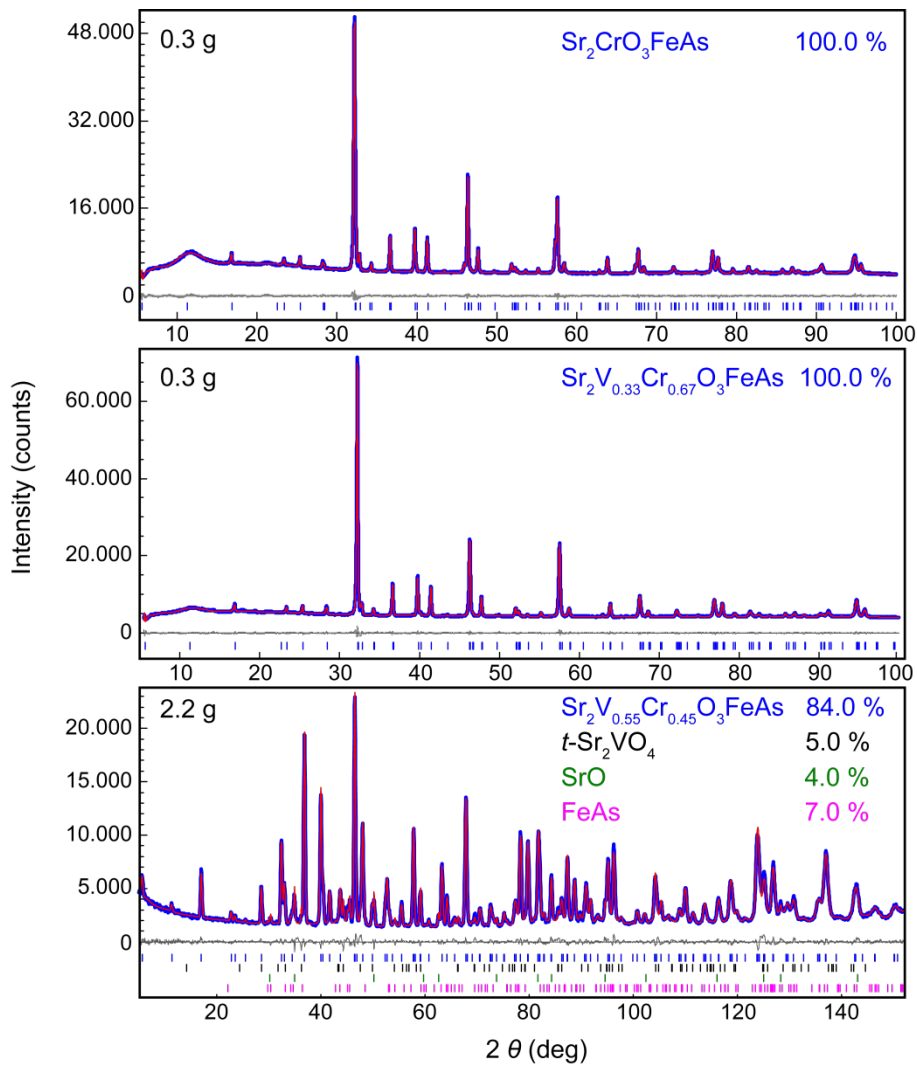


Figure 9.2: X-ray powder-diffraction pattern (blue) for $\text{Sr}_2\text{V}_{1-x}\text{Cr}_x\text{O}_3\text{FeAs}$ with $x = 1$ (top), $x = 0.67$ (middle) and neutron powder-diffraction pattern (blue) with $x = 0.45$ (bottom) with Rietveld refinements (red).

Magnetic susceptibility measurements revealed superconductivity in samples with a chromium content of up to 63 % and show traces of superconductivity even up to $x = 0.85$. Figure 9.3 shows the susceptibility data of all superconducting samples.

To get a better overview of the superconducting properties of the samples, Figure 9.4 shows the critical temperature and superconducting volume fraction (f_{sc}) as a function of the chromium content x .

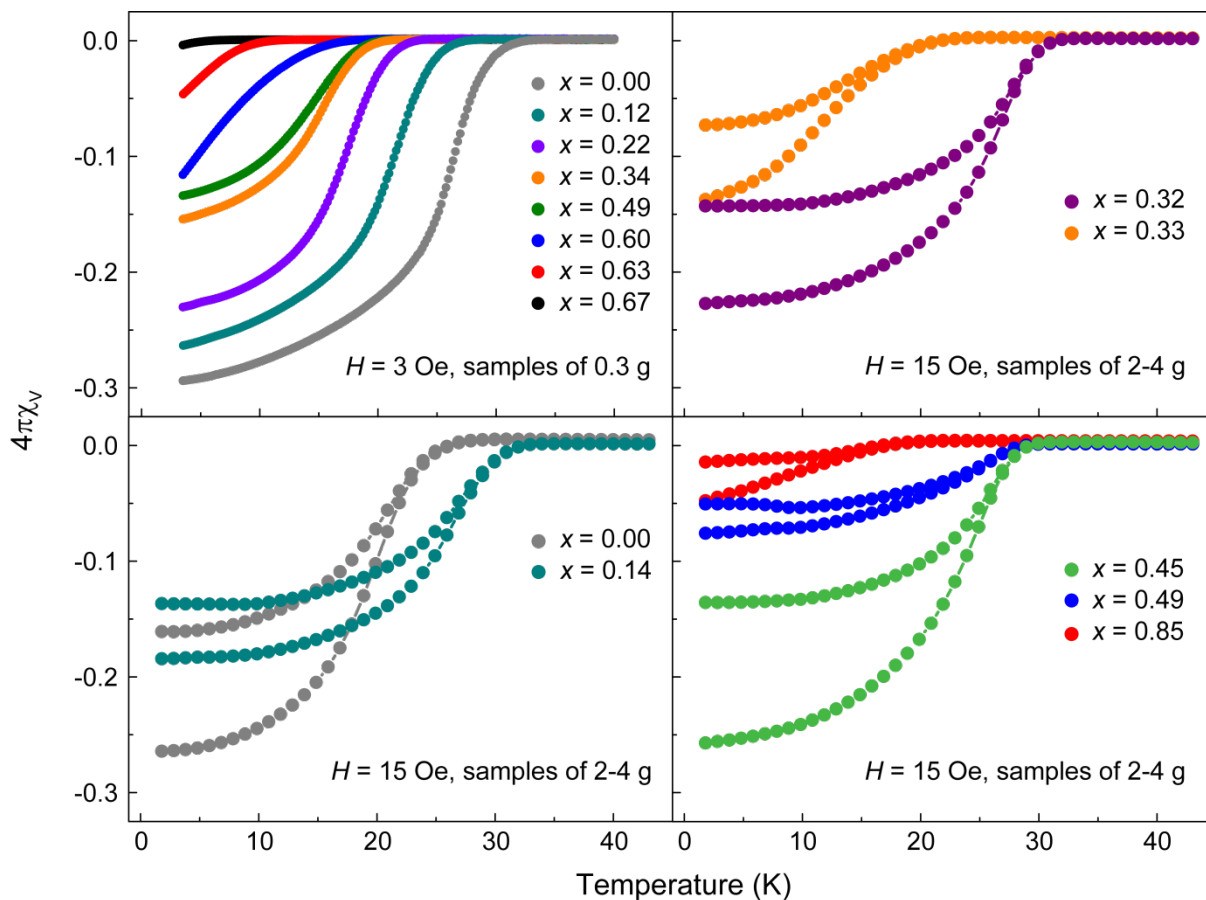


Figure 9.3: AC susceptibility of 0.3-g samples (top left) and zero-field-cooled/field-cooled susceptibility of larger samples (top right and bottom) of $\text{Sr}_2\text{V}_{1-x}\text{Cr}_x\text{O}_3\text{FeAs}$.

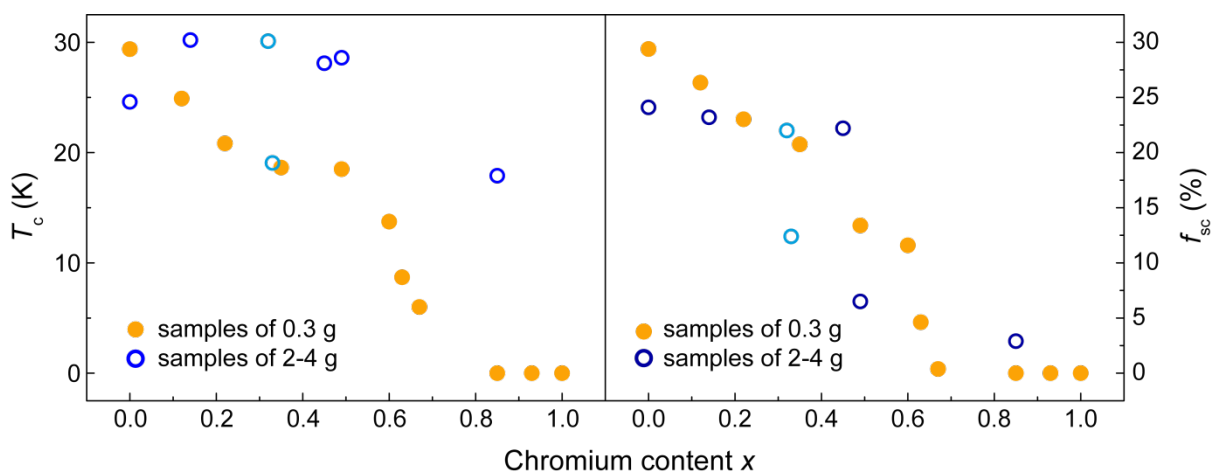


Figure 9.4: Critical temperature (left) and superconducting volume fraction (right) of $\text{Sr}_2\text{V}_{1-x}\text{Cr}_x\text{O}_3\text{FeAs}$ as a function of the chromium content x .

As expected, the substitution of vanadium by chromium leads to a weakening of the superconducting properties. The superconducting volume fraction strongly decreases with

increasing Cr content and we observe the same tendency for T_c . However, samples with a nearly equal chromium content but strongly differing T_c s and f_{sc} s were obtained. The best example for this are the two 2-g samples around $x = 0.3$ (top right in Figure 9.3 and highlighted in light blue in Figure 9.4). One of them has a chromium content of $x = 0.32$ and 22 vol% of the sample become superconducting with a T_c of 30 K. The other one contains only slightly more Cr with $x = 0.33$ but merely 12 vol% of the sample are superconducting with considerably lower $T_c = 19$ K. These strongly differing superconducting properties are very similar to what was reported for the pure vanadium compound $\text{Sr}_2\text{VO}_3\text{FeAs}$, where the controlling factor is still unclear. In case of the solid solution $\text{Sr}_2\text{V}_{1-x}\text{Cr}_x\text{O}_3\text{FeAs}$, possible reasons for different superconducting properties in samples with very similar Cr contents are differences in: 1. the structure (lattice parameters, As-Fe-As tetrahedral angle, Fe-As distance); 2. the amount of possible oxygen deficiency; 3. the mixed occupancy of the Fe site; 4. the strength of the Cr magnetism; 5. the mixing of the vanadium valence.

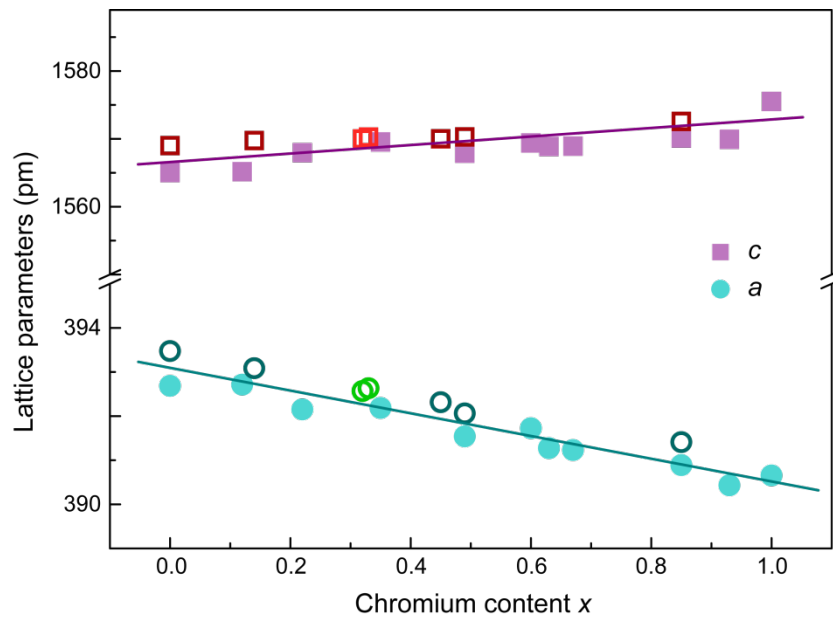


Figure 9.5: Lattice parameters of $\text{Sr}_2\text{V}_{1-x}\text{Cr}_x\text{O}_3\text{FeAs}$ as a function of the chromium content x . Filled symbols: 0.3-g samples; open symbols: 2- to 4-g samples (lighter color: example compounds).

By analyzing the X-ray and neutron powder-diffraction data, structural details were examined in order to test the first possible explanation. As can be seen in Figure 9.5, with increasing Cr content the lattice parameter a decreases and c increases (both by $\sim 0.7\%$). However, regarding the two example compounds (depicted in a lighter color), there is no significant difference in their lattice parameters. The tetrahedral angle and Fe-As distance within the FeAs layers (not shown) do not exhibit any relevant changes within the solid solution. As the effective ionic radius of Cr^{3+} (61.5 pm) is $\sim 4\%$ smaller than the one of V^{3+} (64.0 pm)^[93], the

total height of the interlayer is decreased with increasing Cr content, while the height of the FeAs layer is slightly increased. Nevertheless, no structural differences are detected for the two example compounds. Thus, this cannot be the reason for the observed strongly differing superconducting properties at similar x .

From the neutron data of the 2- to 4-g samples the stoichiometry of the compounds could also be verified. No oxygen deficiency was detected over the whole range of the solid solution (both oxygen sites remained fully occupied during the refinement), therefore possibility no. 2 can be excluded. Furthermore, no chromium or vanadium was found on the iron site, *i.e.* up to $x = 0.85$ there is still no mixing of Cr and Fe in the iron-arsenide layers, which rules out the third possible explanation.

By evaluating the low-temperature neutron data, the magnetism of the Cr^{3+} moments was studied. As we know from earlier experiments with polarized neutrons^[114] the moments order C-type-like at $T_N = 36$ K and the strongest magnetic reflections appear close to the nuclear 0 0 3 reflection. Figure 9.6 shows the 0 0 3 reflection at 297 and 4 K. At $x = 0.49$ and 0.85 we clearly see the additional magnetic $\frac{1}{2} \frac{1}{2} 0$ and $\frac{1}{2} \frac{1}{2} 2$ reflections that unambiguously indicate the ordering of the chromium moments. The sample with $x = 0.45$ already shows a weak onset of this magnetic order. However, none of the two example compounds shows any sign of magnetically ordered chromium. Hence, also the fourth possible explanation for their different superconducting properties is disproved.

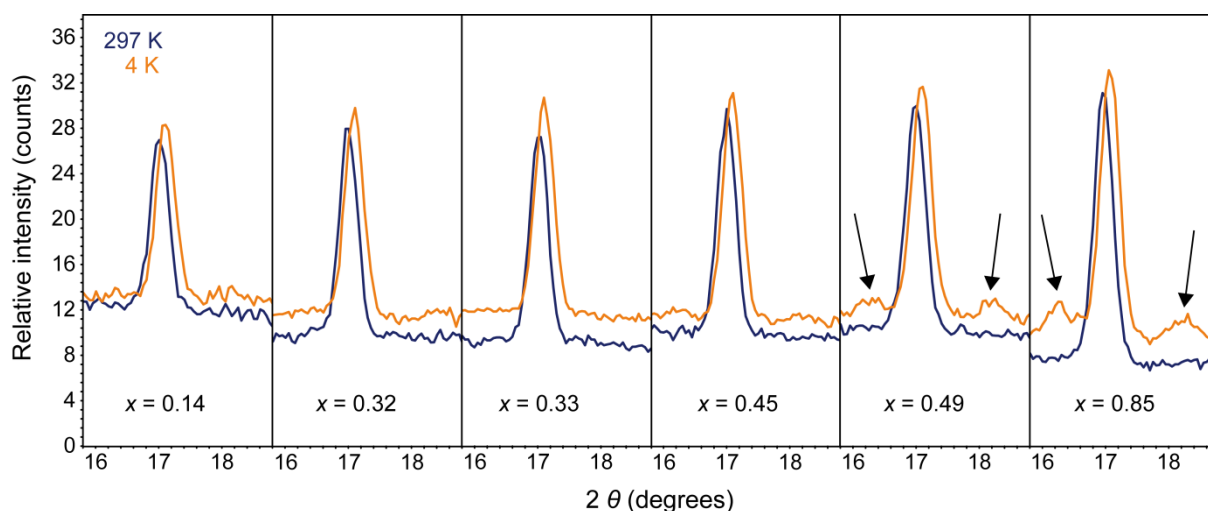


Figure 9.6: SPODI neutron data of $\text{Sr}_2\text{V}_{1-x}\text{Cr}_x\text{O}_3\text{FeAs}$ at 297 K (blue) and 4 K (orange) - nuclear 0 0 3 reflection and developing magnetic reflections.

Consequently, only explanation no. 5 remains to be analyzed: a difference in the valence state of vanadium as the crucial factor for superconductivity. In fact, XPS measurements reveal significantly differing V oxidation states in the two example compounds.

For comparison, XPS measurements were performed on two more samples with equal chromium content $x = 0$ and differing T_c s of 30 K and 25 K, respectively. The structural parameters of both samples differ only slightly and can therefore not explain the differing superconducting properties. As these two compounds are free of chromium, no Cr magnetism or mixed Cr/Fe occupancy can influence the T_c . Only the hypothetical oxygen deficiency cannot be ruled out experimentally for the sample with $T_c = 30$ K as it was not studied via neutron diffraction. However, in earlier studies a sample with similar T_c was analyzed where fully occupied oxygen sites were verified^[95] so there is no reason to expect oxygen deficiency in the sample presented here. Therefore, analogously to the two example compounds discussed before, differing vanadium valence states are a reasonable explanation for the differing superconducting properties and are indeed detected by XPS measurements.

The obtained XPS spectra of all four samples including the theoretical fits are shown in Figure 9.7. While we know from earlier XAS measurements that the pure vanadium compound $\text{Sr}_2\text{VO}_3\text{FeAs}$ contains V^{3+} with a minor contribution of V^{4+} ^[103], fitting the XPS data of $\text{Sr}_2\text{V}_{1-x}\text{Cr}_x\text{O}_3\text{FeAs}$ reveals V^{4+} and V^{5+} , which is probably due to surface oxidation effects. In order to make sure that these results are not influenced by surface oxidation due to measurement artifacts, one sample was measured twice. Once after sample preparation in the glove box (~ 2 seconds of air contact before the measurement) and once after sample preparation at air (~ 1 minute of air contact). The other three samples were measured after preparation in the glove box. The results of all five measurements are listed in Table 9.2.

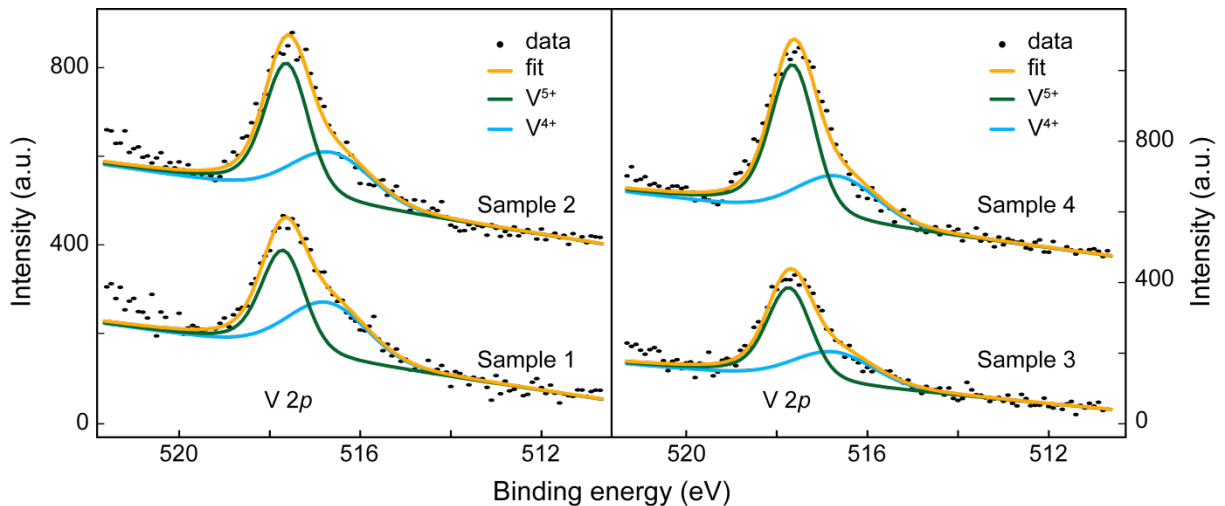


Figure 9.7: XPS spectra of $\text{Sr}_2\text{V}_{1-x}\text{Cr}_x\text{O}_3\text{FeAs}$ with $x \approx 0.3$ (left) and $x = 0$ (right) after preparation in the glove box.

For the sample with $x = 0.32$, $T_c = 30$ K, and $f_{sc} = 22$ vol% we find an oxidation state ratio ($\text{V}^{4+}:\text{V}^{5+}$) of 1.006 after sample preparation in the glove box and 0.940 after 1 minute of air contact. Thus, we get a difference of 6.6 % due to this drastically different handling. The second sample with $x = 0.33$, $T_c = 19$ K, and $f_{sc} = 12$ vol% exhibits a $\text{V}^{4+}:\text{V}^{5+}$ ratio of 0.712. Therefore, the V oxidation state ratios of both samples (prepared in the glove box) differ by 41.3 %. This difference is significantly bigger than the one obtained by different handling of a sample.

The samples with $x = 0$ and $T_c = 30$ K and 25 K exhibit an oxidation state ratio of 0.629 and 0.526, respectively, differing by 19.6 %. Hence, the XPS measurements consistently find larger $\text{V}^{4+}:\text{V}^{5+}$ ratios in the samples with higher critical temperatures. Also, the extent of the differences might be associated to each other. While in the system with $x = 0$ an increase of the oxidation-state ratio by 19.6 % goes along with an increase of the T_c by 19.4 %, the samples with $x \approx 0.3$ exhibit $\text{V}^{4+}:\text{V}^{5+}$ ratios differing by 41.3 % and T_c s differing by 57.9 %.

Table 9.2: XPS data for $\text{Sr}_2\text{V}_{1-x}\text{Cr}_x\text{O}_3\text{FeAs}$.

	x	T_c	preparation	ratio $\text{V}^{4+}:\text{V}^{5+}$
Sample 1	0.32	30 K	at air	0.940
			glove box	1.006
Sample 2	0.33	19 K	glove box	0.712
Sample 3	0.00	30 K	glove box	0.629
Sample 4	0.00	25 K	glove box	0.526

While the measured values of the oxidation states do not reflect the actual situation within the bulk samples due to probable surface oxidation, the drastic difference in the oxidation-state ratio cannot be ascribed to different handling of the samples during the measurement as they were all prepared under argon atmosphere and even one minute of air contact before the measurement led to a deviation of only 6.6 %.

Therefore, these results reveal a sample-intrinsic difference in the surface area, which must originate from significant valence-state differences in the bulk samples. As no differences regarding any of the other four factors discussed above for influencing the superconducting properties were detected either in the two compounds with $x \approx 0.3$ or in both compounds with $x = 0$, this proves the key role of the vanadium oxidation state for superconductivity in $\text{Sr}_2\text{V}_{1-x}\text{Cr}_x\text{O}_3\text{FeAs}$.

9.4 Conclusion

The solid solution $\text{Sr}_2\text{V}_{1-x}\text{Cr}_x\text{O}_3\text{FeAs}$ is superconducting up to $x = 0.63$ and shows traces of superconductivity even up to a chromium content of 85 %. The influences which the substitution of vanadium by chromium has upon the superconducting properties were systematically studied: the structure, the occupancy of the different crystallographic sites, the magnetism of Cr, and the valence state of V within the different samples. Finally, all results indicate the key role of the valence state of vanadium for the superconducting properties of $\text{Sr}_2\text{V}_{1-x}\text{Cr}_x\text{O}_3\text{FeAs}$. As XPS measurements are restricted to the surface area of the measured samples, the actual oxidation state within the bulk samples could not be determined but only relative changes therein. Further XAS experiments on $\text{Sr}_2\text{V}_{1-x}\text{Cr}_x\text{O}_3\text{FeAs}$ could help to reveal actual values and assign them to the corresponding superconducting properties. Nevertheless, identifying the vanadium valence state as important factor for the superconducting properties of $\text{Sr}_2\text{V}_{1-x}\text{Cr}_x\text{O}_3\text{FeAs}$ contributes to the understanding of this system of iron-based superconductors.

10 The influence of oxygen deficiency in the solid solution $\text{Sr}_2\text{V}_{1-x}\text{Cr}_x\text{O}_{3-y}\text{FeAs}$

10.1 Introduction

In superconducting $\text{Sr}_2\text{VO}_3\text{FeAs}$ a possible oxygen deficiency has been a subject of discussions ever since its discovery in 2009^[97]. Originally, it was suspected that oxygen deficiency was the reason and thus a necessary prerequisite for the emergence of superconductivity in this system. By now, it is believed by many researchers in this field that oxygen deficiency is the reason for the strongly differing T_c s found for $\text{Sr}_2\text{VO}_3\text{FeAs}$. Mostly, high T_c s close to the maximum value of 37 K are ascribed to nearly fully occupied oxygen sites and lower T_c s are said to correlate with increasing oxygen deficiency.^[102,119-121] However, in none of these reports the actual oxygen content is ever determined experimentally. Either the nominal oxygen deficiency is treated as the actual value or the true oxygen deficiency is estimated by the compound's weight or lattice parameters. In one case even the mere presence of impurity phases (without further analysis of their composition) was taken as proof for oxygen deficiency in the main phase.^[122]

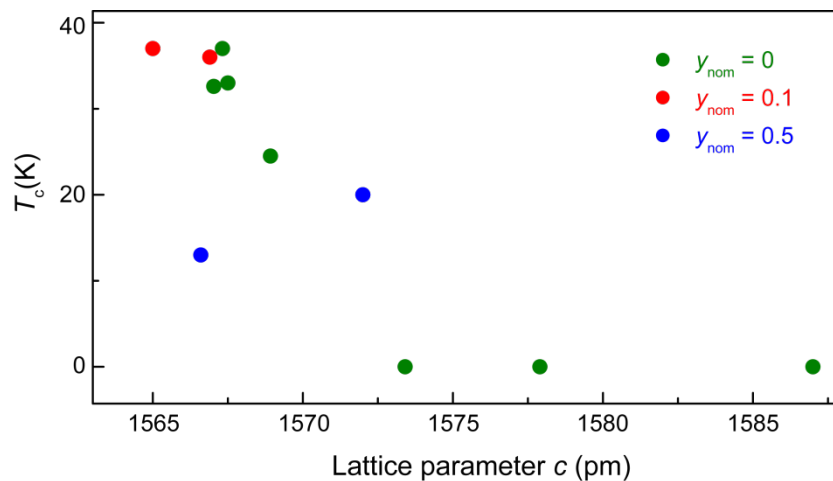


Figure 10.1: Critical temperature of $\text{Sr}_2\text{VO}_3\text{FeAs}$ samples as a function of their lattice parameter c , compiled from [97,100-102,109,120,122].

Figure 10.1 shows the critical temperature of $\text{Sr}_2\text{VO}_3\text{FeAs}$ samples with nominal oxygen deficiencies of $y_{\text{nom}} = 0, 0.1,$ and 0.5 as a function of their lattice parameter c , compiled from different publications^[97,100-102,109,120,122]. Here, no correlation between the nominal oxygen deficiency y_{nom} , the lattice parameter c , and the critical temperature of a compound can be

found, as c and T_c vary for samples with equal values of y_{nom} . Nevertheless, many statements in literature are based upon these unconfirmed correlations.

In the very few reports in which the actual oxygen content has been determined experimentally, samples with the nominal composition of $\text{Sr}_2\text{VO}_3\text{FeAs}$ and a T_c of 33 K and 25 K, respectively, did not exhibit any oxygen deficiency.^[95,96]

Although oxygen deficiency in $\text{Sr}_2\text{VO}_3\text{FeAs}$ is intensely discussed and its significance for the superconducting properties of the compound is broadly accepted, its actual influence is still unclear and has not been systematically analyzed up to now. It is only assumed that differing T_c s are caused by a change of the oxygen content. However, as discussed in Chapter 9, the strongly varying T_c s found for samples of $\text{Sr}_2\text{V}_{1-x}\text{Cr}_x\text{O}_3\text{FeAs}$ with similar chromium contents were not caused by differences regarding the oxygen contents but the vanadium valence states. These samples were synthesized without nominal oxygen deficiency and neutron experiments confirmed the full occupancy of all oxygen sites.

To analyze the influence of nominal oxygen deficiency, the solid solution $\text{Sr}_2\text{V}_{1-x}\text{Cr}_x\text{O}_{3-y}\text{FeAs}$ was synthesized with x and $y = 0 - 0.5$. The effects on the structural and magnetic properties of the compounds are studied and the alleged correlations between oxygen deficiency, structural parameters, and superconducting properties are put to the test.

10.2 Experimental details

Polycrystalline samples of $\text{Sr}_2\text{V}_{1-x}\text{Cr}_x\text{O}_{3-y}\text{FeAs}$ with nominal values for x and $y = 0 - 0.5$ (with a step size of 0.1) were synthesized by heating stoichiometric mixtures of Sr, V, Cr, Fe_2O_3 , Fe, and As_2O_3 in alumina crucibles which were sealed in silica ampoules. The reaction mixtures were then treated according to the synthesis described for 0.3-g samples in Chapter 9.2.

Room-temperature X-ray powder-diffraction patterns were recorded using the Huber diffractometer with $\text{Cu-K}\alpha_1$ radiation. For Rietveld refinements of the diffraction data the TOPAS package^[30] was used with March Dollase functions to describe the preferred orientation of the crystallites. Shape anisotropy effects were described by the approach of *Le Bail* and *Jouanneaux*^[31]. Energy dispersive X-ray (EDX) experiments were performed on the Carl Zeiss EVO-MA 10. For magnetic measurements the AC susceptometer was used.

10.3 Sample composition

Compounds with the nominal composition $\text{Sr}_2\text{V}_{1-x}\text{Cr}_x\text{O}_{3-y}\text{FeAs}$ were obtained as black polycrystalline samples. Figure 10.2 exemplarily shows the X-ray powder-diffraction pattern of a sample with $x = 0.3$ and $y = 0.1$ including its Rietveld refinement.

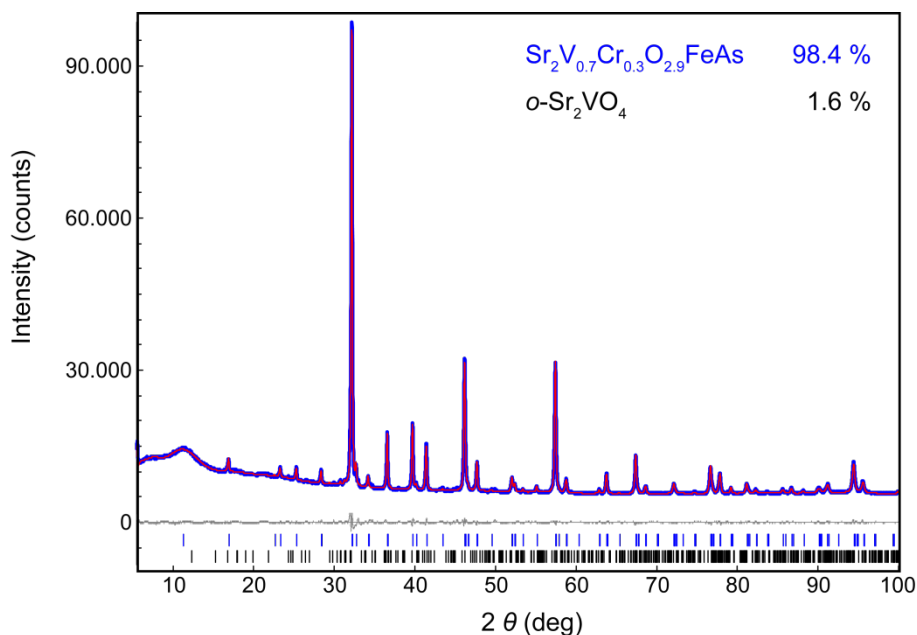


Figure 10.2: X-ray powder-diffraction data of $\text{Sr}_2\text{V}_{0.7}\text{Cr}_{0.3}\text{O}_{2.9}\text{FeAs}$ (blue) and Rietveld refinement (red).

Orthorhombic and tetragonal Sr_2VO_4 , FeAs, Fe_3O_4 , and one unidentified phase were detected as impurity phases (Table 10.1). Surprisingly, samples with higher nominal oxygen deficiencies y_{nom} exhibit less impurity phases, whereby the smallest amount appears around $y_{\text{nom}} = 0.3$. This trend is observed for all examined chromium contents.

The chromium content within the 21311 phase of each sample was determined via EDX measurements. In Figure 10.3, the correlation between nominal chromium content and the one found experimentally is depicted. The experimental values of x tend to be slightly larger than x_{nom} , which can be explained by the fact that no chromium was detected in the impurity phases. Therefore, the ratio of V and Cr within the main phase is shifted towards a higher chromium content by the impurity phases which contain vanadium. Unfortunately, the effective oxygen deficiency could not be determined via EDX measurements with the required accuracy. Thus, all results in this chapter will be referred to the nominal oxygen deficiency.

Table 10.1: Composition of the $\text{Sr}_2\text{V}_{1-x}\text{Cr}_x\text{O}_{3-y}\text{FeAs}$ samples according to Rietveld refinements.

x_{nom}	y_{nom}	$\text{Sr}_2\text{V}_{1-x}\text{Cr}_x\text{O}_{3-y}\text{FeAs}$	amount (wt%) of				unidentified phase
			<i>o</i> - Sr_2VO_4	<i>t</i> - Sr_2VO_4	FeAs	Fe_3O_4	
0.0	0.0	63	6	20	7	4	-
	0.1	70	5	16	6	3	-
	0.2	> 93	2	1	3	-	< 1
	0.3	89	5	3	-	3	-
	0.4	> 92	-	2	-	3	< 3
	0.5	> 86	-	4	-	5	< 5
0.1	0.0	49	16	19	13	3	-
	0.1	79	5	9	6	1	-
	0.2	> 93	2	-	4	-	< 1
	0.3	98	1	-	1	-	-
	0.4	> 93	3	-	2	-	< 2
	0.5	85	-	11	-	4	-
0.2	0.0	64	5	17	11	3	-
	0.1	89	4	3	4	-	-
	0.2	93	4	-	3	-	-
	0.3	> 94	4	-	1	-	< 1
	0.5	> 78	4	6	3	4	< 5
0.3	0.0	63	4	19	11	3	-
	0.1	98	2	-	-	-	-
	0.2	> 94	3	-	2	-	< 1
	0.3	> 94	3	-	-	-	< 3
	0.5	> 80	4	5	3	3	< 5
0.4	0.0	71	8	10	7	4	-
	0.1	> 91	2	2	3	-	< 2
	0.2	> 92	3	-	3	-	< 2
0.5	0.0	70	-	16	9	5	-
	0.1	> 93	-	2	3	-	< 2
	0.2	> 94	-	-	3	-	< 3

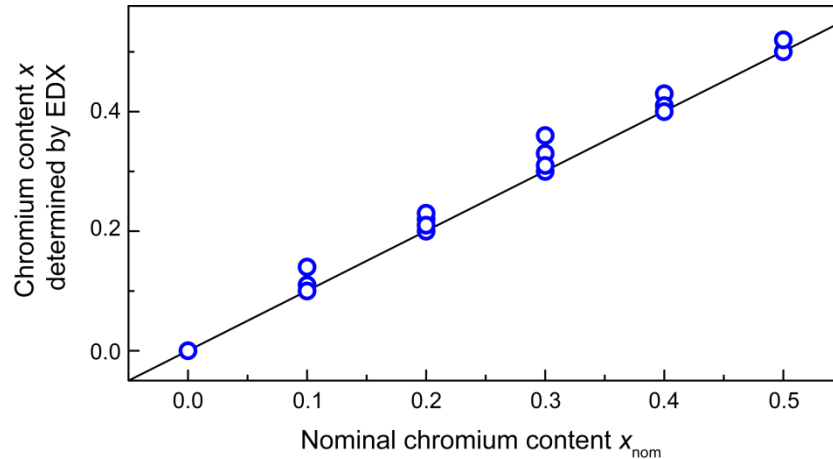


Figure 10.3: Relation between the nominal Cr content in $\text{Sr}_2\text{V}_{1-x}\text{Cr}_x\text{O}_{3-y}\text{FeAs}$ and the one determined by EDX.

10.4 Crystal structure

Figure 10.4 shows the lattice parameters a and c as a function of the nominal oxygen deficiency for the different chromium contents. Here, only nominal chromium contents are given for reasons of clarity. With increasing y_{nom} the lattice parameter c increases by an average of 0.1 % per 10 % oxygen deficiency no matter how much Cr the samples contain. However, a is not influenced significantly by the nominal oxygen deficiency at Cr contents of 0 to 30 % but increases by 0.1 % per 10 % increase of y_{nom} for Cr contents of 40 and 50 %.

As discussed in Chapter 9, without nominal oxygen deficiency the lattice parameter a decreases and c increases with rising Cr content x (both by ~ 0.07 % per 10 % increase of x). Here, this tendency is also observed in samples with nominal oxygen deficiencies of 10 to 30 %. At higher levels of y_{nom} , this relation is reversed.

The geometry of the iron-pnictide or iron-chalcogenide tetrahedral layers has often been found to be crucial for the superconducting properties of a system. For the solid solution $\text{Sr}_2\text{V}_{1-x}\text{Cr}_x\text{O}_3\text{FeAs}$ no such correlation was observed. In order to examine whether this situation changes by introducing a nominal oxygen deficiency, the twofold tetrahedral angle α and the Fe-As distance within the tetrahedra of $\text{Sr}_2\text{V}_{1-x}\text{Cr}_x\text{O}_{3-y}\text{FeAs}$ are both depicted in Figure 10.5 as a function of the nominal oxygen deficiency.

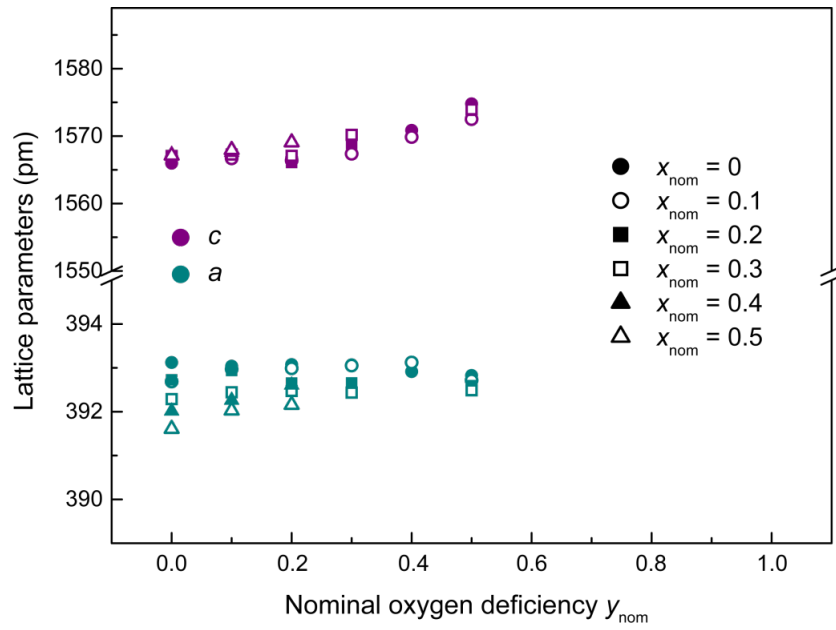


Figure 10.4: Lattice parameters a (green) and c (purple) of $\text{Sr}_2\text{V}_{1-x}\text{Cr}_x\text{O}_{3-y}\text{FeAs}$ as a function of y_{nom} .

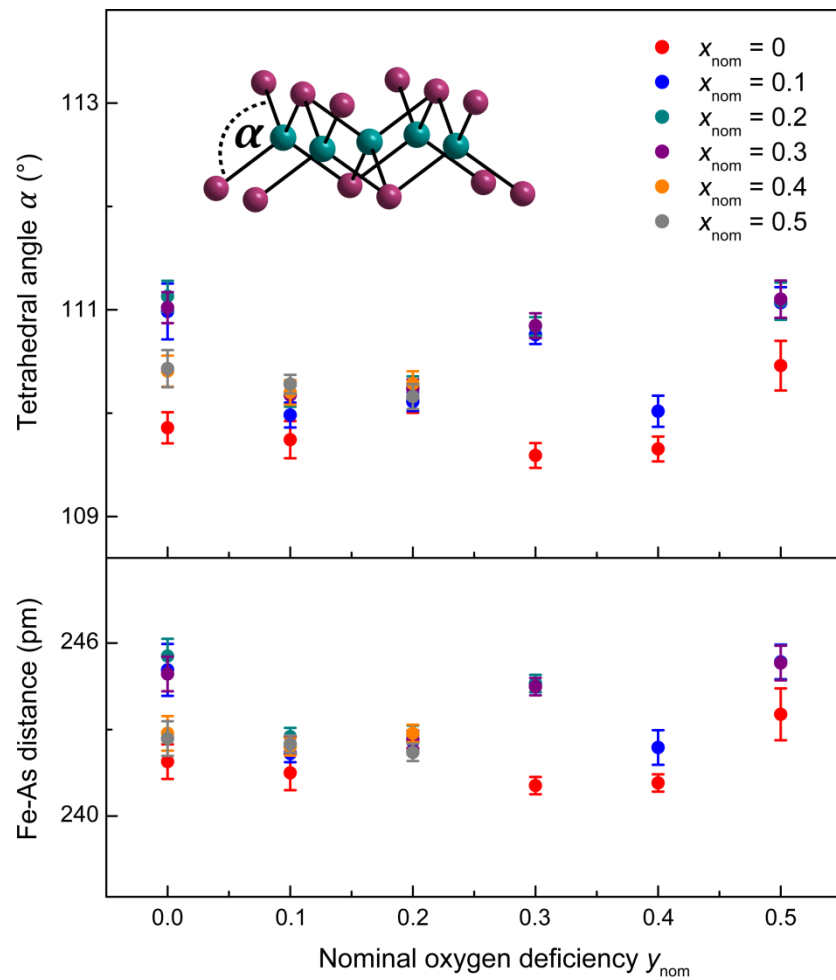


Figure 10.5: Tetrahedral angle α and Fe-As distance in $\text{Sr}_2\text{V}_{1-x}\text{Cr}_x\text{O}_{3-y}\text{FeAs}$ as a function y_{nom} .

The values of the tetrahedral angle are allocated around an average value of 110.4° with a mean deviation of 0.4 %, while the Fe-As distance exhibits an average of 243.2 pm and a mean deviation of 0.6 %. However, both structural parameters do not show a significant correlation with neither the nominal oxygen deficiency nor the chromium content.

10.5 Magnetic properties

AC susceptibility measurements revealed superconductivity with strongly differing critical temperatures and superconducting volume fractions in 18 of the 28 samples (Figure 10.6). Table 10.2 gives an overview of the emergence of superconductivity within the solid solution $\text{Sr}_2\text{V}_{1-x}\text{Cr}_x\text{O}_{3-y}\text{FeAs}$.

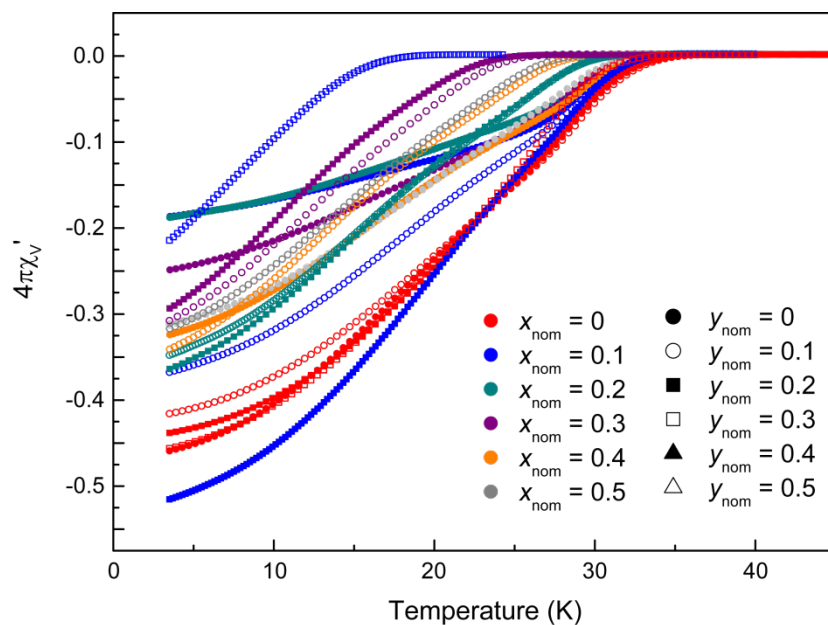
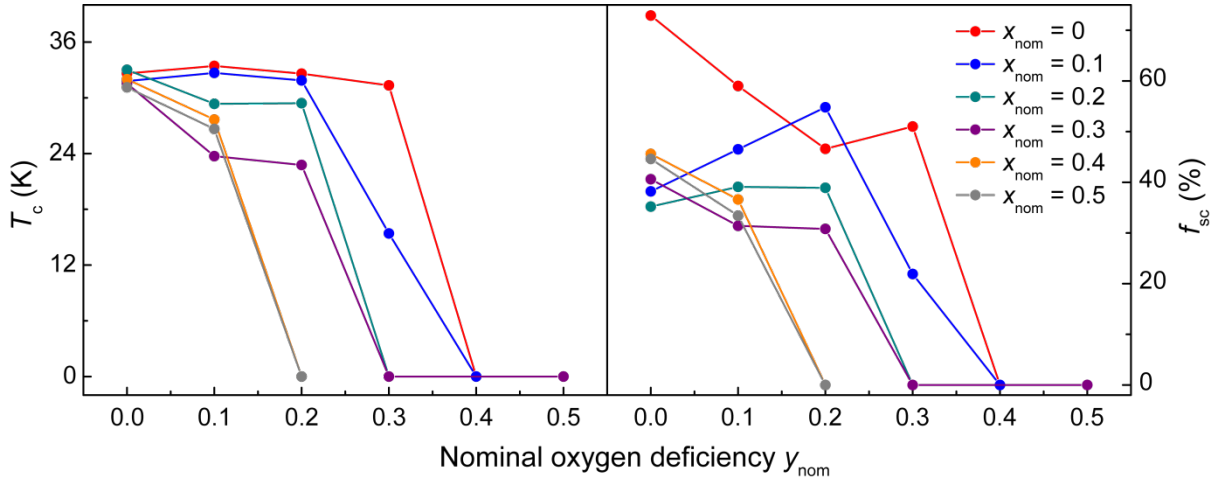


Figure 10.6: AC susceptibility data of the superconducting samples within the solid solution $\text{Sr}_2\text{V}_{1-x}\text{Cr}_x\text{O}_{3-y}\text{FeAs}$.

Clearly, superconductivity in $\text{Sr}_2\text{V}_{1-x}\text{Cr}_x\text{O}_{3-y}\text{FeAs}$ is suppressed by reducing the amount of oxygen provided during the synthesis. The critical amount of nominal oxygen vacancies at which superconductivity still emerges becomes smaller with increasing chromium content. Thus, both the substitution of vanadium by chromium and minimizing the oxygen content weaken the superconducting properties of the system. In order to examine this correlation in more detail, Figure 10.7 shows the behavior of the critical temperature and the superconducting volume fraction as a function of the nominal oxygen deficiency. Here, the superconducting volume fraction f_{sc} has been adjusted to the main phase fraction of the sample. Again, for clarity only the nominal Cr content is given.

Table 10.2: Occurrence of superconductivity in $\text{Sr}_2\text{V}_{1-x}\text{Cr}_x\text{O}_{3-y}\text{FeAs}$. Superconducting samples are marked with "sc", non-superconducting ones with "non-sc".

		x_{nom}					
		0.0	0.1	0.2	0.3	0.4	0.5
y_{nom}	0.0	sc	sc	sc	sc	sc	sc
	0.1	sc	sc	sc	sc	sc	sc
	0.2	sc	sc	sc	sc	non-sc	non-sc
	0.3	sc	sc	non-sc	non-sc	-	-
	0.4	non-sc	non-sc	-	-	-	-
	0.5	non-sc	non-sc	non-sc	non-sc	-	-


 Figure 10.7: Critical temperature T_c (left) and superconducting volume fraction f_{sc} (right) of $\text{Sr}_2\text{V}_{1-x}\text{Cr}_x\text{O}_{3-y}\text{FeAs}$ as a function of the nominal oxygen deficiency y_{nom} .

At a certain amount of nominal oxygen deficiency the superconductivity in $\text{Sr}_2\text{V}_{1-x}\text{Cr}_x\text{O}_{3-y}\text{FeAs}$ is suppressed. The higher the chromium content x , the smaller this critical amount of oxygen deficiency y_{nom} is. Also, the superconducting volume fraction is reduced with increasing x and y_{nom} . The weakening effect, which the substitution of V by Cr in $\text{Sr}_2\text{V}_{1-x}\text{Cr}_x\text{O}_3\text{FeAs}$ has upon the superconducting properties of the system, has already been shown in Chapter 9. Here, it is found that this effect is strengthened by additionally introducing oxygen vacancies. For the pure vanadium compound, superconductivity is preserved with high critical temperatures of 31 to 33 K up to nominal oxygen deficiencies of 30 %. In this series, the superconducting volume fraction diminishes from 73 % without oxygen deficiency to 51 % with $y_{\text{nom}} = 0.3$. However, in samples with a chromium content of 50 % a nominal oxygen deficiency of 0.2 is already sufficient to fully suppress superconductivity.

While a clear tendency towards lower T_c s and f_{sc} s with increasing y_{nom} is observed, a linear correlation cannot be verified. Especially for $\text{Sr}_2\text{VO}_{3-y}\text{FeAs}$, for which such a correlation has often been referred to in literature, T_c stays nearly constant up to $y_{nom} = 0.3$.

Figure 10.8 shows color-coded 3D plots, where the behavior of critical temperature and superconducting volume fraction within the solid solution $\text{Sr}_2\text{V}_{1-x}\text{Cr}_x\text{O}_{3-y}\text{FeAs}$ are depicted as functions of both the nominal oxygen deficiency and the experimentally determined chromium content.

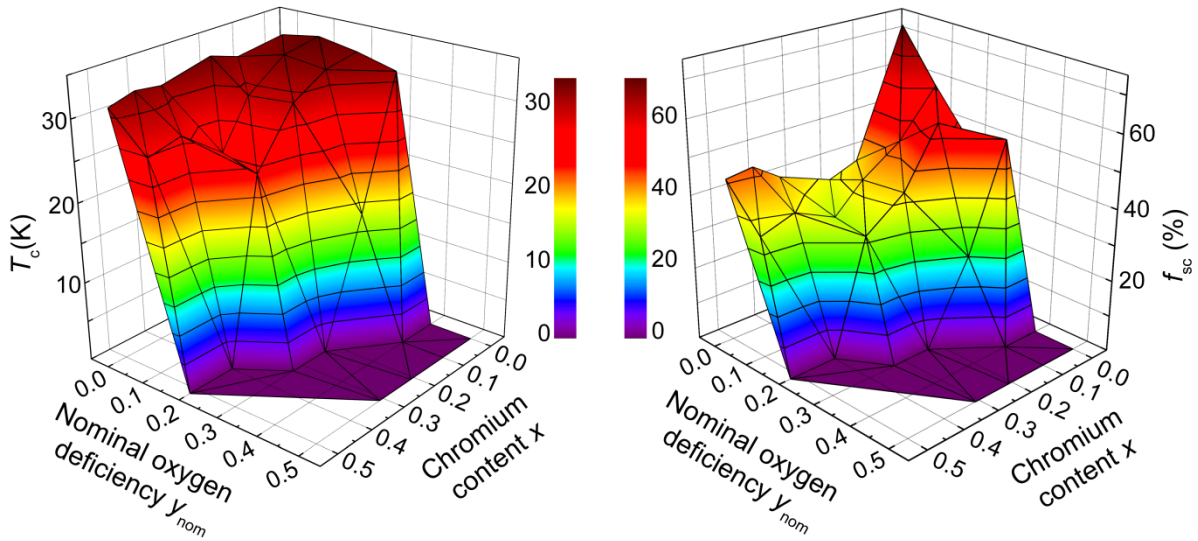


Figure 10.8: Critical temperature T_c (left) and superconducting volume fraction f_{sc} (right) of $\text{Sr}_2\text{V}_{1-x}\text{Cr}_x\text{O}_{3-y}\text{FeAs}$ as functions of nominal oxygen deficiency y_{nom} and chromium content x .

Finally, the alleged correlations between structural parameters, superconducting properties, and the nominal oxygen deficiency in $\text{Sr}_2\text{V}_{1-x}\text{Cr}_x\text{O}_{3-y}\text{FeAs}$ are put to the test. Therefore, the critical temperatures found in this system are displayed as a function of the corresponding lattice parameter c for different values of y_{nom} (Figure 10.9). While there is a general tendency of higher T_c s at smaller values of c and y_{nom} , no strict correlation can be observed. Neither does the critical temperature depend proportionally on the lattice parameter c or y_{nom} , nor is the lattice parameter c directly proportional to y_{nom} . However, we find no superconductivity in samples with c larger than ~ 1568 pm.

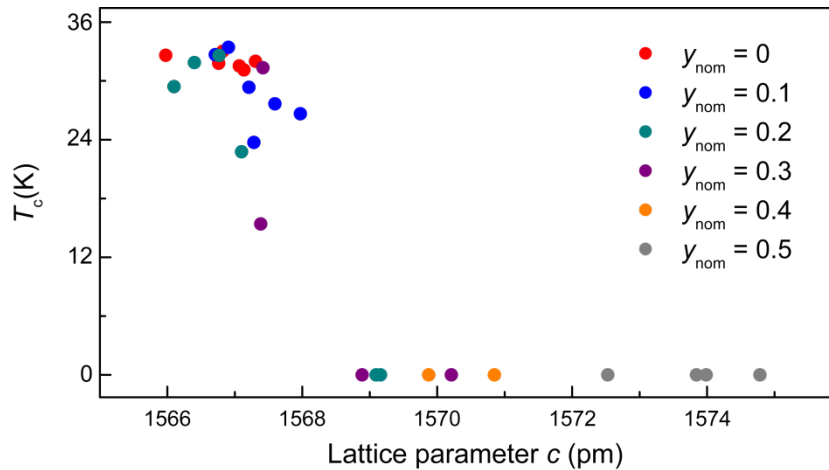


Figure 10.9: Critical temperature of $\text{Sr}_2\text{V}_{1-x}\text{Cr}_x\text{O}_{3-y}\text{FeAs}$ as a function of the lattice parameter c .

10.6 Conclusion

Nominal oxygen deficiency leads to a weakening of the superconducting properties in $\text{Sr}_2\text{V}_{1-x}\text{Cr}_x\text{O}_{3-y}\text{FeAs}$. However, superconductivity is found up to an oxygen deficiency of $y_{\text{nom}} = 0.3$ for a Cr content of 0 and 10 %, up to $y_{\text{nom}} = 0.2$ for 20 and 30 % of Cr, and only up to $y_{\text{nom}} = 0.1$ for 40 and 50 % of Cr. The best superconducting properties within this system are found for the stoichiometric, pure vanadium compound $\text{Sr}_2\text{VO}_3\text{FeAs}$, while substituting vanadium by chromium as well as reducing the amount of oxygen provided during the synthesis weakens superconductivity. Nevertheless, the critical temperature does not decrease directly proportionally to the amount of nominal oxygen deficiency in $\text{Sr}_2\text{VO}_{3-y}\text{FeAs}$ but stays nearly constant until superconductivity is fully suppressed at $y_{\text{nom}} = 0.3$.

Additionally, no strict correlation between structural and superconducting properties is found. The geometry of the iron-arsenide tetrahedra (tetrahedral angle and Fe-As distance) does not show any significant dependence on the nominal oxygen deficiency. While the lattice parameter c increases by an average of 0.1 % per 10 % nominal oxygen deficiency, this is not directly correlated to a change in the critical temperature or superconducting volume fraction. Therefore, this correlation, which is often used in literature for estimating the actual oxygen deficiency within a sample, is disconfirmed.

As already discussed in Chapter 9, controlling the T_c in this system is very complicated as it strongly depends on the valence state of vanadium which leads to an internal electron doping of the iron-arsenide layer. Nevertheless, it would be interesting to compare the nominally introduced oxygen deficiency in $\text{Sr}_2\text{V}_{1-x}\text{Cr}_x\text{O}_{3-y}\text{FeAs}$ with the actual oxygen content in the samples, which could be determined by neutron experiments.

11 Summary

The focus of the present thesis lay on the analysis of magnetic and superconducting properties of layered manganese and iron pnictides. The studies were performed using a broad range of experimental methods like XRD, EDX, susceptibility, resistivity, Mössbauer, heat capacity, XPS, polarized and non-polarized neutron diffraction, and μ SR measurements. If useful, these experiments were complemented by theoretical calculations. The thoughtful combination of adequate methods allowed a detailed analysis of the relevant physical properties of each system.

Dynamic magnetism in CsMn_2P_2

Via neutron measurements the magnetic structure of CsMn_2P_2 has successfully been solved. The compound exhibits a C-type antiferromagnetic order within the magnetic space group $P4_2/m'm'c'$. Hereby, the manganese moments are oriented along [001], order antiferromagnetically along [110], and ferromagnetically along [001]. While this ordering is already detected at room temperature, the magnetic susceptibility indicates a Néel temperature of 11 K and Curie-Weiss behavior above this temperature.

μ SR measurements exhibit clear evidence of dynamic effects in the magnetism of CsMn_2P_2 . A static magnetic ground state is reached through transitions at 64, 17, and 11 K, which are detectable via μ SR, specific heat, resistivity, susceptibility, and XRD measurements.

In spite of the broad spectrum of experimental methods applied, a conclusive explanation for the exceptional magnetic behavior of this compound cannot be given at this point. It appears to be a unique phenomenon which has not been reported in literature so far. Additional experiments like inelastic neutron scattering might help to solve the mystery about the magnetic properties of CsMn_2P_2 . As the observed dynamic effects are probably due to the $\text{Mn}^{2+}/\text{Mn}^{3+}$ mixed valence, it is also interesting to analyze the magnetic properties of the isoelectronic and isostructural RbMn_2P_2 in detail in the future and compare the obtained results.

The electronic structure of CsMn_2P_2

The electronic structure of CsMn_2P_2 was calculated for the experimentally detected C-type structure and compared to two hypothetical models: one non-magnetic and the other one with G-type antiferromagnetic ordering as found in the isostructural BaMn_2P_2 ^[52]. In agreement with the experimental data, the C-type ordering appeared as most favorable one

of the three models. The calculated effective moment per manganese atom is very close to the one determined experimentally.

Additionally, possible indications for the origin of the observed dynamic effects were investigated based on spin-polarized relativistic Korringa-Kohn-Rostoker (SPR-KKR) calculations. The obtained exchange coupling parameters between neighboring manganese atoms predict that the coupling within the layers is considerably stronger than between them. While the moments within one layer are expected to align to each other already at high temperatures, the ordering between the layers probably occurs well below room temperature.

Modifying the magnetism in CsMn_2P_2

$\text{Cs}_{1-x}\text{Rb}_x\text{Mn}_2\text{P}_2$ samples with $x = 0.18$ and 0.76 were obtained in good quality. While the structural changes, which are found in CsMn_2P_2 at low temperatures, are already suppressed at $x = 0.18$, the resistivity measurement shows anomalies which indicate that the dynamic effects are probably not yet fully suppressed. This should be examined for the whole range of the solid solution.

The synthesis of $\text{Cs}_{1-x}\text{Ba}_x\text{Mn}_2\text{P}_2$ turned out to be more complicated than $\text{Cs}_{1-x}\text{Rb}_x\text{Mn}_2\text{P}_2$ and a further optimization of the process is required in order to conclusively examine the physical properties of this solid solution.

Annealing CsMn_2P_2 under oxygen and hydrogen atmospheres did successfully modify its magnetic properties, reduce the effective manganese moment, and slightly change the structural parameters.

Further neutron and μSR experiments are required in order to examine how or if the modifications have influenced the complicated dynamic effects of the magnetism in CsMn_2P_2 . Additionally, a substitution of the manganese in CsMn_2P_2 is a promising way to modify its magnetic properties, whereby elements which do typically not exhibit magnetic ordering are especially interesting.

$\text{Eu}_3\text{Sc}_2\text{O}_5\text{Fe}_2\text{As}_2$

With $\text{Eu}_3\text{Sc}_2\text{O}_5\text{Fe}_2\text{As}_2$, a new member of the iron-based 32522 family is introduced. It does not undergo a structural transition between 300 and 10 K. Magnetic measurements revealed an effective moment of $7.79 \mu_{\text{B}}$ per europium atom, in good agreement with the theoretical value of $7.94 \mu_{\text{B}}$ for Eu^{2+} ^[79].

Antiferromagnetic ordering at 5 K is indicated by a drop in the magnetic susceptibility. ^{151}Eu and ^{57}Fe Mössbauer measurements confirm the susceptibility results, showing a resonance for Eu^{2+} and the beginning of a cooperative magnetic phenomenon below 5 K.

Although the compound itself does not exhibit superconductivity, it is a possible parent compound for future superconductors. Different substitution sites and methods were tested but no signs of superconductivity were detected.

The effects of chemical pressure in the solid solution $\text{Sr}_2\text{ScO}_3\text{FeAs}_{1-x}\text{P}_x$

$\text{Sr}_2\text{ScO}_3\text{FeAs}$ contains $\text{FeAs}_{4/4}$ tetrahedra with nearly ideal tetrahedral symmetry (fourfold angle of 108.9°) but does not show any signs of superconductivity. However, the tetrahedra in $\text{Sr}_2\text{ScO}_3\text{FeP}$ are compressed (fourfold angle of 105.3°) but the compound is superconducting with $T_c \approx 16$ K.

The chemical pressure in $\text{Sr}_2\text{ScO}_3\text{FeAs}_{1-x}\text{P}_x$ causes a compression of the $\text{FePn}_{4/4}$ tetrahedral layer, while the perovskite-like interlayer is slightly decompressed. Thereby, the FePn tetrahedra are flattened. Superconductivity emerges at phosphorus contents of $x \geq 0.61$, while traces of superconductivity are already detected at $x = 0.49$. The maximum T_c of 19.5 K is found for $x = 0.86$.

It is interesting to compare the effects of chemical pressure upon $\text{Sr}_2\text{ScO}_3\text{FeAs}$ studied here with the results of future experiments on $\text{Sr}_2\text{ScO}_3\text{FeAs}$ under physical pressure.

Weak magnetism and the Mott state of vanadium in superconducting $\text{Sr}_2\text{VO}_3\text{FeAs}$

Neutron diffraction experiments unambiguously prove the stoichiometry of $\text{Sr}_2\text{VO}_3\text{FeAs}$, without oxygen deficiency or V doping on the Fe site. Eliminating these factors as possible origin for the superconductivity in this compound leaves intrinsic electron doping due to a $\text{V}^{3+}/\text{V}^{4+}$ mixed valence as probable explanation.

Experiments using polarized neutrons give evidence of a magnetic ordering of the vanadium moments around 45 K with a probable propagation vector $q = \left(\frac{1}{8}, \frac{1}{8}, 0\right)$. The experimentally determined magnetic moment of $\sim 0.1 \mu_B$ per vanadium is more than one order of magnitude smaller than earlier LDA+ U calculations predicted in order to obtain the typical quasinested Fermi surface topology of iron-based superconductors. Theoretical calculations revealed a

Mott state of the vanadium 3d orbitals, which removes these states from the Fermi level even without a significant magnetic moment.

The results consistently show that $\text{Sr}_2\text{VO}_3\text{FeAs}$ is a typical iron-arsenide superconductor without deviations from the nominal composition, thereby giving conclusive answers to long-discussed topics.

Superconductivity in $\text{Sr}_2\text{V}_{1-x}\text{Cr}_x\text{O}_3\text{FeAs}$

The up to now unknown solid solution $\text{Sr}_2\text{V}_{1-x}\text{Cr}_x\text{O}_3\text{FeAs}$ displays superconductivity up to $x = 0.63$ and shows traces of superconductivity even up to a chromium content of 85 %. Strongly differing T_c s are found for similar values of x . The system comprises a large amount of possible control factors, like structural features, the occupancy of the different crystallographic sites, the magnetism of Cr, or the valence state of V.

A systematical analysis of two compounds with similar Cr content ($x = 0.32$ and 0.33) but strongly differing critical temperatures ($T_c = 30$ K and 19 K) and superconducting volume fractions (22 and 12 vol%) indicates the key role of the vanadium valence state for the superconducting properties.

The influence of oxygen deficiency in the solid solution $\text{Sr}_2\text{V}_{1-x}\text{Cr}_x\text{O}_{3-y}\text{FeAs}$

Nominal oxygen deficiency in $\text{Sr}_2\text{V}_{1-x}\text{Cr}_x\text{O}_{3-y}\text{FeAs}$ (with x and $y = 0 - 0.5$) weakens the superconducting properties. The highest T_c and superconducting volume fraction within this system are found for $\text{Sr}_2\text{VO}_3\text{FeAs}$, while substituting vanadium by chromium, as well as reducing the amount of oxygen provided during the synthesis, reduces both parameters. Nevertheless, T_c does not decrease directly proportionally to the amount of nominal oxygen deficiency in $\text{Sr}_2\text{VO}_{3-y}\text{FeAs}$ but stays nearly constant until superconductivity is fully suppressed at $y_{\text{nom}} = 0.3$.

The correlation between structural parameters, O-deficiency, and T_c , which is often used in literature, was proved wrong. Although per 10 % nominal oxygen deficiency the lattice parameter c increases by an average of 0.1 %, this is not directly correlated to a change in the critical temperature or superconducting volume fraction. The significance of these results can be increased further by determination of the actual oxygen deficiencies via neutron experiments as compared to the nominal values.

The present thesis has revealed new features about known compounds and has clarified topics, which had been subject to numerous discussions. Additionally, new compounds have successfully been synthesized, including new superconductors and possible candidates for superconducting parent compounds.

The exceptional magnetic properties of CsMn_2P_2 demonstrate that a system which may appear quite conventional at its first appearance is often more complex. Unraveling the mystery about this unique phenomenon will be a challenge for future work.

In the field of iron-based superconductors several factors have been identified or ruled out as significant for the superconducting properties of the studied systems. Hereby, the foundation has been laid for the next step: after detecting the most important influencing factors and understanding their interplay with superconductivity it remains to be learned how to use this knowledge to actively control the properties of a system.

Bibliography

- [1] H. K. Onnes, *Commun. Phys. Lab. Univ. Leiden* **1911**, 12, 120.
- [2] B. T. Matthias, *Physical Review* **1955**, 97, 74-76.
- [3] B. T. Matthias, in *Progress in Low Temperature Physics, Vol. 2* (Ed.: C. J. Gorter), Elsevier, **1957**, pp. 138-150.
- [4] I. I. Mazin, *Nature* **2010**, 464, 183-186.
- [5] Y. Kamihara, T. Watanabe, M. Hirano, H. Hosono, *Journal of the American Chemical Society* **2008**, 130, 3296-3297.
- [6] Z.-A. Ren, W. Lu, J. Yang, W. Yi, X.-L. Shen, C. Zheng, G.-C. Che, X.-L. Dong, L.-L. Sun, F. Zhou, Z.-X. Zhao, *Chinese Physics Letters* **2008**, 25, 2215.
- [7] G. R. Stewart, *Reviews of Modern Physics* **2011**, 83, 1589-1652.
- [8] D. Johrendt, *Journal of Materials Chemistry* **2011**, 21, 13726-13736.
- [9] K. Kuroki, S. Onari, R. Arita, H. Usui, Y. Tanaka, H. Kontani, H. Aoki, *Physical Review Letters* **2008**, 101, 087004.
- [10] I. I. Mazin, D. J. Singh, M. D. Johannes, M. H. Du, *Physical Review Letters* **2008**, 101, 057003.
- [11] I. I. Mazin, M. D. Johannes, *Nat Phys* **2009**, 5, 141-145.
- [12] P. Dai, J. Hu, E. Dagotto, *Nat Phys* **2012**, 8, 709-718.
- [13] D. J. Scalapino, *Reviews of Modern Physics* **2012**, 84, 1383-1417.
- [14] C. de la Cruz, Q. Huang, J. W. Lynn, J. Li, W. R. Li, J. L. Zarestky, H. A. Mook, G. F. Chen, J. L. Luo, N. L. Wang, P. Dai, *Nature* **2008**, 453, 899-902.
- [15] H.-H. Wen, G. Mu, L. Fang, H. Yang, X. Zhu, *EPL (Europhysics Letters)* **2008**, 82, 17009.
- [16] H. Takahashi, H. Okada, Y. Kamihara, S. Matsuishi, M. Hirano, H. Hosono, K. Matsubayashi, Y. Uwatoko, *Journal of Physics: Conference Series* **2010**, 215, 012037.
- [17] E. Wiesenmayer, H. Luetkens, G. Pascua, R. Khasanov, A. Amato, H. Potts, B. Banusch, H.-H. Klauss, D. Johrendt, *Physical Review Letters* **2011**, 107, 237001.
- [18] P. Klüfers, A. Mewis, *Z. Naturforsch.* **1978**, 33 b, 151-155.

- [19] M. Rotter, M. Tegel, D. Johrendt, *Physical Review Letters* **2008**, *101*, 107006.
- [20] W. J. Zhu, P. H. Hor, *Journal of Solid State Chemistry* **1997**, *134*, 128-131.
- [21] X. Zhu, F. Han, G. Mu, B. Zeng, P. Cheng, B. Shen, H.-H. Wen, *Physical Review B* **2009**, *79*, 024516.
- [22] P. M. Shirage, K. Kihou, C.-H. Lee, H. Kito, H. Eisaki, A. Iyo, *Journal of the American Chemical Society* **2011**, *133*, 9630-9633.
- [23] W. J. Zhu, P. H. Hor, *Inorganic Chemistry* **1997**, *36*, 3576-3577.
- [24] S. N. Ruddlesden, P. Popper, *Acta Crystallographica* **1958**, *11*, 54-55.
- [25] H. Ogino, Y. Matsumura, Y. Katsura, K. Ushiyama, S. Horii, K. Kishio, J.-i. Shimoyama, *Superconductor Science and Technology* **2009**, *22*, 075008.
- [26] M. Tegel, *HConvert*, Version 0.8, LMU Munich (Germany), **2011**.
- [27] *STOE WinXPOW*, Version 2.21, STOE & Cie GmbH, Darmstadt (Germany), **2007**.
- [28] *JCPDS, PDF 2*, International Center for Diffraction Data, Swathmore (USA), **2001**.
- [29] O. Schärpf, H. Capellmann, *physica status solidi (a)* **1993**, *135*, 359-379.
- [30] A. Coelho, *TOPAS-Academic*, Version 4.1, Coelho Software, Brisbane (Australia), **2007**.
- [31] A. Le Bail, A. Jouanneaux, *Journal of Applied Crystallography* **1997**, *30*, 265-271.
- [32] M. Tegel, Ph.D. thesis, LMU Munich (Germany), **2011**.
- [33] A. Coelho, *TOPAS-Academic*, Version 5, Coelho Software, Brisbane (Australia), **2012**.
- [34] M. Tegel, *SQUID-Processor*, Version 0.2, LMU Munich (Germany), **2010**.
- [35] M. Tegel, *Susceptometer - Process Data*, LMU Munich (Germany), **2010**.
- [36] M. Tegel, *Conductivity - Process Data*, LMU Munich (Germany), **2010**.
- [37] R. A. Brand, *Normos Mössbauer fitting programme*, University of Duisburg (Germany), **2007**.
- [38] A. Suter, B. M. Wojek, *Physics Procedia* **2012**, *30*, 69-73.
- [39] G. B. Pascua, Ph.D. thesis, University of Zurich (Switzerland), **2014**.
- [40] S. J. Blundell, *Contemporary Physics* **1999**, *40*, 175-192.
- [41] S. Doniach, M. Sunjic, *Journal of Physics C: Solid State Physics* **1970**, *3*, 285.

- [42] P. Blaha, K. Schwarz, G. K. H. Madsen, D. Kvasnicka, J. Luitz, *WIEN2K - An Augmented Plane Wave + Local Orbitals Program for Calculating Crystal Properties*, Version 12.1, TU Wien (Austria), **2012**.
- [43] K. Schwarz, P. Blaha, *Computational Materials Science* **2003**, *28*, 259-273.
- [44] D. J. Singh, L. Nordstrom, *Planewaves, Pseudopotentials and the LAPW Method*, Springer, New York, **2006**.
- [45] H. Ebert, D. Ködderitzsch, J. Minár, *Reports on Progress in Physics* **2011**, *74*, 096501.
- [46] H. Ebert *et al.*, *The Munich SPR-KKR package*, Version 6.3, Munich (Germany), <http://ebert.cup.uni-muenchen.de/SPRKKR>.
- [47] S. H. Vosko, L. Wilk, M. Nusair, *Canadian Journal of Physics* **1980**, *58*, 1200-1211.
- [48] S. Polesya, S. Mankovsky, D. Benea, H. Ebert, W. Bensch, *Journal of Physics: Condensed Matter* **2010**, *22*, 156002.
- [49] A. I. Liechtenstein, M. I. Katsnelson, V. A. Gubanov, *Journal of Physics F: Metal Physics* **1984**, *14*, L125.
- [50] A. I. Liechtenstein, M. I. Katsnelson, V. P. Antropov, V. A. Gubanov, *Journal of Magnetism and Magnetic Materials* **1987**, *67*, 65-74.
- [51] H. G. von Schnering, R. Türcck, W. Hönle, K. Peters, E. M. Peters, R. Kremer, J. H. Chang, *Zeitschrift für anorganische und allgemeine Chemie* **2002**, *628*, 2772-2777.
- [52] S. L. Brock, J. E. Greedan, S. M. Kauzlarich, *Journal of Solid State Chemistry* **1994**, *113*, 303-311.
- [53] F. Hummel, masters thesis, LMU Munich (Germany), **2010**.
- [54] L. Häggström, J. Sjöström, T. Ericsson, *Journal of Magnetism and Magnetic Materials* **1986**, *60*, 171-174.
- [55] F. Schucht, A. Dascoulidou, R. Müller, W. Jung, H. U. Schuster, W. Bronger, P. Müller, *Zeitschrift für anorganische und allgemeine Chemie* **1999**, *625*, 31-36.
- [56] R. S. Hayano, Y. J. Uemura, J. Imazato, N. Nishida, T. Yamazaki, R. Kubo, *Physical Review B* **1979**, *20*, 850-859.
- [57] A. Mewis, *Z. Naturforsch.* **1978**, *33 b*, 606-609.
- [58] X. C. Wang, Q. Q. Liu, Y. X. Lv, W. B. Gao, L. X. Yang, R. C. Yu, F. Y. Li, C. Q. Jin, *Solid State Communications* **2008**, *148*, 538-540.

- [59] M. J. Pitcher, D. R. Parker, P. Adamson, S. J. C. Herkelrath, A. T. Boothroyd, R. M. Ibberson, M. Brunelli, S. J. Clarke, *Chemical Communications* **2008**, 5918-5920.
- [60] F.-C. Hsu, J.-Y. Luo, K.-W. Yeh, T.-K. Chen, T.-W. Huang, P. M. Wu, Y.-C. Lee, Y.-L. Huang, Y.-Y. Chu, D.-C. Yan, M.-K. Wu, *Proceedings of the National Academy of Sciences* **2008**, *105*, 14262-14264.
- [61] C. Löhnert, T. Stürzer, M. Tegel, R. Frankovsky, G. Friederichs, D. Johrendt, *Angewandte Chemie International Edition* **2011**, *50*, 9195-9199.
- [62] N. Katayama, K. Kudo, S. Onari, T. Mizukami, K. Sugawara, Y. Sugiyama, Y. Kitahama, K. Iba, K. Fujimura, N. Nishimoto, M. Nohara, H. Sawa, *Journal of the Physical Society of Japan* **2013**, *82*, 123702.
- [63] Y. Xiao, Y. Su, M. Meven, R. Mittal, C. M. N. Kumar, T. Chatterji, S. Price, J. Persson, N. Kumar, S. K. Dhar, A. Thamizhavel, T. Brueckel, *Physical Review B* **2009**, *80*, 174424.
- [64] W. Uhoja, G. Tsoi, Y. K. Vohra, M. A. McGuire, A. S. Sefat, B. C. Sales, D. Mandrus, S. T. Weir, *Journal of Physics: Condensed Matter* **2010**, *22*, 292202.
- [65] H. S. Jeevan, Z. Hossain, D. Kasinathan, H. Rosner, C. Geibel, P. Gegenwart, *Physical Review B* **2008**, *78*, 092406.
- [66] Y. Qi, Z. Gao, L. Wang, D. Wang, X. Zhang, Y. Ma, *New Journal of Physics* **2008**, *10*, 123003.
- [67] Z. Ren, Q. Tao, S. Jiang, C. Feng, C. Wang, J. Dai, G. Cao, Z. a. Xu, *Physical Review Letters* **2009**, *102*, 137002.
- [68] S. Jiang, H. Xing, G. Xuan, Z. Ren, C. Wang, Z.-a. Xu, G. Cao, *Physical Review B* **2009**, *80*, 184514.
- [69] Anupam, V. K. Anand, P.L. Paulose, S. Ramakrishnan, C. Geibel, Z. Hossain, *Physical Review B* **2012**, *85*, 144513.
- [70] W.-H. Jiao, Q. Tao, J.-K. Bao, Y.-L. Sun, C.-M. Feng, Z.-A. Xu, I. Nowik, I. Felner, G.-H. Cao, *EPL (Europhysics Letters)* **2011**, *95*, 67007.
- [71] U. B. Paramanik, P. L. Paulose, S. Ramakrishnan, A. K. Nigam, C. Geibel, Z. Hossain, *Superconductor Science and Technology* **2014**, *27*, 075012.
- [72] N. Kurita, M. Kimata, K. Kodama, A. Harada, M. Tomita, H. S. Suzuki, T. Matsumoto, K. Murata, S. Uji, T. Terashima, *Physical Review B* **2011**, *83*, 214513.

- [73] Y. He, T. Wu, G. Wu, Q. J. Zheng, Y. Z. Liu, H. Chen, J. J. Ying, R. H. Liu, X. F. Wang, Y. L. Xie, Y. J. Yan, J. K. Dong, S. Y. Li, X. H. Chen, *Journal of Physics: Condensed Matter* **2010**, *22*, 235701.
- [74] N. Kawaguchi, H. Ogino, Y. Shimizu, K. Kishio, J.-i. Shimoyama, *Applied Physics Express* **2010**, *3*, 063102.
- [75] G. F. Chen, T.-L. Xia, H. X. Yang, J. Q. Li, P. Zheng, J. L. Luo, N. L. Wang, *Superconductor Science and Technology* **2009**, *22*, 072001.
- [76] J. Brous, I. Fankuchen, E. Banks, *Acta Crystallographica* **1953**, *6*, 67-70.
- [77] R. Marchand, W. Jeitschko, *Journal of Solid State Chemistry* **1978**, *24*, 351-357.
- [78] M. Tegel, M. Rotter, V. Weiß, F. M. Schappacher, R. Pöttgen, D. Johrendt, *Journal of Physics: Condensed Matter* **2008**, *20*, 452201.
- [79] H. Lueken, *Magnetochemie*, B. G. Teubner Stuttgart, Leipzig, **1999**.
- [80] O. Berkooz, *Journal of Physics and Chemistry of Solids* **1969**, *30*, 1763-1767.
- [81] Y. Zong, K. Fujita, H. Akamatsu, S. Murai, K. Tanaka, *Journal of Solid State Chemistry* **2010**, *183*, 168-172.
- [82] K. Fujita, K. Tanaka, K. Hirao, N. Soga, *Journal of the American Ceramic Society* **1998**, *81*, 1845-1851.
- [83] H. Raffius, E. Mörsen, B. D. Mosel, W. Müller-Warmuth, W. Jeitschko, L. Terbüchte, T. Vomhof, *Journal of Physics and Chemistry of Solids* **1993**, *54*, 135-144.
- [84] A. Błachowski, K. Ruebenbauer, J. Żukrowski, K. Rogacki, Z. Bukowski, J. Karpinski, *Physical Review B* **2011**, *83*, 134410.
- [85] A. K. Jasek, K. Komędera, A. Błachowski, K. Ruebenbauer, J. Żukrowski, Z. Bukowski, J. Karpinski, *Philosophical Magazine* **2015**, *95*, 493-502.
- [86] C.-H. Lee, A. Iyo, H. Eisaki, H. Kito, M. Teresa Fernandez-Diaz, T. Ito, K. Kihou, H. Matsuhata, M. Braden, K. Yamada, *Journal of the Physical Society of Japan* **2008**, *77*, 083704.
- [87] K. Kuroki, H. Usui, S. Onari, R. Arita, H. Aoki, *Physical Review B* **2009**, *79*, 224511.
- [88] S. A. J. Kimber, A. Kreyssig, Y.-Z. Zhang, H. O. Jeschke, R. Valenti, F. Yokaichiya, E. Colombier, J. Yan, T. C. Hansen, T. Chatterji, R. J. McQueeney, P. C. Canfield, A. I. Goldman, D. N. Argyriou, *Nat Mater* **2009**, *8*, 471-475.
- [89] S. Jiang, H. Xing, G. Xuan, C. Wang, Z. Ren, C. Feng, J. Dai, Z. a. Xu, G. Cao, *Journal of Physics: Condensed Matter* **2009**, *21*, 382203.

- [90] M. Rotter, C. Hieke, D. Johrendt, *Physical Review B* **2010**, *82*, 014513.
- [91] H. Kotegawa, T. Kawazoe, H. Tou, K. Murata, H. Ogino, K. Kishio, J.-i. Shimoyama, *Journal of the Physical Society of Japan* **2009**, *78*, 123707.
- [92] H. Ogino, Y. Katsura, S. Horii, K. Kishio, J.-i. Shimoyama, *Superconductor Science and Technology* **2009**, *22*, 085001.
- [93] R. Shannon, *Acta Crystallographica Section A* **1976**, *32*, 751-767.
- [94] V. Zinth, Ph.D. thesis, LMU Munich (Germany), **2012**.
- [95] M. Tegel, T. Schmid, T. Stürzer, M. Egawa, Y. Su, A. Senyshyn, D. Johrendt, *Physical Review B* **2010**, *82*, 140507.
- [96] F. Hummel, Y. Su, A. Senyshyn, D. Johrendt, *Physical Review B* **2013**, *88*, 144517.
- [97] X. Zhu, F. Han, G. Mu, P. Cheng, B. Shen, B. Zeng, H.-H. Wen, *Physical Review B* **2009**, *79*, 220512.
- [98] Y. Kamihara, H. Hiramatsu, M. Hirano, R. Kawamura, H. Yanagi, T. Kamiya, H. Hosono, *Journal of the American Chemical Society* **2006**, *128*, 10012-10013.
- [99] K. Sasmal, B. Lv, B. Lorenz, A. M. Guloy, F. Chen, Y.-Y. Xue, C.-W. Chu, *Physical Review Letters* **2008**, *101*, 107007.
- [100] A. Pal, A. Vajpayee, R. S. Meena, H. Kishan, V. P. S. Awana, *J Supercond Nov Magn* **2009**, *22*, 619-621.
- [101] A. S. Sefat, D. J. Singh, V. Ovidiu Garlea, Y. L. Zuev, M. A. McGuire, B. C. Sales, *Physica C: Superconductivity* **2011**, *471*, 143-149.
- [102] F. Han, X. Zhu, G. Mu, P. Cheng, B. Shen, B. Zeng, H. Wan, *Sci. China Phys. Mech. Astron.* **2010**, *53*, 1202-1206.
- [103] G.-H. Cao, Z. Ma, C. Wang, Y. Sun, J. Bao, S. Jiang, Y. Luo, C. Feng, Y. Zhou, Z. Xie, F. Hu, S. Wei, I. Nowik, I. Felner, L. Zhang, Z. a. Xu, F.-C. Zhang, *Physical Review B* **2010**, *82*, 104518.
- [104] I. R. Shein, A. L. Ivanovskii, *J Supercond Nov Magn* **2009**, *22*, 613-617.
- [105] K. W. Lee, W. E. Pickett, *EPL (Europhysics Letters)* **2010**, *89*, 57008.
- [106] I. I. Mazin, *Physical Review B* **2010**, *81*, 020507.
- [107] T. Qian, N. Xu, Y. B. Shi, K. Nakayama, P. Richard, T. Kawahara, T. Sato, T. Takahashi, M. Neupane, Y. M. Xu, X. P. Wang, G. Xu, X. Dai, Z. Fang, P. Cheng, H. H. Wen, H. Ding, *Physical Review B* **2011**, *83*, 140513.

-
- [108] J. Munevar, D. R. Sánchez, M. Alzamora, E. Baggio-Saitovitch, J. P. Carlo, T. Goko, A. A. Aczel, T. J. Williams, G. M. Luke, H.-H. Wen, X. Zhu, F. Han, Y. J. Uemura, *Physical Review B* **2011**, *84*, 024527.
- [109] S. Tatematsu, E. Satomi, Y. Kobayashi, M. Sato, *Journal of the Physical Society of Japan* **2010**, *79*, 123712.
- [110] H. Nakamura, M. Machida, *Physical Review B* **2010**, *82*, 094503.
- [111] P. Novák, J. Kuneš, L. Chaput, W. E. Pickett, *physica status solidi (b)* **2006**, *243*, 563-572.
- [112] M. Aichhorn, TU Graz (Austria), private communication, **2013**.
- [113] M. Rotter, M. Pangerl, M. Tegel, D. Johrendt, *Angewandte Chemie International Edition* **2008**, *47*, 7949-7952.
- [114] M. Tegel, F. Hummel, Y. Su, T. Chatterji, M. Brunelli, D. Johrendt, *EPL (Europhysics Letters)* **2010**, *89*, 37006.
- [115] E. Hryha, E. Rutqvist, L. Nyborg, *Surface and Interface Analysis* **2012**, *44*, 1022-1025.
- [116] G. Silversmit, D. Depla, H. Poelman, G. B. Marin, R. De Gryse, *Journal of Electron Spectroscopy and Related Phenomena* **2004**, *135*, 167-175.
- [117] J. Mendialdua, R. Casanova, Y. Barbaux, *Journal of Electron Spectroscopy and Related Phenomena* **1995**, *71*, 249-261.
- [118] M. Demeter, M. Neumann, W. Reichelt, *Surface Science* **2000**, *454–456*, 41-44.
- [119] G. Garbarino, R. Weht, A. Sow, C. Lacroix, A. Sulpice, M. Mezouar, X. Zhu, F. Han, H. H. Wen, M. Núñez-Regueiro, *EPL (Europhysics Letters)* **2011**, *96*, 57002.
- [120] R. C. Che, F. Han, C. Y. Liang, X. B. Zhao, H. H. Wen, *Physical Review B* **2014**, *90*, 104503.
- [121] K. Ueshima, F. Han, X. Zhu, H.-H. Wen, S. Kawasaki, G.-q. Zheng, *Physical Review B* **2014**, *89*, 184506.
- [122] Y. Tojo, M. Matoba, Y. Kamihara, *Journal of Applied Physics* **2013**, *113*, 17E157.

Scientific contributions

Publications

Synthesis, Crystal Structure, and Magnetism of $\text{Eu}_3\text{Sc}_2\text{O}_5\text{Fe}_2\text{As}_2$

F. Hummel, M. Tegel, B. Gerke, R. Pöttgen, D. Johrendt
Z. Naturforsch., *accepted*; *arXiv: 1506.02925* **2015**. (Chapter 6)

CuPN_2 : Synthesis, Crystal Structure, and Electronic Properties

F. J. Pucher, F. Hummel, W. Schnick
Eur. J. Inorg. Chem. **2015**, 1886.

$\text{Sn}_6[\text{P}_{12}\text{N}_{24}]$ - A Sodalite-Type Nitridophosphate

F. J. Pucher, Constantin Frhr. von Schrinding, F. Hummel, V. R. Celinski, J. Schmedt auf der
Günne, B. Gerke, R. Pöttgen, W. Schnick
Eur. J. Inorg. Chem. **2015**, 382.

Weak magnetism and the Mott state of vanadium in superconducting $\text{Sr}_2\text{VO}_3\text{FeAs}$

F. Hummel, Y. Su, A. Senyshyn, D. Johrendt
Physical Review B **2013**, *88*, 144517. (Chapter 8)

$\text{Ba}_3\text{Ga}_3\text{N}_5$ - A Novel Host Lattice for Eu^{2+} -Doped Luminescent Materials with Unexpected Nitridogallate Substructure

F. Hintze, F. Hummel, P. J. Schmidt, D. Wiechert, W. Schnick
Chem. Mater. **2012**, *24*, 402.

Non-stoichiometry and the magnetic structure of $\text{Sr}_2\text{CrO}_3\text{FeAs}$

M. Tegel, F. Hummel, Y. Su, T. Chatterji, M. Brunelli, D. Johrendt
EPL (Europhysics Letters) **2010**, *89*, 37006.

Low-temperature Crystal Structure and Fe-57 Mössbauer Spectroscopy of $\text{Sr}_3\text{Sc}_2\text{O}_5\text{Fe}_2\text{As}_2$

M. Tegel, I. Schellenberg, F. Hummel, R. Pöttgen, D. Johrendt
Z. Naturforsch. **2009**, *64 b*, 815.

The Layered Iron Arsenide Oxides $\text{Sr}_2\text{CrO}_3\text{FeAs}$ and $\text{Ba}_2\text{ScO}_3\text{FeAs}$

M. Tegel, F. Hummel, S. Lackner, I. Schellenberg, R. Pöttgen, D. Johrendt.

Zeitschrift für anorganische und allgemeine Chemie **2009**, 635, 2242.

Short range magnetic order in overdoped $\text{Ba}_{1-x}\text{K}_x\text{Fe}_2\text{As}_2$ ($0 \leq x \leq 0.66$)

E. Wiesenmayer, G. Pascua, F. Hummel, H. Luetkens, Z. Guguchia, A. Binek, U. Pachmayr, T. Hermann, T. Goltz, Z. Shermadini, R. Khasanov, A. Amato, H. Maeter, H.-H. Klauss, D. Johrendt.

in preparation.

Superconductivity in $\text{Sr}_2\text{V}_{1-x}\text{Cr}_x\text{O}_3\text{FeAs}$

F. Hummel, K. Hedegger, A.-K. Henß, A. Senyshyn, D. Johrendt

in preparation. (Chapter 9)

Conference contributions

Überraschende magnetische Eigenschaften von CsMn_2P_2

F. Hummel

Hemdsärmelkolloquium, Munich (Germany), February **2015**. (talk)

Weak Magnetism and the Mott State of Vanadium in Superconducting $\text{Sr}_2\text{VO}_3\text{FeAs}$

F. Hummel, Y. Su, A. Senyshyn, D. Johrendt

International Workshop on Novel Superconductors and Super Materials (NS²), Tokyo (Japan), November **2013**. (poster)

The solid solution $\text{Sr}_2\text{V}_{1-x}\text{Cr}_x\text{O}_3\text{FeAs}$

F. Hummel, K. Hedegger, A. Senyshyn, D. Johrendt

SummerSchool on Iron Pnictides (DFG priority program SPP1458), Achatswies (Germany), July/August **2012**. (poster)

Magnetically ordered vanadium in $\text{Sr}_2\text{VO}_3\text{FeAs}$

F. Hummel, Y. Su, A. Senyshyn, D. Johrendt

International Workshop "Iron-Based Superconductors" (DFG priority program SPP1458), Munich (Germany), March **2012**. (poster)

Struktur und Eigenschaften von CsMn₂P₂

F. Hummel

Hirschegg-Seminar für Festkörperchemie, Hirschegg (Austria), June **2011**. (talk)

Neutron diffraction studies on Sr₂MO₃FeAs

F. Hummel, M. Tegel, Y. Su, D. Johrendt

Kick-Off Meeting - DFG priority program SPP1458, Dresden (Germany), February **2011**.
(talk)

Curriculum vitae

Personal details

Name: Franziska Hummel
Date of Birth: 08.08.1984
Place of Birth: Madrid, Spain
Nationality: German

Education

University

Since January 2011 Ph.D. thesis in Inorganic Solid-State Chemistry
in the group of Prof. Dr. D. Johrendt, LMU Munich
Title: "Magnetism and superconductivity in layered manganese
and iron pnictides".

December 2011 Römer award (Dr. Klaus Römer-Stiftung) for master thesis

2008-2010 Master studies in Chemistry, LMU Munich

2005-2008 Bachelor studies in Chemistry and Biochemistry, LMU Munich

2003-2005 Bachelor studies in Communication, LMU Munich

School

June 2003 Abitur

1997-2003 Luisengymnasium Munich

1994-1997 Ludwigsgymnasium Munich

1991-1994 Canisius Schule Munich

1990-1991 Deutsche Schule Madrid